

Dislocation Cross-Slip in Face-Centered Cubic Solid Solution Alloys

THÈSE N° 8383 (2018)

PRÉSENTÉE LE 12 FÉVRIER 2018

**À LA FACULTÉ DES SCIENCES ET TECHNIQUES DE L'INGÉNIEUR
LABORATOIRE DE MODÉLISATION MÉCANIQUE MULTI-ÉCHELLE
PROGRAMME DOCTORAL EN MÉCANIQUE**

ÉCOLE POLYTECHNIQUE FÉDÉRALE DE LAUSANNE

POUR L'OBTENTION DU GRADE DE DOCTEUR ÈS SCIENCES

PAR

Wolfram Georg NÖHRING

acceptée sur proposition du jury:

Prof. J. Botsis, président du jury

Prof. W. Curtin, directeur de thèse

Prof. D. Rodney, rapporteur

Prof. K. Albe, rapporteur

Dr P. Derlet, rapporteur



ÉCOLE POLYTECHNIQUE
FÉDÉRALE DE LAUSANNE

Suisse
2018

Whence, in order to discover ores, I think it better to abandon the way of bestial and fearless men and to choose the way of using the signs that are exhibited to us through the benignity of Nature, founded on truth and approved by all experts because of their experience, which, as is evident, does not consist of words or promises of incomprehensible and vain things.

— Vannoccio Biringuccio, *De la pirotechnia* (1540)

Acknowledgements

This work was carried out from 2014 to the time of writing at the École polytechnique fédérale de Lausanne (EPFL), in the Laboratory for Multiscale Mechanics Modeling (LAMMM). Support was provided by the European Research Council through the Advanced Grant “Predictive Computational Metallurgy”, ERC Grant agreement No. 339081 – PreCoMet, and by EPFL through the use of the facilities of its Scientific IT and Application Support Center.

Before introducing the subject matter, I would like to address a few words of thanks. First and foremost, I would like to thank my thesis advisor, Prof. William A. Curtin, for his support. He always encouraged me to focus on the important parts of physical problems and to keep the larger context in mind. His guidance was very helpful for someone who tends to get bogged down in details. Moreover, I am thankful for his kind and patient leadership style, and for the opportunity to visit several interesting conferences and workshops abroad.

I also thank the members of the jury for agreeing to participate in my PhD exam. Furthermore, I would like to thank the current and former members of LAMMM: Fabio Pavia, Kris Baker, Mike Francis, Phil Moseley, Aitor Luque, Céline Varvenne, Wu Zhaoxuan, Varun Rajan, Francesco Maresca, Binglun Yin, Nikolaos Bouklas, Till Junge, Satish Rao, Ben Szajewski, Mostafa Khosrownejad, Ali Tehranchi, Max Hodapp, Predrag Andric, Shankha Nag, Rasool Ahmad, Yi Hu, Eleanor Mak, Vladimir Dorodnitsyn and Florian Maurin; as well as a number of visiting scholars: Ronald Miller, Derek Warner, Ryo Kobayashi, Maryam Ghazisaeidi, Jun Song and Daniel Mulvihill. I enjoyed the friendly atmosphere in the lab and the lively discussions. Moreover, I owe a debt of gratitude to the secretary of LAMMM, Géraldine Palaj, for her assistance with numerous administrative issues.

I fondly recall the time when Céline, Kris, Aitor and others would supply LAMMM with cake almost every week. I am also grateful to Kris for making me aware of the String method, and to Céline and Aitor for their work on the average atom method. Both methods became indispensable for my work on cross-slip. Furthermore, I am indebted to Aitor for his kind support. I also want to thank Wu Zhaoxuan for many interesting discussions about, and assistance with, atomistic modeling, simulation of dislocations, and technical problems. I thank Satish, who has studied cross-slip extensively himself, for his advice and interesting discussions. Ben introduced me to hiking in Switzerland, which I enjoy a lot. Mike was the “master of ceremony” of many lively discussions. I thank Mostafa, who had entered the PhD program before me, for helpful advice regarding my next steps. Moreover, I thank Ali for his advice and our tremendous discussions. Never forget: you won't find the global minimum. I thank Max, Predrag and Aitor for our many meetings. I wonder how many lemonade bottles we emptied over the course of three years. I fondly recall several hikes and many inspiring conversations with Varun and Max, who share my sense of humor. In this spirit, I wish Max much success with the further development of dislocation jokes. Finally, I thank Francesco, Till and Nikolaos for their sage advice. A special thanks goes to Till for translating the abstract

Acknowledgements

of this thesis into French.

I also thank my friends from the “Stammtisch”, in particular Simon Schütz, with whom I departed on many recreational expeditions into the alps. Without him as planner and cartographer, I would not have went on some hikes and been lost on others. Moreover, I want to thank my friends from Germany for their support. I cannot name them all here, however, I want to thank Simon for our Skype chats, Felix for many exhilarating messages, and Benni and Kathrin for visiting me thrice. Furthermore, I thank Johannes Joel Möller for proofreading the manuscript and basically for his friendship since we were “little” students. Last but not least, I want to thank my family. Without their support this work would not have been possible.

Lausanne, December 5, 2017

W. G. N.

Abstract

The mechanical strength of metals depends on their resistance against various microscopic deformation processes. In ductile metals, the most important process is shearing of the crystal lattice by dislocations. One of the fundamental aspects of dislocation motion is cross-slip of screw dislocations, the process by which they change their glide plane. In Face-Centered Cubic (FCC) metals, cross-slip is supposed to play a role in dislocation structuring, work hardening, recovery, fatigue, etc. Most prior studies on cross-slip in FCC metals focused on pure metals. There have been few studies of solute effects on cross-slip, which are important for engineering alloys. Here, the effects of substitutional solutes are studied using atomistic simulations and statistical modeling.

In the first part of the thesis, the mechanism and energy of cross-slip of short (40 Burgers vectors long) dislocations in Ni-Al, Al-Mg and Cu-Ni alloys are determined using atomistic calculations. These calculations are carried out with real random alloys and with “average” alloys, where the real atom types are replaced by a single average type. By comparison, it is shown that cross-slip is controlled by fluctuations in the solute concentration, i.e. the activation energy for cross-slip is a distributed variable with a large variance around the mean value. The latter changes only little with concentration. Most importantly, activation energies that are significantly lower than the mean value can be observed in random alloys. A linear correlation between the activation energy and the energy difference between the state of the dislocation before and after cross-slip is observed. An analytical, parameter-free model of this energy difference is developed, which takes random changes in solute-dislocation and solute-solute binding energies into account. Thus, it is possible to predict the distribution of activation energies for nucleation of cross-slip.

In the second part, cross-slip of long (10^2 – 10^3 Burgers vectors) dislocations is studied using a random walk model. Cross-slip is seen as a discrete process, where one Burgers vector long subsegments of the dislocation cross-slip one after another. Associated with each step is a random energy due to random changes in solute binding energies, as well as a deterministic energy change due to constriction formation and stress effects. The random walk model allows the calculation of the activation energy distribution for arbitrary dislocation lengths and stresses. Cross-slip of long dislocations is unlikely at zero stress, due to increasing frequency of high activation energies with increasing length. However, an external stress eliminates these high barriers. Cross-slip then becomes a weakest-link problem. Like in the case of short dislocations, activation energies that are significantly lower than average-alloy estimates can be observed in real random alloys.

Keywords: screw dislocation, cross-slip, face-centered cubic crystals, solid solution, atomistic simulation, transition path calculation, random walk, modeling

Zusammenfassung

Die Festigkeit der Metalle ist abhängig von ihrem Widerstand gegen verschiedene mikroskopische Verformungsmechanismen. Der wichtigste Mechanismus in duktilen Metallen ist die Abscherung des Kristallgitters durch Versetzungen. Ein wichtiger Aspekt der Versetzungsbewegung ist die Quergleitung von Schraubenversetzungen, also die Änderung ihrer Gleitebene. Im Falle der kubisch-flächenzentrierten (kfz-) Metalle nimmt man an, dass die Quergleitung bei der Bildung von Versetzungsstrukturen, der Kaltverfestigung, der Ermüdung, etc. eine Rolle spielt. Bei früheren Untersuchungen von Quergleitung in kfz-Metallen standen zumeist die reinen Metalle im Mittelpunkt. Es liegen nur wenige Studien zum Einfluss von Fremdatomen auf die Quergleitung vor. Dieser spielt in technischen Legierungen eine wichtige Rolle. In der vorliegenden Arbeit wird der Einfluss von substitutionellen Fremdatomen mittels atomistischer Simulationen und statistischer Modellierung untersucht.

Im ersten Teil der Arbeit werden der Mechanismus und die Energie der Quergleitung kurzer (40 Burgersvektoren langer) Versetzungen in Ni-Al, Al-Mg und Cu-Ni mit atomistischen Simulationen bestimmt. Diese Berechnungen werden mit echten und "gemittelten" Mischkristallen durchgeführt. Bei letzteren werden die verschiedenen echten Atomtypen durch einen einzigen durchschnittlichen Typ ersetzt. Im Vergleich zeigt sich, dass die Quergleitung stark von Schwankungen in der Konzentration der Fremdatome abhängt, das heißt die Aktivierungsenergie der Quergleitung ist eine Zufallsvariable mit erheblicher Streuung um den Mittelwert. Letzterer ändert sich nur geringfügig mit der Konzentration. Am wichtigsten ist jedoch, dass in den echten Mischkristallen Aktivierungsenergien vorkommen, die erheblich unterhalb des Mittelwertes liegen. Es wird festgestellt, dass die Aktivierungsenergie linear mit der Energiedifferenz zwischen Anfangs- und Endzustand der Versetzung korreliert. Ein analytisches, parameterfreies Modell dieser Energiedifferenz wird vorgestellt. Erfasst werden Änderungen der Bindungsenergien zwischen Fremdatomen und Versetzungen, sowie der Bindungsenergie von Fremdatom-Paaren. Somit ist es möglich, die Verteilung der Aktivierungsenergie für die Nukleation der Quergleitung vorherzusagen.

Im zweiten Teil der Arbeit wird die Quergleitung langer (10^2 – 10^3 Burgersvektoren) Versetzungen mit einem Random-Walk-Modell untersucht. Die Quergleitung wird als diskreter Prozess aufgefasst, bei dem einen Burgersvektor lange Subsegmente der Versetzung nacheinander quergleiten. Verbunden mit jedem Schritt ist sowohl eine zufällige Energieänderung, welche zufälligen Änderungen der Bindungsenergien geschuldet ist als auch eine deterministische Energieänderung, aufgrund von Spannungseffekten und der Bildung einer Einschnürung. Das Random-Walk-Modell erlaubt die Berechnung der Verteilung der Aktivierungsenergie für beliebige Versetzungslängen und äußere Spannungen. Im spannungsfreien Zustand ist die Quergleitung langer Versetzungen wegen der zunehmenden Häufigkeit hoher Aktivierungsenergien unwahrscheinlich. Äußere Spannungen eliminieren

Acknowledgements

diese Barrieren jedoch. Die Quergleitung wird dann zu einem Problem des schwächsten Glieds. Wie im Falle der kurzen Versetzungen werden in echten Mischkristallen Aktivierungsenergien beobachtet, die weit unterhalb des mit einem gemittelten Mischkristall bestimmten Wertes liegen.

Stichwörter: Schraubenversetzung, Quergleitung, kubisch-flächenzentrierter Kristall, Mischkristall, atomistische Simulation, Reaktionspfad-Berechnung, Zufallsbewegung, Modellierung

Résumé

La résistance mécanique de métaux dépend de leur résistance à différents processus de déformation microscopiques. Dans le cas des métaux ductiles, le processus le plus important est le cisaillement du réseau cristallin par des dislocations. Le glissement dévié forme un aspect fondamental du mouvement de dislocations. C'est le mécanisme par lequel elles changent de plan de glissement. Le glissement dévié est censé jouer un rôle dans la structuration des réseaux de dislocations, l'écrouissage, le rétablissement, la fatigue, e.t.c., pour les métaux à réseau cubique à faces centrées (CFC). La plupart des études existantes du glissement dévié en métaux CFC se concentre sur les métaux purs. Seulement quelques peu de travaux ont étudié les effets de solutés sur le glissement dévié, effets qui sont importants pour les alliages utilisés en ingénierie. Ici, l'effet des solutés substitutionnels est étudié en utilisant des simulations atomiques et la modélisation statistique.

La première partie de cette thèse détermine, en utilisant des calculs atomiques, le mécanisme et l'énergie du glissement dévié de dislocations courtes (40 vecteurs Burgers de longs) dans des alliages Ni-Al, Al-Mg et Cu-Ni. Ces calculs sont exécutés avec des vrais alliages aléatoires et des alliages "moyens", dans lesquels les vrais types d'atomes ont été remplacés par un seul type moyen. En comparant les résultats, on peut montrer que le glissement dévié est contrôlé par des fluctuations de la concentration de solutés, c'est-à-dire que l'énergie d'activation du glissement dévié est une variable distribuée qui a une forte variance autour de sa valeur moyenne. Cette moyenne ne dépend que faiblement de la concentration. Surtout, on peut observer des énergies d'activation qui sont significativement plus basses que la moyenne dans les alliages aléatoires. On observe une corrélation linéaire entre l'énergie d'activation et la différence d'énergie entre l'état d'une dislocation avant et après un glissement dévié. Un modèle analytique et sans paramètres de cette différence d'énergie est développé. Il tient compte des variations aléatoires des énergies de liaisons dislocation-soluté et soluté-soluté. Ainsi, il est possible de prédire la distribution des énergies d'activation pour la nucléation de glissement dévié.

La deuxième partie étudie le glissement dévié de longues dislocations (de 100 à 1000 vecteurs Burgers de long) en utilisant un modèle de marche aléatoire. Le glissement est interprété comme un processus discret, où des sous-segments de dislocation d'une longueur d'un vecteur Burgers sont déviés l'un après l'autre. Chaque pas est associé à une énergie aléatoire due aux variations aléatoires d'énergie de liaison de solutés, ainsi qu'une variation déterministe d'énergie due à la formation d'une constriction et des effets de contrainte. Le modèle de marche aléatoire permet de calculer la distribution d'énergie d'activation pour de longueurs de dislocations et états de contrainte arbitraires. Le glissement dévié est peu probable à contrainte nulle à cause de la fréquence élevée des énergies d'activations hautes pour les dislocations longues. Par contre, une contrainte appliquée élimine ces hautes barrières. Le glissement dévié devient un problème de maillon faible. Comme dans le cas des

Acknowledgements

dislocations courtes, on peut observer des énergies d'activation significativement plus basses que dans les alliages moyens dans les vrais alliages aléatoires.

Mots clés : dislocation vis, glissement dévié, cristaux à réseau cubique à faces centrées, solution solide, calcul atomique, calcul de chemin de transition, marche aléatoire, modélisation

Contents

Acknowledgements	i
Abstract (English/Français/Deutsch)	iii
List of Figures	xi
List of Tables	xiii
List of Symbols	xv
Introduction	1
1 Theoretical Background	5
1.1 Dislocations in Face-Centered Cubic Crystals	5
1.2 Cross-Slip in Face-Centered Cubic Crystals	7
1.2.1 Friedel-Escaig Mechanism	8
1.2.2 Continuum Models	9
1.2.3 Atomistic Models	10
1.2.4 Other Mechanisms	11
1.2.5 Cross-Slip at Heterogeneities	12
1.2.6 Alloying Effects	12
1.3 Transition State Theory	13
2 Methods	17
2.1 Atomistic Calculations with Classical Potentials	17
2.1.1 Embedded Atom Method	17
2.1.2 Average Atom Approximation	18
2.2 Selected Alloys	19
2.3 Calculating the Transition Path of Cross-Slip	20
2.3.1 Initial and Final States	20
2.3.2 String Method	22
2.3.3 Initial Guess for the Path	24
2.3.4 Application of an Escaig Stress	24
2.4 Solute Binding Energies	25
3 Cross-Slip of Short Dislocations	27
3.1 Calculations	27
3.2 Results	28

Contents

3.2.1	Average Alloys	28
3.2.2	True Random Alloys	29
3.3	Preliminary Discussion	32
3.4	Analytic Model for the Statistical Distribution of ΔE_{act}	35
3.4.1	General model	35
3.4.2	Solute-Dislocation Contribution	35
3.4.3	Solute-Solute Contribution	37
3.4.4	Results and Comparison to Simulations	40
3.5	Discussion	42
4	Cross-Slip of Long Dislocations	45
4.1	Random Energy Change	46
4.2	Random Walk Model	49
4.2.1	Deterministic Energy Change	50
4.2.2	Stress Effects in the Random Walk Model	51
4.3	Validation Against Atomistic Simulations	54
4.3.1	Zero Stress	54
4.3.2	Non-zero Escaig Stresses	56
4.4	Cross-Slip of Long Dislocations	58
4.4.1	Zero Stress	58
4.4.2	Non-zero Stress	58
4.4.3	Weakest-Link Scaling	61
4.4.4	Predictions Based on Zero Stress Data	62
4.5	Discussion	67
5	Summary	71
6	Outlook	73
A	Appendix	77
A.1	Calculation of Basic Properties	77
A.1.1	Average Alloys	77
A.1.2	Random Alloys	80
A.2	Nudged Elastic Band Method	81
A.3	Convergence in String Method Calculations	81
A.4	System Size Dependence of ΔE_{act} in Atomistic Calculations	86
A.5	Partially Cross-Slipped Dislocations	89
A.6	Extended Solute Pair Model	90
A.6.1	Implementation	94
A.7	E_{det} under Stress	98
A.8	Correlation between ΔE_{act} and ΔE_{end}	99
Bibliography		111
Acronyms		113
Curriculum Vitae		115

List of Figures

1	Introduction to dislocations and cross-slip	2
1.1	Dislocations in FCC	6
1.2	Friedel-Escaig cross-slip mechanism	8
1.3	Schöck-Seeger-Wolf and Fleischer cross-slip mechanisms	11
1.4	Model potential energy surface	15
2.1	Setup for transition path calculations	20
2.2	Transition path calculation on a 2D model landscape	23
2.3	Fixed atoms in dislocation core	26
3.1	Typical states during cross-slip in average Ni-15 at.% Al	29
3.2	Cross-slip transition paths in average alloys	29
3.3	Typical cross-slip transition states in random alloys	30
3.4	Transition paths in Ni+15 at.% Al random alloys	31
3.5	Activation energies ΔE_{act} of cross-slip in random and average alloys	31
3.6	Cross-slip activation energy ΔE_{act} vs. end state energy difference ΔE_{end}	34
3.7	Reference frames for measuring relative solute/dislocation positions	36
3.8	Cutting of first-nearest neighbor solute pairs	39
3.9	Observed and predicted standard deviation of ΔE_{end}	41
4.1	Correlation between pair loss/formation	47
4.2	Observed and predicted standard deviation od ΔE_{end} (extended solute pair model)	48
4.3	Dislocation partitioned into $1b$ long segments	49
4.4	Step selection in the random walk	50
4.5	Energy as a function of the length of the cross-slipped segment	52
4.6	Distributions of ΔE_{act} for $40b$ long dislocations (random walk & atomistics)	55
4.7	Frequency of the location of the maximum as a function of step	56
4.8	Correlation of ΔE_{act} and ΔE_{end} in random walk calculations	57
4.9	Distributions of ΔE_{act} for different random alloys and $N_b = 40\dots 1000$	59
4.10	ΔE_{act} in random Cu+33 at.% Ni for $N_b = 40, 200, 1000$	59
4.11	ΔE_{act} for a $500b$ long dislocation in Cu+33 at.% Ni at stresses 0–200 MPa	60
4.12	ΔE_{act} for a $500b$ long dislocation in random alloys at (0, 10, 200) MPa stress	61
4.13	Weakest-link scaling under Schmid stress	63
4.14	Weakest-link scaling under Escaig stress	64
4.15	Weakest-link scaling: predictions based on zero stress data (Cu+33 at.% Ni)	65
4.16	Weakest-link scaling: predictions based on zero stress data (Al+06 at.% Mg)	66
4.17	Weakest-link scaling: predictions based on zero stress data (Ni+15 at.% Al)	66

List of Figures

A.1	Relative difference between average and random alloy properties	79
A.2	Relative change of ΔE_{act} per iteration	83
A.3	Perpendicular force on transition path in String method calculations	84
A.4	Relative energy and perpendicular force on transition path	84
A.5	Difference between String and NEB estimates for ΔE_{act}	85
A.6	Extreme cases of differences between NEB and String paths	85
A.7	Cross-slip transition path vs. radius of the configuration	87
A.8	Cross-slip transition path vs. length of the configuration	87
A.9	Cross-slip transition path vs. radius at 300 MPa Escaig stress	88
A.10	Partially cross-slipped dislocation	89
A.11	Unit cell used in the derivation of the extended solute pair model	91
A.12	Energy during cross-slip at 150 MPa Escaig stress as a function of step	98
A.13	$\Delta E_{\text{act,avg}}$ as a function of Escaig stress	99
A.14	ΔE_{act} of pure Ni as a function of Schmid stress	99
A.15	$\Delta E_{\text{act}}-\Delta E_{\text{end}}$ -correlation in random walk and atomistics (additional data)	100

List of Tables

1.1	Zero-stress cross-slip energy according to Püschl and Schöck	10
1.2	Reduction of cross-slip activation energy at heterogeneities	13
2.1	FIRE parameters	21
4.1	Neighbor distances	47
4.2	Average alloy activation energy and standard deviation of ΔE_{end} per step	54
A.1	Basic properties of Ni-Al average and random alloys	77
A.2	Basic properties of Cu-Ni average and random alloys	78
A.3	Basic properties of Al-Mg average and random alloys	78
A.4	Equilibrium segment length ζ^* of partially cross-slipped dislocations	90

List of Symbols

$ \dots $	Euclidean norm of ...
γ_{SF}	Stable stacking fault energy
$\gamma_{\text{eff},g}$	Effective stacking fault energy on the glide plane
$\gamma_{\text{eff},c}$	Effective stacking fault energy on the cross-slip plane
ΔE_{act}	Activation energy
$\Delta E_{\text{act,avg}}$	Activation energy of cross-slip in an average alloy
ΔE_{end}	Energy difference between a dislocation lying on the cross-slip and glide plane
$\Delta E_{\text{end,s-s}}$	Contribution to ΔE_{end} from differences in solute-solute binding energies
$\Delta E_{\text{end,s-s,XY}}$	Contribution to ΔE_{end} from cutting/forming of $X-Y$ solute pairs
$\Delta E_{\text{end,s-d}}$	Contribution to ΔE_{end} from differences in solute-dislocation binding energies
$\Delta E_{\text{end,s-d},X}$	Contribution to $\Delta E_{\text{end,s-d}}$ from X -solutes
Δt	Timestep
ΔV_i	Relative energy of image i in a transition path calculation
ξ	Dislocation line direction
$\tau_{\text{glide}}^{\text{Esc}}$	Escaig stress on the glide plane
$\tau_{\text{cross}}^{\text{Esc}}$	Escaig stress on the cross-slip plane
$\tau_{\text{glide}}^{\text{Sch}}$	Schmid stress on the glide plane
$\tau_{\text{cross}}^{\text{Sch}}$	Schmid stress on the cross-slip plane
ζ_{csn}	Characteristic length of cross-slip nucleation
a	Lattice parameter
b	Magnitude of the Burgers vector of a $1/2a\langle 110 \rangle$ dislocation
b_p	Magnitude of the Burgers vector of a $1/6a\langle 112 \rangle$ Shockley partial dislocation

List of Tables

d	Equilibrium dislocation dissociation width
d_g	Dissociation width on the glide plane
d_{cs}	Dissociation width on the cross-slip plane
E_c	Energy of a single constriction
E_{det}	Deterministic energy in random walk
$E_{\text{det}}^{\text{Esc}}$	Contribution to E_{det} from Escaig stresses
$E_{\text{det}}^{\text{Sch}}$	Contribution to E_{det} from a Schmid stress on the cross-slip plane
F	N -dimensional vector of atomic forces
\mathbf{F}_i^\perp	Perpendicular force on image i
k_B	Boltzmann constant
N	Number of atoms
N_b	Dislocation length in Burgers vectors
N_c	Constriction length in Burgers vectors
N_d	Width of stacking fault in number of unit cells
N_T	Number of atom types
N_s	Number of images on the transition path
N_ζ	Length of stacking fault in number of unit cells
R	$3N$ -dimensional vector of atomic positions
\hat{s}	Normalized reaction coordinate
U _{s-s,XY}	Vector of solute-solute binding energies
$U_{n,XY}$	Binding energy of an n-th order pair of X and Y atoms

Introduction

Alloys are the most important class of materials for load bearing structural components in machines, vehicles, aircraft, etc. The purpose of alloying is to achieve superior mechanical properties relative to those of the corresponding pure metal. One of the underlying principles is that alloying elements influence the microscopic deformation mechanisms that govern the macroscopic mechanical behavior. A thorough understanding of this influence is indispensable for designing new, improved alloys.

In ductile metals, movement of dislocations is the most important atomic-scale deformation mechanism. Dislocations are line-like lattice defects, whose movement shears off one part of the crystal with respect to the other. Due to distortion of the lattice, dislocations create a stress field, through which they interact with solute atoms. These interactions and their effects on dislocation motion must be understood in order to make alloy strength predictable.

The principle of dislocations is that the crystal is *not* sheared off at once, by a relative displacement of the two parts over the whole dividing surface. Such a displacement would require very high applied stresses [41]. Instead, the shear is localized. Only a small portion of the crystal is sheared off initially. The line separating sheared and not yet sheared parts of the crystal is the dislocation line, see Fig. 1a) and b). The dislocation is therefore a line-like lattice defect. As it moves through the lattice, a greater portion of the crystal is sheared off. Dislocations are characterized by the line direction ξ and the Burgers vector \mathbf{b} , which indicates the relative displacement of the two parts of the crystal. Based on the relative orientation between ξ and \mathbf{b} , two principal types of dislocations can be distinguished, with different constraints concerning their movement, see Fig. 1a). Edge dislocations with $\xi \cdot \mathbf{b} = 0$ can move conservatively, i.e. without addition or subtraction of mass, only on the lattice plane that is spanned by ξ and the \mathbf{b} . Screw dislocations with $\xi \parallel \mathbf{b}$, on the other hand, can move on any lattice plane that contains \mathbf{b} . The process by which dislocations change between planes is referred to as *cross-slip*.

Cross-slip is important in several ways. A new dislocation source can be generated by double cross-slip [84]. On the other hand, cross-slip can reduce the total dislocation length because it enables mutual annihilation of pairs of opposite dislocations on nearby planes [63]. These two processes are illustrated in Fig. 1b). Furthermore, cross-slip enables dislocations to overcome obstacles, such as precipitates [51, 128]. Recently, the importance of cross-slip for dislocation network formation has been demonstrated using computer simulations [54, 159].

This thesis deals with cross-slip in substitutional alloys of Face-Centered Cubic (FCC) metals.

List of Tables

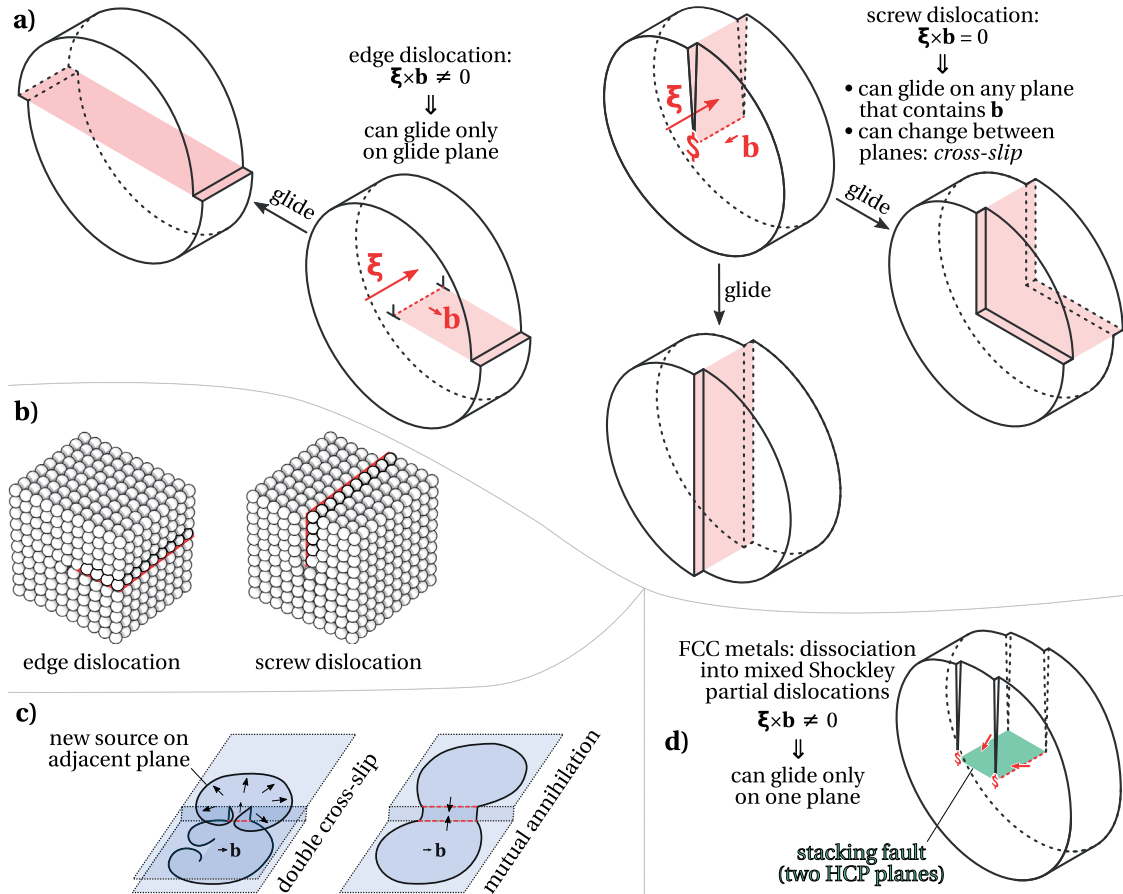


Figure 1: a) Differences between edge and screw dislocations; the line direction ξ and the Burgers vector \mathbf{b} of an edge dislocation are perpendicular and it can move only on the lattice plane spanned by these vectors (red); screw dislocations with $\xi \times \mathbf{b} = 0$ can move on any plane that contains \mathbf{b} ; cross-slip is the process by which they change between planes; b) edge and screw dislocations in a simple cubic lattice; c) cross-slip as a dislocation source or sink mechanism; left: screw part (red) of a Frank-Read source [40] cross-slips twice and generates a source on an adjacent plane; right: screw parts (red) of two dislocation loops on adjacent planes cross-slip towards each other and mutually annihilate; d) in FCC metals, cross-slip is complicated by the splitting of perfect dislocations into Shockley partial dislocations, which have mixed edge/screw character and create a stacking fault

In FCC metals, cross-slip has been invoked to explain observed dislocation network structures, like sheets [55] or persistent slip bands [34], which are formed during cyclical deformation. Mutual annihilation of screw dislocations by cross-slip may explain why the microstructure in the first stage of FCC single crystal deformation consists mainly of edge dislocation dipoles [5, 33, 132]. Furthermore, mutual annihilation by cross-slip has been incorporated into models of work hardening and dynamic recovery [61, 62, 87] and creep at intermediate homologous temperatures [24, 42, 76, 97]. A more controversial issue is whether cross-slip can also explain the transition between the second and third stage of deformation, from linear to parabolic hardening, see e.g. Refs. [3, 32, 66, 125] and Ref. [14, p. 154]. Finally, cross-slip has also been

invoked to explain the copper-brass texture transition [22, 68, 69, 129].

FCC cross-slip is a thermally activated process with an energy barrier. The cause for this energy barrier is the splitting of complete dislocations, whose Burgers vector is a translation vector of the lattice, into pairs of Shockley partial dislocations, see Fig. 1c). The partial dislocations have mixed character and therefore cannot readily cross-slip, but must merge again or undergo some other transformation first. Additionally, a stacking fault, i.e. two atomic planes with Hexagonal Close-Packed (HCP) coordination, is created between the partial dislocations.

Different cross-slip mechanism have been discussed in the literature [39, 43, 125] and the required energy or stress has been calculated using elastic or atomistic models [27, 31, 32, 78, 99, 101, 102, 112, 117, 124, 153, 154], see also Ref. [100] or [14, Ch. 5]. The most frequently discussed mechanism for cross-slip in FCC is the Friedel-Escaig [32, 43] (F-E) mechanism, where cross-slip starts with formation of a point constriction. More recently, cross-slip at heterogeneities, such as jogs or forest dislocations, has been subject of research [103, 104, 106–109, 142]. However, most studies to date have considered cross-slip in pure metals. There are only few dedicated studies of alloying effects on cross-slip. Previous studies considered specific alloys [25] and solute arrangements [151, 152]. In other models, solute effects were reduced to a simple friction term acting on the dislocation [53], or it was assumed that solutes are fully segregated to the dislocation, which is unlikely during deformation at moderate temperatures. In any case, prior studies considered only solute effects on cross-slip nucleation in short ($\sim 10^1$ Burgers vectors) dislocations segments. To the best of our knowledge, cross-slip of long (10^2 – 10^3 Burgers vectors) dislocations has not been studied before.

This thesis is motivated by the lack of comprehensive studies of solute effects on dislocation cross-slip in FCC alloys. The following important questions are addressed in this work.

- What is the effect of substitutional solute atoms on the cross-slip activation energy?
- How does the activation energy change with solute concentration?
- How to model solute effects on cross-slip analytically?
- How to predict the activation energy as a function of matrix and solute properties, and concentration?
- How does cross-slip of long dislocations differ from cross-slip of shorter ones? How does the barrier scale with nucleus size?
- How to predict the activation energy distribution for cross-slip of long dislocations?

To answer these questions, the activation energy of cross-slip was calculated for various solid solutions using atomistic methods. Guided by these calculations, which cover various possible solute effects, we developed statistical models of the distribution of activation energies for cross-slip nucleation in short ($40b$) dislocations, and full cross-slip of long (10^2 – 10^3b) dislocations. We restrict our attention to the important case of random distributions of substitutional solutes, because in many alloys of practical interest, a fraction of the alloying elements remains in solution. A random distribution of solute atoms is a fair assumption when there is no strong preference for short range ordering, and at intermediate temperatures, where segregation is slow. Finally, this work is also relevant for High Entropy Alloys [162], which are highly-concentrated, multi-component random solid solutions.

List of Tables

This thesis is structured as follows. Ch. 1 gives a more detailed introduction into the relevant topics. In addition, the existing literature on cross-slip in FCC is reviewed. The atomistic simulation methods used to study cross-slip are explained in Ch. 2. Ch. 3 deals with nucleation of cross-slip in short ($40b$) dislocation segments. The activation energy for cross-slip in various Ni-Al, Al-Mg and Cu-Ni alloys is determined using atomistic simulations and a model of this distribution is proposed. It is shown that cross-slip is controlled by fluctuations in the solute concentration and that the activation energy in random alloys can be much lower than expected based on models of average alloying effects. Cross-slip of long dislocations is studied in Ch. 4. A random walk model is developed, which allows to predict the cross-slip activation energy distribution for dislocations of arbitrary length. The results are summarized in Ch. 5. Finally, open questions and directions for future research are discussed in Ch. 6.

1 Theoretical Background

Disclaimer

Parts of this chapter are adapted from the following article, with permission from the coauthor and the publisher.

W. G. Nöhring and W. A. Curtin. "Dislocation Cross-Slip in FCC Solid Solution Alloys". In: *Acta Materialia* 128 (Apr. 2017), pp. 135–148. ISSN: 13596454. DOI: 10.1016/j.actamat.2017.02.027

This chapter gives an overview of the theoretical background for the current work. In the first section, important properties of dislocations in FCC crystals are reviewed. For more details about FCC dislocations and dislocation theory in general, the reader is referred to Ref. [1]. Sec. 1.2 deals with cross-slip in FCC. The Friedel-Escaig (F-E) mechanism is explained and other proposed mechanism are reviewed. Furthermore, we review approaches to calculate the required energy or stress, as well as the literature on cross-slip at heterogeneities and alloying effects. Finally, Sec. 1.3 introduces some elements of transition state theory which are relevant for this work.

1.1 Dislocations in Face-Centered Cubic Crystals

Dislocation theory predicts that slip preferentially takes place on close packed planes and along close-packed directions. In the face-centered cubic (FCC) lattice, these are the families of $\{111\}$ planes and $\langle 110 \rangle$ directions, respectively. Indeed, the twelve possible pairings among these families are the most important slip systems in FCC. The corresponding perfect dislocations have Burgers vector $a/2\langle 110 \rangle$.

However, perfect dislocations are typically unstable. It is energetically favorable for them to split up into pairs of Shockley [46] partial dislocations with Burgers vector of type $a/6\langle 112 \rangle$. A simple argument to this effect is Frank's rule [85, see Frank's comment]: Since the energy of a dislocation depends on the square of the magnitude of its Burgers vector, it will tend to split up if this value is greater than the sum of the magnitudes of the resulting partial Burgers vectors. The magnitude b of a $a/2\langle 110 \rangle$ dislocations is $a/\sqrt{2}$, whereas the magnitude b_p of the Burgers

Chapter 1. Theoretical Background

vector of a Shockley partial dislocation is $a/\sqrt{6}$. Since $b^2 > 2b_p^2$, $a/2\langle 110 \rangle$ dislocations are expected to dissociate. Perfect and partial dislocations in FCC are sketched in Fig. 1.1.

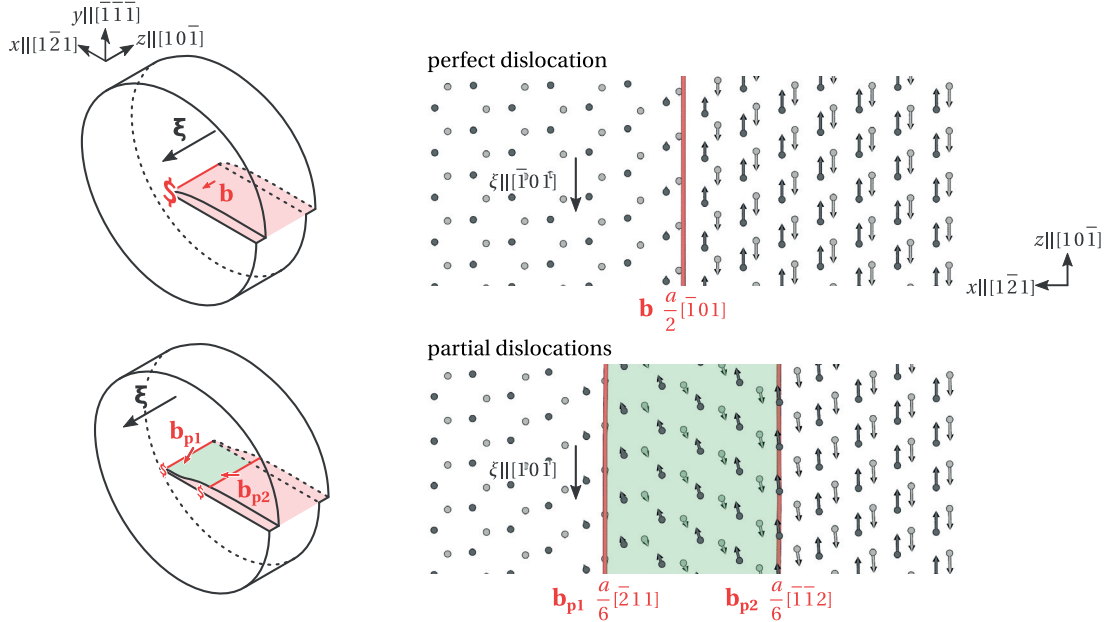


Figure 1.1: Dissociation of perfect dislocations into Shockley partial dislocations in FCC; left: perfect and partial dislocations in a cylindrical body; red: plane across which the displacement is discontinuous (cut plane); green: stacking fault; right: displacements of atoms in the two lattice planes above (dark gray) and below (light gray) the red plane in the left figure; arrows indicate the displacement with respect to the dislocation-free reference configuration; a stacking fault (green) is created between the two partial dislocations

Each $a/2\langle 110 \rangle$ dislocation can split up into two different pairs of $a/6\langle 112 \rangle$ partial dislocations, which correspond to different $\{111\}$ slip planes. For example, $a/2[110]$ can split up into $a/6[121]$ and $a/6[21\bar{1}]$ on the $(\bar{1}\bar{1}\bar{1})$ plane, or into $a/6[211]$ and $a/6[12\bar{1}]$ on the $(1\bar{1}\bar{1})$ plane. The Burgers vector of a Shockley partial dislocation is not a full translation vector of the FCC lattice. As a consequence, the stacking sequence of $\{111\}$ lattice planes, which is A-B-C-A-B-C in FCC, changes to A-B-C-B-C-A in the region between the two partial dislocations. Note that B-C-B-C is the $\{111\}$ stacking sequence of the hexagonal close-packed HCP lattice. Thus, there are two planes of HCP coordinated atoms, an *intrinsic stacking fault*. Associated with this fault is a surface tension (energy per area) γ_{SF} , which is typically on the order of several tens to hundreds of mJ m^{-2} in FCC metals.

γ_{SF} is one of the factors that control the equilibrium separation d between the partial dislocation cores. Two other factors are the interaction between the elastic fields of the dislocations, and, if applicable, their interaction with an external stress field. For analysis of the fields, it is useful to consider the edge and screw components of the partial dislocation separately. Within the framework of isotropic elasticity, such separation is always possible because there is no interaction between pure edge and screw dislocations. Within anisotropic elasticity, separation is possible in special cases, see p. 360 in [1] and references therein. Among them is the present case of interest, where the perfect dislocation is a pure screw

1.2. Cross-Slip in Face-Centered Cubic Crystals

dislocation. The Burgers vectors of the corresponding partial dislocations have the same screw components, but oppositely aligned edge components. The former repel each other, whereas the latter attract each other. An external stress that interacts with the screw components will cause a bow-out. This kind of stress is referred to as Schmid¹ stress. An external stress that interacts with the edge components, on the other hand, will change the splitting width and is referred to as Escaig² stress.

The equilibrium splitting width d can be obtained by requiring that the forces resulting from the stacking fault and the internal and external fields are balanced. Within the framework of isotropic³ elasticity, the solution for an originally pure screw dislocation is [12, 114]

$$d = \frac{1}{\gamma_{SF} + \tau_e b / (2/\sqrt{3})} \frac{\mu b^2}{8\pi} \left(1 - \frac{1}{3(1-\nu)} \right), \quad (1.1)$$

where μ is the shear modulus and ν is Poisson's ratio. Within anisotropic elasticity, the solution is [1, p. 361-362]

$$d = \frac{1}{\gamma_{SF} + \tau_e b / (2/\sqrt{3})} \frac{b^2}{8\pi} \left(K_s - \frac{1}{3} K_e \right), \quad (1.2)$$

where

$$\begin{aligned} K_s &= (C'_{44} C'_{55} - C'_{16})^{1/2}, \\ K_e &= \frac{1}{3} \left(2 + \frac{C'_{22}}{\bar{C}'_{11}} \right) (\bar{C}'_{11} + C'_{12}) \left[\frac{C'_{55} (\bar{C}'_{11} - C'_{12})}{C'_{22} (\bar{C}'_{11} + C'_{12} + 2C'_{55})} \right]^{1/2}, \end{aligned} \quad (1.3)$$

are the energy prefactors of the edge and screw components of an $a/6\langle 112 \rangle$ partial dislocation, respectively, and the primed coefficients are functions of the cubic elastic constants C_{11} , C_{12} , and C_{44} ,

$$\begin{aligned} C'_{11} &= C_{11} & C'_{12} &= C_{12} & C'_{55} &= C_{44} \\ C'_{22} &= C_{11} + \frac{1}{2}H & C'_{23} &= C_{12} - \frac{1}{2}H & C'_{44} &= C_{44} - \frac{1}{2}H \\ \bar{C}'_{11} &= \sqrt{C'_{11} C'_{22}} & H &= 2C_{44} + C_{12} - C_{11}. \end{aligned} \quad (1.4)$$

1.2 Cross-Slip in Face-Centered Cubic Crystals

Dissociation of perfect dislocations into Shockley partial dislocations complicates cross-slip. The two partials lie in only one of the four preferred $\{111\}$ planes and have mixed screw-edge character. Thus, cross-slip requires recombination of the partial dislocations or some other core transformation. Over the years, several cross-slip mechanisms and methods for calculating the required energy have been proposed, see Püschl's review [100] and chapter 5 in Caillard and Martin's book [14]. The present study focuses on a mechanism proposed by

1. Named after Erich Schmid (1896–1983)

2. Named after Bertrand Escaig

Friedel [43]. The associated activation energy was first calculated by Escaig [31, 32], using a line tension model. Therefore, this mechanism is referred to as the Friedel-Escaig (F-E) mechanism. Atomistic calculations of the cross-slip transition path in Cu [112, 143], Ni [143], and Al [57] indicate that the F-E mechanism is the operative mechanism for cross-slip if the dislocation line is sufficiently long.

Cross-slip can nucleate at heterogeneities like jogs or forest dislocations. Such “heterogeneous” cross-slip has received considerable attention in recent years, because the associated activation energy may be significantly lower than that of homogeneously nucleated cross-slip. Here, we are concerned with only one type of heterogeneity, namely solute atoms. Solute effects on cross-slip involving additional heterogeneities will be left for further study.

The rest of this section is structured as follows. The F-E mechanism is explained in the next subsection. In Sec. 1.2.2 and Sec. 1.2.3, continuum and atomistic models for calculation of the cross-slip activation energy are reviewed. Other mechanisms for homogeneous and heterogeneous cross-slip are discussed briefly in Sec. 1.2.4 and Sec. 1.2.5. The section concludes with a review of the literature about alloying effects on FCC cross-slip.

1.2.1 Friedel-Escaig Mechanism

Fig. 1.2 shows the Friedel-Escaig cross-slip mechanism. The perfect screw dislocation is initially dissociated into a pair of Shockley partial dislocations on the $(\bar{1}\bar{1}1)$ glide plane (Fig. 1.2a)). The first step of cross-slip is the formation of a point constriction (Fig. 1.2b)). Starting from there, the dislocation re-dissociates into a pair of Shockley partial dislocations on the $(\bar{1}\bar{1}\bar{1})$ cross-slip plane (Fig. 1.2c)). Since the dislocation line must be closed, the left and right end of the cross-slipped segment are constricted, hence there are now two point constrictions in total. Subsequently, these constrictions move laterally and the cross-slipped segment grows.

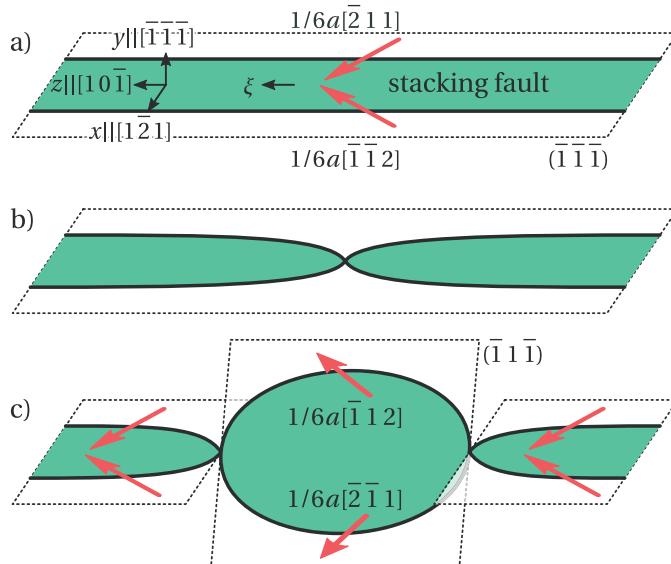


Figure 1.2: Friedel-Escaig cross-slip mechanism

Note that the partial dislocations are close to edge orientation near the left constriction, and close to screw orientation near the right one. Atomistic models show that the screw-like constriction has a negative energy relative to the fully dissociated state, thus it could form spontaneously at a free surface [102, 110].

1.2.2 Continuum Models

Cross-slip costs energy. Initially, energy must be spent to change the splitting width. Some of it is regained later, when the dislocation re-dissociates on the cross-slip plane. Other energy changes are caused by dislocation curvature. First of all, the total line length increases, and therefore the total energy as well. Furthermore, the local character of the dislocation changes, which affects the energy per length, the interaction energy between the partial dislocation, and their self-interaction energy. The sum of these energy changes is positive, thus an energy barrier must be overcome to cross-slip. The required energy must be supplied by an external stress or thermal fluctuations. Stroh [133] calculated the energy of a point constriction using an isotropic elastic line tension model. Similarly, Escaig [31, 32] used a line tension model to calculate the activation energy of cross-slip. The derivation of this model can be found elsewhere [14, 31, 32, 60]. Here, only some important assumptions are summarized.

For the purpose of calculating the interaction energy between infinitesimal segments with the same z -coordinate (see Fig. 1.2), it is assumed that both segments are straight. The interaction energy between segments with different z -coordinate is neglected, as is self-interaction. The only way in which curvature enters the calculation is through a line tension term, which penalizes the increase in length. Furthermore, three ill-defined parameters appear in the calculation: an inner and an outer core cutoff radius, and a minimum splitting width. The latter is the distance below which the two partial dislocations are considered to have combined into a perfect screw dislocation.

These approximations make the F-E model quantitatively inaccurate. However, it provides some qualitative information. At zero applied stress, the barrier energy tends to two times the constriction energy. According to Stroh⁴, the latter scales as

$$E_c \propto d \left(\frac{\mu b^2}{8\pi} \right) \left(1 - \frac{1}{3(1-\nu)} \right) \sqrt{\log \frac{R}{r_0}}, \quad (1.5)$$

where r_0 and R are the inner and outer core cutoff radius, respectively. For a discussion of stress effects, Escaig and Schmid components must be considered separately. An Escaig stress on the glide plane has a stronger effect on the barrier than an Escaig stress on the cross-slip plane. A Schmid stress on the cross-slip plane is even less effective. A Schmid stress on the glide plane can be ignored, since it causes only normal slip. These differences in effectiveness of the stress components have recently been confirmed by direct atomistic calculations of cross-slip under stress [60].

Using Escaig's low stress approximation [32], Bonneville et al. [10] calculated a barrier energy of 1.6 ± 0.2 eV for Cu. Saada [117] obtained (single) constriction energies of 0.7 eV, 0.55 eV and 0.32 eV in Cu for minimum dissociation widths of $2b$, $1b$ and $b/2$. For other metals, a similarly

4. The dependence on Poisson's ratio, which was neglected by Stroh, has been included here.

Chapter 1. Theoretical Background

strong dependence on this parameter was observed. Thus, Saada argues that the F-E model permits only order of magnitude estimates.

Several groups developed more elaborate models, which avoid some of the aforementioned approximations. In the model by Duesbery et al. [27], dislocation self-interactions are calculated explicitly using isotropic elasticity, thus eliminating the line tension approximation. For this purpose, the dislocation lines are discretized into piecewise linear curves. The estimated barrier energy of Cu is⁵ 3.7 eV. Püschl and Schöck [99] also described the dislocations as piecewise linear curves, but calculated segment interactions using anisotropic elasticity. In addition, the authors physically motivated their choice of minimum splitting width. It was chosen such that the energy required to reach this width equals the dissociation energy calculated with a Peierls-Nabarro [86, 95] model of the slip distribution in the dislocation core. According to this model, the constriction energy, which is approximately half the activation energy of cross-slip, follows the trend [100]

$$\frac{E_c}{K_s b^3} \approx 1.2 \times 10^{-2} \frac{d}{b} \log \left(2 \frac{d}{b} \right). \quad (1.6)$$

Using elastic constants from Ref. [1], and the experimentally measured splitting widths listed in Saada's publication [117], see Refs. [16, 17, 56, 82, 123], one obtains the barrier energies listed in Tab. 1.1. Finally, the arguably most elaborate continuum model to date was proposed by Ramírez et al. [101]. Here, the dislocation lines are approximated as cubic splines, thus avoiding discontinuities at the nodes where segments meet. The screw dislocation is actually modeled as a group of fractional dislocations, whose interactions are computed using Cai's [13] isotropic nonsingular solution for the elastic fields. Like in a Peierls-Nabarro model, the fractional dislocations are subject to a lattice restoring force, which in this case is obtained from ab-initio calculations. For Cu, Ramírez et al. obtain a barrier energy of 1.43 eV.

Table 1.1: Energy required for cross-slip at zero stress according to Püschl and Schöck [99]

Element	Ni	Al	Cu	Ag	Au
Energy (eV)	1.0	0.2	1.6	1.8	0.8

1.2.3 Atomistic Models

In the past two decades, atomistic calculations have increasingly been used to study cross-slip. Rasmussen et al. [110, 113] were the first to estimate the energy barrier using an atomistic technique. By separately calculating the formation energy of the two constrictions involved in the process, they arrived at an estimate of 2.7 eV for Cu. Using a similar technique, Rao et al. [102] obtained a value of 4.85 eV and 2.35 eV for two Ni potentials [148]. Note that the first potential underestimates γ_{SF} . This difference shows that an appropriate interatomic potential must be used to obtain an accurate energy estimate. Based on Eq. 1.1 and Eq. 1.5, one would require that the potential gives the correct lattice parameter, elastic constants, and stacking fault energy. Püschl [121] has argued that the whole γ -surface should be correct. Calculations with an anisotropic-elastic Peierls-Nabarro model by Szajewski et al. [137] indicate that the

5. Note that the authors use the Voigt average [147] of μ for calculation, which is an upper bound.

dissociation energy is mainly determined by the difference between γ_{SF} and γ_T , the maximum energy for a stacking fault displacement along the $\langle 110 \rangle$ direction.

Several groups have used atomistic transition path calculations to determine the cross-slip activation energy and pathway. The cross-slip mechanism does not need to be known a priori. Nudged Elastic Band (NEB) [59, 81] calculations with Cu [112, 143], Ni [143], and Al [57] showed that the Friedel-Escaig mechanism is the operative mechanism for cross-slip if the dislocation line is sufficiently long.

1.2.4 Other Mechanisms

Besides the F-E mechanism, two other mechanisms for homogeneous cross-slip have been discussed in the literature. Schöck and Seeger [120, 124] assumed that the dislocation first constricts over a certain length, before it bows out into the cross-slip plane, see Fig. 1.3a). In contrast to the F-E mechanism it does not redissociate immediately⁶. The predicted activation energies for Al and Cu are 1.05 eV and 10 eV, respectively [124]. Wolf [153, 154] calculated the activation energy for the case where cross-slip by this mechanism takes place at the tip of a dislocation pile-up. For a pile-up of 20 dislocations under low external stress ($\tau/\mu \approx 3 \times 10^{-4}$), the activation energy is approximately 0.6 eV in Al and 2.4 eV in Cu⁷. Considering that the Schöck-Seeger-Wolf mechanism has a high activation barrier if there are no pile-ups, and that the F-E mechanism is typically observed in transition path calculations, the latter seems to be the more likely mechanism for homogeneous cross-slip in FCC. However, a combination of the two mechanisms has recently been observed in molecular dynamics simulations [92].

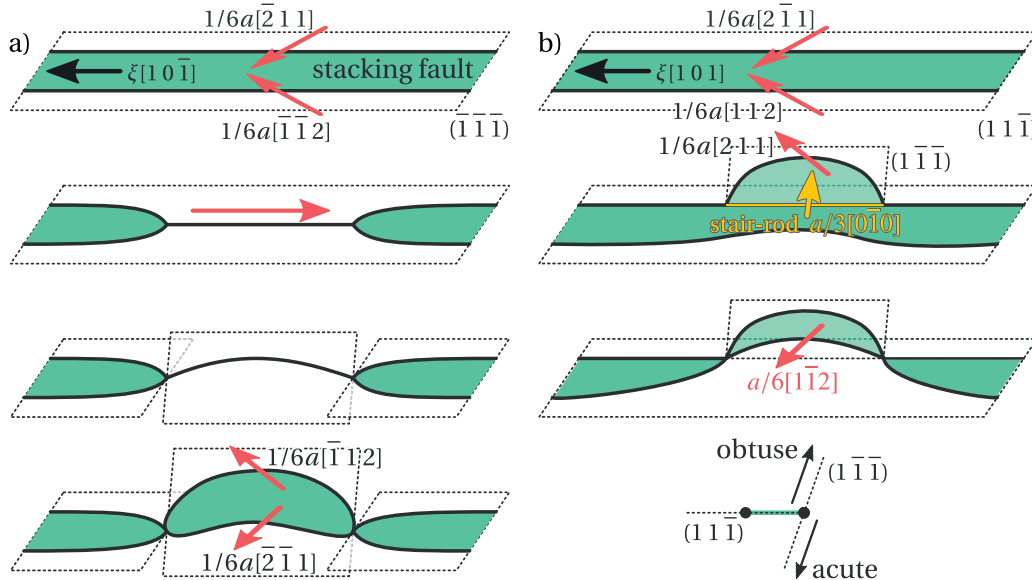


Figure 1.3: a) Schöck-Seeger-Wolf cross-slip mechanism; b) Fleischer mechanism

6. Seeger et al. [126] argued that a process with immediate redissociation would require strongly correlated movement of atoms, and would therefore have low statistical weight.

7. Using Equ. 5.1 and Equ. 5.3 in Ref. [153], with material parameters from Ref. [1], and an effective shear modulus $\mu = \sqrt{(C_{11} - C_{12})C_{44}/2}$, where C_{11} , C_{12} and C_{44} are the cubic elastic constants.

A constriction-free mechanism was proposed by Fleischer [39], see Fig. 1.3. He suggested that the leading Shockley partial dislocation first decomposes into another Shockley partial dislocation on the cross-slip plane and a sessile dislocation with Burgers vector of type $a/3\langle 010 \rangle$ or $a/6\langle 10\bar{1} \rangle$, depending on whether the cross-slip plane makes an obtuse or acute angle with the glide plane. In a second step, the trailing Shockley partial dislocation on the glide plane merges with the sessile dislocation to form the trailing dislocation on the cross-slip plane. Fleischer argued that according to Frank's [85] rule, the product of the first step should have a lower energy than a perfect screw dislocation, hence this mechanism should be preferred to cross-slip involving a line constriction. Marcinkowski et al. [78] calculated the required energy and the critical stress for both mechanisms using a two-dimensional isotropic-elastic model. The critical stress of Fleischer cross-slip is found to be on the order of Gigapascals and to decrease with decreasing stacking fault energy. In a metal with $\gamma_{SF} = 20 \text{ mJ m}^{-2}$ at an applied stress of 500 MPa, the required energies per dislocation length are 0.27 eV \AA^{-1} and 0.2 eV \AA^{-1} for cross-slip onto an obtuse and acute plane, respectively. This energy seems prohibitively high. However, recent calculations of the critical stress with a multiscale technique by Xu et al. [160] indicate that the critical stress of Fleischer's mechanism is only few tens of MPa higher than that of the F-E mechanism. Fleischer cross-slip is sometimes observed in molecular dynamics simulations of deformation [7, 79, 90]. Moreover, cross-slip without full constriction is observed in atomistic transition path calculation when the dislocation line is very short (few b) [26, 57].

1.2.5 Cross-Slip at Heterogeneities

Early on, it was proposed that cross-slip could occur at a heterogeneity in the dislocation line. Stroh already [133] suggested that jogs could facilitate cross-slip. Mechanisms for cross-slip at dissociated superjogs and dislocation intersections were proposed by Hirsch [50] and Washburn [150], respectively. More recently, heterogeneous cross-slip mechanisms were studied using atomistic methods. Generally, these calculations indicate that heterogeneities facilitate cross-slip. Rasmussen et al. [113] demonstrated that cross-slip can be spontaneous if a screw-like constriction is formed at the surface of the crystal. Vegge et al. [142] simulated cross-slip at jogs and found that the energy was reduced by a factor of four. In a series of papers, Rao and coworkers considered cross-slip at mildly attractive intersections with forest dislocations in Ni [103, 104] and Cu [107], at mildly repulsive dislocation intersections in Ni, Cu, and Ni₃Al [109], at surfaces in Ni and Cu [106], and at jogs [108]. In all cases, the activation energy was significantly less than in the homogeneous case, see Tab. 1.2. Thus, cross-slip at heterogeneities should be taken into account when discussing the overall rate of cross-slip. See Ref. [54] for an example where such mechanisms have been incorporated into Discrete Dislocation Dynamics calculations.

1.2.6 Alloying Effects

In most studies of cross-slip to date, the metal was assumed to be pure. Extension to alloys is primarily considered by assuming that the effects of alloying are limited to changing the relevant average material properties entering the F-E model. In particular, alloying is considered mainly to change the stacking fault energy γ_{SF} , with decreases in γ_{SF} leading to

1.3. Transition State Theory

Table 1.2: Factors by which the activation energy for cross-slip is reduced at heterogeneities, compared to homogeneous cross-slip; “—” = spontaneous cross-slip

heterogeneity	material	factor	reference
jog	Cu	4	[142]
jog	Cu	4–5	[108]
surface	Cu	—	[113]
surface	Cu, Ni	20–30	[106]
dislocation intersections	Ni	2–5	[103]
dislocation intersections	Cu, Ni	2.5–6 (Cu), 3–20 (Ni)	[107]
dislocation intersections	Cu, Ni, Ni ₃ Al	—	[106]

wider dissociation of the initial partial dislocations, and thus a higher energy for forming the constriction. A more accurate dimensionless measure for the dissociation width, and hence the tendency for cross-slip, is $\gamma_{SF}/\mu b$, the ratio of stacking fault energy to shear modulus and Burgers vector magnitude [19]. However, this reduction to a single parameter is a simplistic model of the alloying effect that misses important mechanisms, as we will see. Surprisingly, there have been few dedicated studies of alloying effects on FCC cross-slip to date.

Hong and Laird [53] estimated the propensity for cross-slip based on a model of the energy that is required to recombine a straight dissociated dislocation. The effect of solutes is to create a frictional force that impedes recombination, and therefore cross-slip. However, this model ignores the cross-slip mechanism. Furthermore, it is not immediately clear why solutes would always impede cross-slip. It seems equally possible that they locally constrict the dislocation, which would facilitate cross-slip. Andrews et al. [2] developed an isotropic-elastic model to compute the energy to form a Stroh constriction using a line tension model, but with the assumption of solute segregation to the dissociated dislocation. The assumption of segregation leads to strong pinning of the initial dislocation, leading to very high energy barriers for cross-slip (e.g. in Cu-Zn, from approximately 1.64 eV at 0.0025 at.% Zn to ca. 10.8 eV at 20 at.% Zn). This assumption is probably not valid for considering materials being deformed steadily at normal strain rates and moderate temperatures, where solute diffusion is too slow to cause significant segregation near dislocations that are temporarily pinned at obstacles. An atomistic study of cross-slip in solid solutions without segregation was conducted by Du et al. [25], who calculated the activation energy for cross-slip in Ni-2 at.% Al and Ni-10 at.% Al, using the Nudged Elastic Band [81] method. The activation energy increased by 0.2 eV if an Al-Al solute pair was formed in the process, due to strong Al-Al near-neighbor repulsion in Ni-Al; this result will echo our broader findings below. A similar methodology was used by Wen et al. [151, 152] for Ni with very ordered arrangements of interstitial H solutes. Overall, there are no systematic studies of cross-slip in realistic FCC solid solution alloys that would reveal the clear effects of alloying on this important process.

1.3 Transition State Theory

In chemistry and physics, one is often interested in the rate r (events/second) at which a system of atoms undergoes a change of configuration, which could be a chemical reaction, or

the movement of a defect in a crystal. Dealing with such problems is the subject of reaction rate theory and, more specifically, transition state theory [37]. Here, we are interested in dislocation cross-slip, which is a particular change of configuration of the atoms in a defective crystal. The purpose of this section is to introduce some basic rate expressions and to motivate calculation of the *activation energy* ΔE_{act} for cross-slip, which is a central quantity in this thesis. For a more elaborate discussion, with emphasis on rates of dislocation motion, see Ref. [122].

Frequently, the rate is described using the Arrhenius equation [4],

$$r(T) = A \exp\left(-\frac{\Delta E_{\text{act}}}{k_B T}\right), \quad (1.7)$$

where k_B is Boltzmann's constant, T is temperature, and A is a constant. ΔE_{act} is the maximum energy encountered during transformation from the initial into the final state, relative to the energy of the initial state. The exponential term is typically interpreted as the likelihood of overcoming the energy barrier, and A as the attempt frequency. Frequently, it is assumed that A is on the order of the Debye frequency ν_D , i.e. $\sim 10^{13} \text{ s}^{-1}$. Molecular dynamics simulations of screw dipole annihilation under stress indicate that the rate of cross-slip of short ($30b$ [144, 145] or $28b$ [83]) and longer ($200b$ [92]) dislocations can be described with Eq. 1.7. However, Vegge et al. [144, 145] measured $A=2 \times 10^{15} \text{ s}^{-1}$. The high frequency compared to the Debye frequency was explained with translational symmetry along the dislocation line.

The Arrhenius equation is an empirical relation. In transition state theory, the rate is derived from the motion of the atoms using statistical mechanics. It is useful to introduce some elements of this theory, which will reappear in Sec. 2.3.2, where a method for calculating ΔE_{act} is explained. For a detailed explanation of the theory see Ref. [122] or Ref. [48]. Note that we consider classical systems; quantum effects are ignored. The state of a system of N atoms is described by $3N$ positions and $3N$ velocities. This state can be envisioned as a $6N$ dimensional vector in *phase space*. If one ignores the exact values of the velocities, it is sufficient to consider the $3N$ dimensional vector \mathbf{R} of atomic coordinates in *configuration space*. The potential energy of the system is a single-valued function of \mathbf{R} . Hence, the configuration is a point on a $(3N - 1)$ -dimensional *potential energy surface* (PES). This surface consists of basins of attraction around local minima, which are separated by saddle points, see Fig. 1.4. In thermal equilibrium, the system spends most of the time moving around randomly in a particular basin. From time to time, velocity fluctuations lead to crossing of a saddle point and the system moves to the next basin. Two local minima A and B may correspond to two physically significant states, e.g. a system with a dislocation before and after cross-slip. We henceforth refer to these minima as initial and final state. The most likely path for the transition is the *Minimum Energy Path* (MEP) between A and B . Invoking the picture of a mountainous landscape, this is the path through the valley, and across the point P on the saddle with the lowest elevation. Using the harmonic approximation for the vibration of atoms, Vineyard [146] derived the rate of atomic jump processes in solids as

$$r = \left(\frac{\prod_{j=1}^{3N} \nu_j}{\prod_{j=1}^{3N-1} \nu'_j} \right) \exp\left(-\frac{(V(P) - V(A))}{k_B T}\right), \quad (1.8)$$

where $\nu_1 \dots \nu_N$ and $\nu'_1 \dots \nu'_{N-1}$ are the real-valued⁸ normal frequencies for vibration around A and P , respectively, and $V(A)$ and $V(P)$ are the values of the potential energy at A and P .

1.3. Transition State Theory

$V(P) - V(A) = \Delta E_{\text{act}}$, hence this equation is similar to Eq. 1.7. For cross-slip, Vegge et al. [145] derived

$$A = \zeta \frac{\omega_0}{2\pi} \left(\frac{M\omega_0}{2\pi k_B T} \right)^{1/2}, \quad (1.9)$$

where ζ is the length of the dislocation, M is a mass associated with a constriction, and ω_0 is a frequency for oscillations in the width of a straight dislocation. A linear dependence of the rate of cross-slip on ζ has been observed by Oren et al. [92].

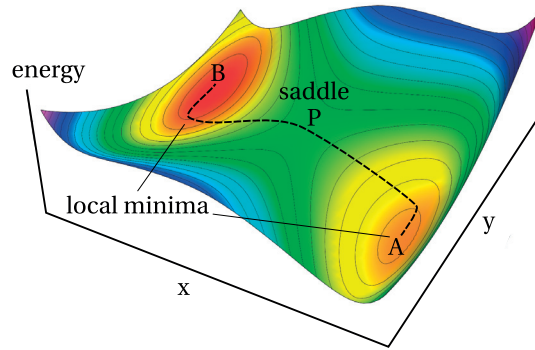


Figure 1.4: Two-dimensional model Potential Energy Surface [59] with two minima separated by a saddle point; dashed line: approximate minimum energy path

8. At P , the normal mode in the direction of the path has a negative eigenvalue and an imaginary frequency. This is the missing frequency in the product in the denominator of Eq. 1.8

2 Methods

Having reviewed the theoretical background, we can now turn to the simulation methods used in this thesis. In Sec. 2.1, we briefly review the interatomic potential models that were used in this work. The alloy systems for which simulations were carried out are introduced in Sec. 2.2. In Sec. 2.3, we explain the transition path calculations. In particular, we explain the setup, the calculation method, and how to perform such calculations at finite stress. Finally, in Sec. 2.4, we explain how solute-dislocation and solute-solute binding energies were calculated.

2.1 Atomistic Calculations with Classical Potentials

A typical configuration for calculating the cross-slip transition path consists of approximately 10^5 atoms. It is not feasible to simulate such a large number of atoms with first principles methods, therefore energies and forces were calculated using classical potentials. The Embedded Atom Method (EAM) [20] is sufficient for FCC metals and was therefore used throughout this work. All simulations were performed with the LAMMPS [96] software package.

A solid solution can be modeled in two ways. A straightforward way is to assign to the atomic sites a random distribution of atom types that is consistent with the desired concentration. Alternatively, a single “average” atom type can be used. The corresponding “average alloy” ideally has the same average properties as the real random alloy, but is free from concentration fluctuations. The EAM and the corresponding first-order average-atom approximation [131, 141] are discussed in the following.

2.1.1 Embedded Atom Method

In the EAM, the energy of each atom is the sum of pairwise interaction energies and an embedding energy, which depends on the local electron density. Consider an alloy with N_T distinct atom types and a total number of N atoms. Let X and Y refer to atom types, and i and j to atom sites. Denote distances between sites by r_{ij} . Furthermore, let $\{s_{i,X}\}$ be occupation

Chapter 2. Methods

variables, where $s_{i,X} = 1$ if the atom at site i is type X and zero otherwise. The total energy is

$$E(\{s_{i,X}\}) = \sum_i^N \sum_X^{N_T} s_{i,X} F_X(\rho_i) + \frac{1}{2} \sum_{i,j \neq i}^N \sum_{X,Y}^{N_T} s_{i,X} s_{j,Y} V_{XY}(r_{ij}), \quad (2.1)$$

where

$$\rho_i = \sum_{j \neq i}^N \sum_X^{N_T} s_{j,X} \rho_X(r_{ij}), \quad (2.2)$$

and where $V_{XY}(r_{ij})$ is the pair potential function, $F_X(\rho_i)$ the embedding energy functional, ρ_i the total electron density at site i , and $\rho_X(r_{ij})$ the contribution of an X -atom at site j to ρ_i .

Note that all $V_{XY}(r_{ij})$ and $\rho_X(r_{ij})$ are radially symmetric. Thus, the EAM represents a reasonable approximation for materials without preferred bonding angles, such as the FCC metals.

2.1.2 Average Atom Approximation

Random alloys can be modeled using the average atom approximation. The central idea is to replace the true atom types with a single fictitious “average” atom type (A-atom), which gives approximately the same average energy. The A-atom EAM potential was derived by Smith et al. [131] and Varvenne et al. [141].

Averaging Eq. 2.1 over occupation variables $s_{i,X}$, Varvenne et al. obtain the preliminary result

$$\langle E \rangle = \sum_i^N \sum_X^{N_T} c_X \langle F_X(\rho_i) \rangle + \frac{1}{2} \sum_{i,j \neq i}^N \sum_{X,Y}^{N_T} c_X c_Y V_{XY}(r_{ij}), \quad (2.3)$$

where c_X is the concentration of type X and $\langle \dots \rangle$ indicates averaging. This equation is valid under the assumption that the $s_{i,X}$ are uncorrelated in the random alloy, i.e. $\langle s_{i,X} s_{j,Y} \rangle = c_X c_Y$.

Eq. 2.3 is simplified further by expanding the embedding energy in a Taylor series around the average electron density. Averaging eliminates the first-order term in the series, hence $\langle F_X(\rho_i) \rangle = \langle F_X(\langle \rho_i \rangle) \rangle + \mathcal{O}(\rho_i - \langle \rho_i \rangle)^2$. Neglecting the second order term leads to a simple expression for the average energy,

$$\langle E \rangle = \sum_i^N F_A(\langle \rho_i \rangle) + \frac{1}{2} \sum_{i,j \neq i}^N V_{AA}(r_{ij}), \quad (2.4)$$

where

$$\begin{aligned} F_A(\langle \rho_i \rangle) &= \sum_X^{N_T} c_X F_X(\langle \rho_i \rangle), \\ V_{AA}(r_{ij}) &= \sum_{X,Y}^{N_T} c_X c_Y V_{XY}(r_{ij}), \\ \langle \rho_i \rangle &= \sum_{j \neq i}^N \sum_X^{N_T} c_X \rho_X(r_{ij}). \end{aligned} \quad (2.5)$$

Thus, the EAM potential functions of the A-atom are the concentration-weighted averages of the corresponding pure element functions. In addition, one takes the weighted average of the pure element masses m_X to obtain the mass m_A of the A-atom, which is required in molecular dynamics simulations:

$$m_A = \sum_X^{N_T} c_X m_X. \quad (2.6)$$

Varvenne et al. [141] showed that the A-atom accurately predicts average properties of true random alloys, for example the lattice parameter, the elastic constants, and the stacking fault energy. Furthermore, it facilitates the calculation of solute-dislocation binding energies, which would be cumbersome using a direct approach. However, the A-atom cannot predict properties that are controlled by solute fluctuations, e.g. the Peierls stress.

The study by Varvenne et al. was limited to zero temperature. Recently, Nöhring and Curtin [89] verified the A-atom approach for finite temperature calculations. The lattice parameter, the elastic constants and the Helmholtz free energy of equiatomic FeNiCr and Ni+15 at.% Al were calculated at temperatures between 0 K and 700 K. It was shown that the A-atom predicts the mean lattice parameter and the elastic constants of true random alloys accurately, to within a few percent. The difference in vibrational entropy was at most $0.05 k_B$ /atom. Hence, the A-atom is also useful for approximating true random alloys at finite temperature.

2.2 Selected Alloys

Our purpose is to demonstrate the effect of alloying on cross-slip across a range of FCC alloys by using model alloy materials over a wide range of solute concentrations. Here, we consider alloys of Al+(2, 6, 10, 14, 18, 22) at.% Mg, Ni+(2, 4, 8, 10, 12, 15) at.% Al and Cu+(10, 22, 33, 68, 79, 90) at.% Ni as described by the EAM potentials for Al-Mg [74], Ni-Al [98], and Cu-Ni [91]. While these model materials may exceed the solute concentrations of the corresponding real alloy materials (e.g. Al-Mg is limited to ~5 at.% Mg and Ni-Al is limited to ~13 at.% Al), the chosen systems serve to cover a range of situations that span real materials (e.g. low and high stacking fault energies; large and small solute misfit volumes; weak and strong solute-solute interaction energies). Results will show that alloying can be significant even at low concentrations (e.g. Al+2 at.% Mg). Furthermore, the main new features of the present study are expected to be relevant to the emerging classes of FCC High Entropy Alloys (HEA) [162], which are essentially highly concentrated multicomponent solid solutions.

Some basic properties of average and random Ni-Al, Cu-Ni and Al-Mg alloys with the aforementioned compositions are listed in Tab. A.1, Tab. A.2 and Tab. A.2 in App. A.1. The tables show the lattice parameter, the cubic elastic constants, the stacking fault energy and the measured screw dissociation width. Methods for calculating these properties are also explained in App. A.1.

2.3 Calculating the Transition Path of Cross-Slip

There are a number of atomistic methods for determining the transition path of a microscopic process, such as the Nudged Elastic Band method [59, 81] or the String method [30]. They provide information about the mechanism and activation energy of the process. Here, this kind of calculation was used to study cross-slip in random and average alloys. The setup and execution of these calculations is explained below. Sec. 2.3.1 deals with the procedure for generating initial and final states. The main method, a variant of the String method, is explained in Sec. 2.3.2. The section closes with a discussion of transition path calculations at finite Escaig stress.

2.3.1 Initial and Final States

The atomic configurations for transition path calculations were cylinders with axis parallel to the $[10\bar{1}]$ crystal direction, see Fig. 2.1. Periodic boundary conditions were applied along this direction. The cylinders were subdivided into a shell and a core region (not to be confused with the dislocation core). Atoms in the shell were kept fixed. Its width was larger than two times the cutoff radius of the potential, hence atoms in the core were not influenced by the free surface. If not stated otherwise, the diameter of the core was $10\sqrt{3}a$ and the length of the cylinder was $40b$. These dimensions were chosen based on a parameter study with pure Ni, see App. A.4. The cylinders contained a screw dislocation with complete Burgers vector $a/2[10\bar{1}]$ and line direction $[\bar{1}01]$, which dissociates into Shockley partial dislocations $a/6[\bar{2}11]$ and $a/6[\bar{1}12]$ on the (111) plane, or into $a/6[\bar{2}11]$ and $a/6[\bar{1}12]$ on the $(\bar{1}\bar{1}\bar{1})$ plane. In transition path calculations, it was assumed that the former pair is the initial state, and the latter the final state. Accordingly, the (111) and $(\bar{1}\bar{1}\bar{1})$ planes are called glide and cross-slip plane, respectively.

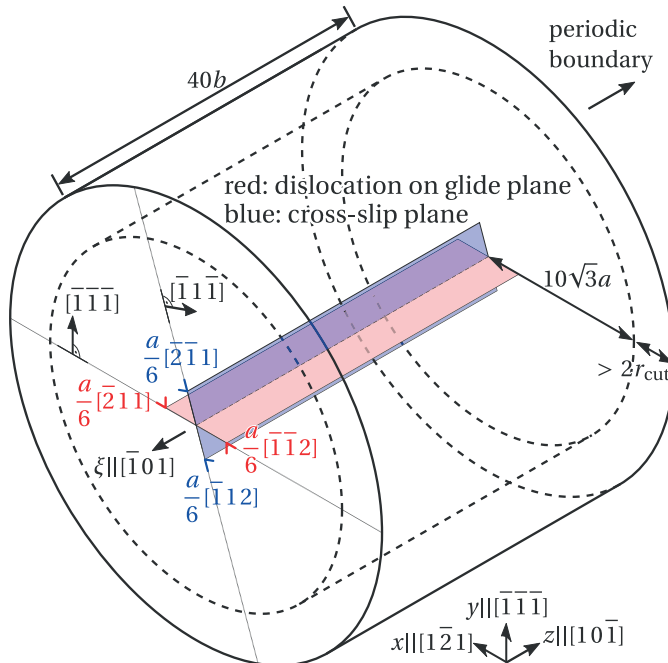


Figure 2.1: Setup for transition path calculations.

2.3. Calculating the Transition Path of Cross-Slip

Generating initial and final states is complicated by the need for consistent cut planes. The cut plane of a dislocation is the plane across which displacements are discontinuous, see Fig. 1.1. If the dissociated dislocations were created by directly inserting the Shockley partial dislocations, then each of them would have its own cut plane, and the initial and final state would be inconsistent. The transition path between them would include extra displacements to transform one cut into the other. Thus, both states were generated by inserting the complete $a/2[10\bar{1}]$ dislocation with cut plane $(\bar{1}\bar{1}\bar{1})$. In one copy of the pristine configuration the dislocation was inserted at the center of the cylinder. During a subsequent energy minimization, it would dissociate either on the glide or on the cross-slip plane. In another copy the center of the dislocation was shifted slightly in the $[1\bar{2}1]$ or $[\bar{1}21]$ direction, which would result in dissociation on the complementary plane. The shift was typically less than 2–3% of $a/\sqrt{3}$, the distance between $\{111\}$ planes. However, the required shift was not known a priori, therefore several trials were typically required. In all cases, the perfect dislocation was inserted by displacing all atoms according to Stroh's [134] anisotropic-elastic solution. The energy was minimized using the conjugate gradient (CG) algorithm [49] and the FIRE algorithm [8] with the parameters in Tab. 2.1. Only atoms in the interior were moved. The minimization was considered converged when the norm of the $3N$ -dimensional force vector fell below 10^{-6} – 10^{-8} eV Å $^{-1}$. However, this threshold could not be achieved in some calculations with Cu-Ni and Al-Mg. The force norm would initially decrease but then start to oscillate around a value above the threshold. These oscillations were interpreted as an effect of potential tabulation, since they occurred more frequently in Al-Mg, where the potential is relatively coarsely discretized (500 points). The maximum observed residual force was 4×10^{-4} eV Å $^{-1}$ in calculations with Al-Mg, and 7×10^{-6} eV Å $^{-1}$ in calculations with Cu-Ni. However, examination of the energies and forces for a number of cases indicates that the total energy decreases by no more than 1×10^{-5} eV if the force norm is reduced from 10^{-3} – 10^{-4} eV Å $^{-1}$ to below 1×10^{-6} eV Å $^{-1}$, hence this level of convergence is sufficient for our purposes.

Table 2.1: FIRE parameters; see Ref. [8] for reference.

parameter	N_{\min}	f_{inc}	f_{dec}	f_{α}	α_{start}	Δt_{\max}	Δt (initial)
value	20	1.1	0.5	0.99	0.25	2 fs	1 fs

The aforementioned method for obtaining the complementary dissociated state by shifting the center of the dislocation relies on the fact that the two pairs of Shockley partial dislocations are symmetrically equivalent and therefore indistinguishable in the chosen simulation cell if the metal is pure. Thus, a minute perturbation suffices to bias the complete dislocation towards dissociation on a particular plane. In a true random alloy, however, there are additional perturbations from solute atoms, which may strongly favor dissociation on one plane. Thus, larger center shifts and more trials may be necessary to obtain the complementary state, and the process would be more cumbersome and harder to automatize. In order to avoid this problem, average alloy initial and final states were used as templates for generating the corresponding random alloy configurations. After insertion of the dislocations, the average alloys were converted into true random alloys by replacing the A-atoms with a random distribution of true atoms types that was consistent with the desired concentration. The distribution was generated by defining a true atom type for each atom, such that the correct

Chapter 2. Methods

concentrations were achieved, and then randomly shuffling¹ the type-to-atom mapping.

However, recall that the average alloy approximation is not exact. Both lattice parameter and elastic constants deviate slightly from the corresponding mean random alloy values, see Fig. A.1. When the average alloy configurations are converted into random alloys, there is hence an error in the simulation cell size and the displacement field of the dislocation, which was calculated using average alloy material properties. The error due to the lattice parameter difference was partially corrected by scaling the configurations by the ratio of lattice parameters. The error caused by the difference in elastic constants could not be corrected, but is expected to be small. Note that the maximum relative difference between average and random alloy elastic constants is typically on the order of a few percent. In the Ni-Al system it is 6.1 % in C_{11} at 15 at.% Al. In Al-Mg, the maximum differences are 6.0 % in C_{11} and 7.5 % in C_{44} at 22 at.% Mg, see Fig. A.1 in App. A.1. In Cu-Ni, the relative difference is less than 1 % for all components, at all concentrations. Anyway, it will be shown that changes of average material properties have a negligible effect on the cross-slip activation energy, compared to solute concentration fluctuations.

After changing atom types and scaling the configurations, the potential energy of the core atoms was minimized using CG and FIRE. During minimization, the dislocation can adapt to the random solute environment. In some cases, it may lower its energy by slipping away from the center, towards a favorable solute fluctuation. Such slip is undesirable, since it results in an additional energy change, which is not associated with cross-slip. This contribution comes from movement against image forces, which, in turn, result from the fixed boundary conditions. It was avoided as follows. The random alloy configurations were discarded when the amount of slip in the initial or final state exceeded a threshold value of 2 Å. The displacement of the dislocation was measured by calculating the average position of the non-FCC atoms in the core as obtained from a Common Neighbor Analysis (CNA) [52] with cutoff $(\sqrt{0.125} + 0.5)a$. In some cases, the displacement criterion was applied only to the initial state. The dislocation was then allowed to slip after cross-slip, but transition paths were later truncated by selecting a new final state, where the dislocation had slipped less than the threshold value.

2.3.2 String Method

The goal of the calculation is to find a Minimum Energy Path (MEP) between initial and final state through $3N$ -dimensional configuration space. The MEP fulfills the condition that the force component \mathbf{F}^\perp perpendicular to the path is zero everywhere. The activation energy ΔE_{act} is the maximum energy along this path. In practice, one works with a discrete approximation of the MEP. Thus, the path is discretized into a chain of N_S states or “images”, see Fig. 2.2. Typically, one demands that the images are evenly spaced along the path or close to maxima. A standard method for calculating transition paths, which is implemented in LAMMPS, is the Nudged Elastic Band (NEB) [59, 81] method, see App. A.2. However, this method was observed to be unstable in preliminary calculations. Frequently, the length of the path would grow out of bounds², and intermediate states would achieve extremely high energies, of up to several

1. Using `numpy.random.RandomState.shuffle` from the Python-Numpy package [149], which implements the Fisher-Yates [38] shuffle.

2.3. Calculating the Transition Path of Cross-Slip

hundreds or thousands of electron volts. A modified version of the Simplified and Improved String [29] method turned out to be more stable and was used instead. The method was implemented using the Python interface to LAMMPS.

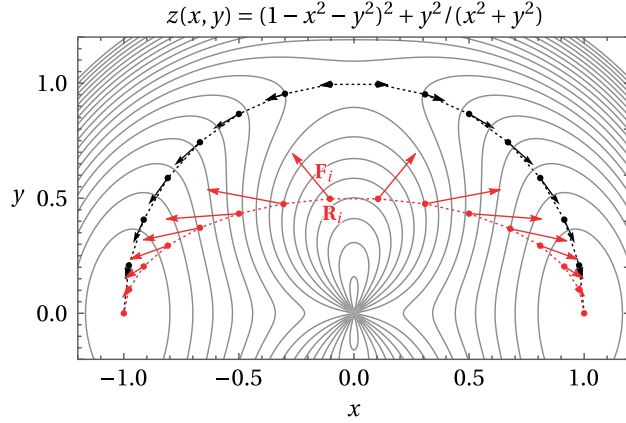


Figure 2.2: Transition path calculation on a 2D model landscape $z(x, y)$; dots represent images and vectors indicate direction and magnitude of the local gradient; the unconverged path (red) has perpendicular force components; the converged path (black) has zero perpendicular force

Consider an initial guess for MEP, i.e. the collection of $3N$ -dimensional vectors \mathbf{R}_i ($i = 1 \dots N_S$) that store the atomic coordinates. In the modified String method as described in Ref. [29], each image moves in the direction of its gradient on the $(3N - 1)$ -dimensional PES, i.e.

$$\dot{\mathbf{R}}_i = -\nabla V_i, \quad (i = 1 \dots N_S), \quad (2.7)$$

where $\dot{\mathbf{R}}_i$ is the $3N$ -dimensional vector of atomic velocities and ∇V_i is the gradient of the potential energy of atom i . Integrating Eq. 2.7 moves the images towards a local minimum of the PES, which also reduces \mathbf{F}_i^\perp , and thus moves them closer to the MEP. However, without further constraints, the images would eventually end up in the local minimum. Thus, after each integration step, they are moved back to their ideal position along the path by interpolation. *Reaction coordinates* \hat{s}_i are introduced to specify the positions,

$$\hat{s}_i = \frac{s_i}{s_{N_S}},$$

where (2.8)

$$s_1 = 0,$$

$$s_i = s_{i-1} + |\mathbf{R}_i^* - \mathbf{R}_{i-1}^*| \quad (i = 2 \dots N_S),$$

and where \mathbf{R}_i^* is the vector of atomic coordinates of image i after the integration step. In this thesis, an equal arc-length parameterization is used throughout, i.e. the ideal reaction coordinates are $\hat{s}_{i,\text{ideal}} = (i - 1)/(N_S - 1)$. After the integration step, $\hat{s}_i \neq \hat{s}_{i,\text{ideal}}$. The correct reaction coordinates are enforced by interpolation of the atomic coordinates. If $\hat{s}_{i,\text{ideal}}$ lies in the interval $[\hat{s}_l, \hat{s}_r]$, then, using linear interpolation,

$$\mathbf{R}_i = \mathbf{R}_l^* + \frac{\hat{s}_{i,\text{ideal}} - \hat{s}_l}{\hat{s}_r - \hat{s}_l} (\mathbf{R}_r^* - \mathbf{R}_l^*). \quad (2.9)$$

2. According to Kolsbjerg et al. [65], the reason for divergence is that the NEB “spring forces”, which should keep the images equispaced, only penalize differences between segment lengths, but not total path length.

Chapter 2. Methods

Under ideal conditions, the MEP is a stationary state of the dynamics given by Eq. 2.7 in conjunction with the interpolation scheme [29]. An image that is already on the path moves only downhill along the path in the integration step, and the interpolation step brings it back to its ideal position.

Here, the String method was implemented using the Python interface to LAMMPS and some modifications were made to the original scheme. Atoms were moved by performing energy minimization in LAMMPS. The parameterization was checked only every 100 iterations of the minimizer. The atomic coordinates were then extracted and interpolated linearly as in Eq. 2.9. We refer to these outer iterations as re-parameterizations. The FIRE [8] or QUICKMIN [59, 127] algorithms were used in the minimization. The dynamics are then not those in Eq. 2.7, but modified Newtonian dynamics, where the velocity and force vector are mixed to obtain a velocity with a stronger downhill component. In addition, velocities are zeroed whenever the dot product of velocity and momentum is positive, i.e. whenever a state is moving uphill on the PES. Therefore, the motion of states lying on the path is biased to stay on the path, and it is expected that the MEP is still a stationary state. The convergence of our String method calculations of MEPs for cross-slip is discussed in App. A.3.

2.3.3 Initial Guess for the Path

If not mentioned otherwise, the initial guess for the path \mathbf{R}_i ($i = 1 \dots N_S$) was created by linearly interpolating between the initial and final state \mathbf{R}_1 and \mathbf{R}_{N_S} , respectively. This is the standard method, also often used for NEB [59]. However, there is no proof that the converged path obtained with this initial guess is the path with the lowest possible ΔE_{act} .

In some cases, average alloy calculations were started with a guess for the path that is closer to a F-E path than the default guess. First, a guess for the transition state of the F-E mechanism was generated. A $20b$ long piece of the initial state and a $20b$ long piece of the final state were combined to form a complete $40b$ long configuration. Smooth constrictions were created at the interface between the two parts by linearly interpolating over a length of 15\AA along z between the atomic coordinates in the initial and undissociated state, and over another 15\AA between the coordinates in the undissociated and final state. The initial guess for the path was created by linearly interpolating between atomic positions in the initial, transition and final state.

2.3.4 Application of an Escaig Stress

Stress effects on cross-slip were studied by performing transition path calculations with stressed configurations. We make the usual distinction between resolved stresses that couple to the edge parts of the partial dislocations (Escaig stresses), and resolved stresses that couple to the screw parts (Schmid stresses). The former change the splitting width and the latter cause either regular slip or bow-out. Consider the coordinate system of Fig. 2.1. By resolving the applied stress tensor σ_{ij} ($i, j = 1, 2, 3$; corresponding to the x -, y - and z -directions) onto the slip planes and partial Burgers vector components, one obtains the following Escaig and

Schmid stresses on the glide and cross-slip planes, respectively:

$$\begin{aligned}\tau_{\text{glide}}^{\text{Esc}} &= \sigma_{12} \\ \tau_{\text{glide}}^{\text{Sch}} &= -\sigma_{23} \\ \tau_{\text{cross}}^{\text{Esc}} &= \frac{1}{9} \left(7\sigma_{12} + 2\sqrt{2}(\sigma_{11} - \sigma_{22}) \right) \\ \tau_{\text{cross}}^{\text{Sch}} &= \frac{1}{9} \left(2\sqrt{2}\sigma_{13} - \sigma_{23} \right).\end{aligned}\tag{2.10}$$

Using Hooke's law, one can find a strain tensor ε_{ij} ($i, j = 1, 2, 3$) that yields a pure Escaig stress $\tau_{\text{glide}}^{\text{Esc}}$ on the glide plane ($\tau_{\text{glide}}^{\text{Sch}} = \tau_{\text{cross}}^{\text{Sch}} = \tau_{\text{cross}}^{\text{Esc}} = 0$), for example

$$\begin{aligned}\varepsilon_{11} &= -\varepsilon_{22} - \varepsilon_{33} \\ \varepsilon_{22} &= \frac{7}{8\sqrt{2}} \frac{1}{C_{44}} \tau_{\text{glide}}^{\text{Esc}} \\ \varepsilon_{33} &= \frac{3}{16\sqrt{2}} \frac{(C_{11} - C_{12} - 2C_{44})}{(C_{11} - C_{12}) C_{44}} \tau_{\text{glide}}^{\text{Esc}} \\ \gamma_{12} &= 2\varepsilon_{12} = \sqrt{8} \left(\frac{4}{7} \varepsilon_{22} - \varepsilon_{33} \right) \\ \gamma_{23} &= \gamma_{13} = 0,\end{aligned}\tag{2.11}$$

where γ_{ij} ($i, j = 1, 2, 3$, with $i \neq j$) are engineering shear strains. For a pure Escaig stress $\tau_{\text{cross}}^{\text{Esc}}$ on the cross-slip plane ($\tau_{\text{glide}}^{\text{Sch}} = \tau_{\text{cross}}^{\text{Sch}} = \tau_{\text{glide}}^{\text{Esc}} = 0$), one may impose

$$\begin{aligned}\varepsilon_{11} &= -\varepsilon_{22} - \varepsilon_{33} \\ \varepsilon_{22} &= -\frac{9}{8\sqrt{2}} \frac{1}{C_{44}} \tau_{\text{cross}}^{\text{Esc}} \\ \varepsilon_{33} &= \frac{3}{16\sqrt{2}} \frac{(C_{11} - C_{12} - 2C_{44})}{C_{44}(C_{11} - C_{12})} \tau_{\text{cross}}^{\text{Esc}} \\ \gamma_{12} &= 2\varepsilon_{12} = -\sqrt{8}\varepsilon_{33} \\ \gamma_{23} &= \gamma_{13} = 0.\end{aligned}\tag{2.12}$$

The desired strain components were imposed on all atoms. When applying a strain ε_{33} , the simulation cell was deformed as well, since the z -direction is periodic. The energy was then minimized using CG and FIRE. Strained random alloy configurations were prepared by scaling the corresponding average alloy configurations and subsequently replacing the A-atoms by real atom types, as described in Sec. 2.3.1. Afterwards, the energy was minimized using CG and FIRE.

2.4 Solute Binding Energies

The binding energy of a solute (s) at position (x, y, z) relative to a defect is the energy associated with moving the solute from infinity to (x, y, z) , i.e.

$$\Delta E_{\text{s-defect}} = E_{\text{s-defect}} - E_s - E_{\text{defect}} - 2E_{\text{pure}},\tag{2.13}$$

Chapter 2. Methods

where $E_{s\text{-defect}}$ is the energy of the atomic configuration with the solute *and* the defect, E_s and E_{defect} are the energies with an isolated solute and defect, respectively, and E_{pure} is the energy of the pure configuration.

Solute-dislocation binding energies were calculated as follows. The basic configuration was a periodic cylinder like the one shown in Fig. 2.1. The radius was $20\sqrt{3}a$, which is twice the value used in transition path calculation. The length of the cylinder was only $6b$, because only individual solutes are studied and so the cell need only be slightly longer than the cutoff radius of the interatomic potential. The configuration was made of A-atoms. A screw dislocation was inserted on the initial plane and relaxed, as described in Sec. 2.3.1. One row of atoms in the core of each partial dislocation was then fixed to prevent the dislocation from slipping towards or away from the solute during subsequent calculations. The selected rows were the rows of non-FCC coordinated core atoms with the highest or lowest x -coordinate, see Fig. 2.3. Typically, these rows were symmetry-equivalent under two-fold rotation about the z -axis through the center of the dislocation. For each of the 5330 unique atomic sites in this geometry, the solute-dislocation binding energy was computed by inserting the desired solute atom into the desired site (removing the A-atom occupying the site), followed by fully minimizing of the energy using CG and FIRE until the norm of the force vector fell below $1 \times 10^{-6} \text{ eV}\text{\AA}^{-1}$, or after 200 000 iterations, and taking the difference between the potential energy after and before insertion of the solute minus the solute binding energy in the perfect A-atom FCC lattice.

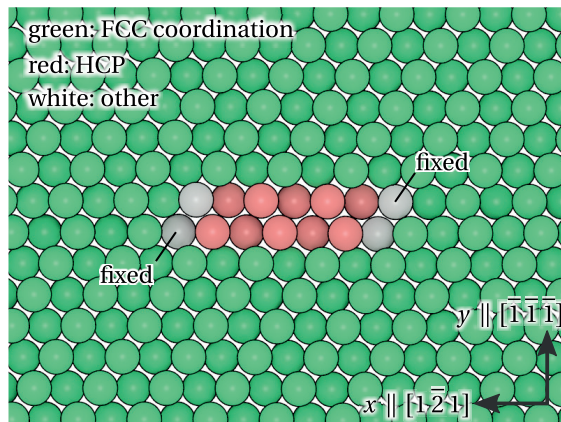


Figure 2.3: Core of a dissociated screw dislocation in Cu+33 at.% Ni, indicating the rows of atoms that are held fixed.

Solute-solute binding energies were computed using a cube of A-atom material aligned along $\langle 100 \rangle$ with edge lengths $40a$ and fully periodic boundary conditions. A neighbor pair of A-atoms was then replaced by the desired real solute pair and the energy was minimized with CG and FIRE. The minimization was stopped when the norm of the force vector fell below $1 \times 10^{-8} \text{ eV}\text{\AA}^{-1}$, or after 20 000 or 30 000 iterations. The solute-solute binding energy is then the potential energy of system containing the solute pair minus twice the energy of a single solute in the perfect A-atom FCC lattice.

3 Cross-Slip of Short Dislocations

Disclaimer

This chapter is adapted from the following article, with permission from the coauthor and the publisher.

W. G. Nöhring and W. A. Curtin. "Dislocation Cross-Slip in FCC Solid Solution Alloys". In: *Acta Materialia* 128 (Apr. 2017), pp. 135–148. ISSN: 13596454. doi: 10.1016/j.actamat.2017.02.027

This chapter deals with the activation energy ΔE_{act} of cross-slip of short (40b) dislocation segments. We present atomistic calculations of ΔE_{act} in average and true random alloys. These calculations show that ΔE_{act} is a random variable with large fluctuations around the mean value. Therefore, average-alloy models are not useful for judging the ease of cross-slip in alloys, and a statistical model is required. We observe that ΔE_{act} correlates with the energy difference ΔE_{end} between the initial and final state. Thus, the distribution of ΔE_{act} can be predicted based on knowledge of the distribution of ΔE_{end} . An analytical model of the standard deviation σ [ΔE_{end}] is developed. The chapter is structured as follows. The atomistic calculations are briefly summarized in Sec. 3.1. The results are presented in Sec. 3.2 and discussed in Sec. 3.3. An analytical model of the distribution of ΔE_{act} is derived and validated in Sec. 3.4. Finally, implications of the results are discussed in Sec. 3.5.

3.1 Calculations

Using the methods explained in Sec. 2.3, we calculated transition paths of cross-slip in average and true random alloys of Al+(2, 6, 10, 14, 18, 22) at.% Mg, Ni+(2, 4, 8, 10, 12, 15) at.% Al and Cu+(10, 22, 33, 68, 79, 90) at.% Ni. For each alloy and concentration, we performed one calculation with the corresponding average alloy and 20 calculations with random alloys. The 20 samples had a random solute distribution corresponding to the specified concentration, but were selected from a larger set, based on the displacement of the dislocation away from the center of the cell, as described in Sec. 2.3.1. In the case of Cu-Ni, the displacement criterion was applied both to the initial and final state, hence the dislocation was close to the center in both states. In the case of Ni-Al and Al-Mg, the criterion was only applied to the

initial state, but transition paths were later truncated by selecting a new final state, where the dislocation had slipped less than the threshold value. The transition paths consisted of 32 images each. Initial guesses were generated by linear interpolation between the coordinates in the initial and final states.

Here, we consider short dislocations. The length of the cylindrical configuration sketched in Fig. 2.1 was $40b$. This length was chosen after studying the dependence of the transition path and energy in pure Ni, see App. A.4. The length $40b$ is the shortest length at which the cross-slip barrier becomes length-independent, i.e. at which there is very limited interaction between the two constrictions formed during cross-slip nucleation. For example, the energy at $40b$ is 1.72 eV and is only 0.02 eV larger at $160b$. This length is therefore a characteristic length of cross-slip nucleation denoted by ζ_{csn} . Different alloys may have different ζ_{csn} because of their different elastic properties. For simplicity, the same length of $\zeta_{\text{csn}} = 40b$ was also used for all other materials, which is ex-post-facto determined to be a good assumption.

The String method as described in Sec. 2.3.2 was used to find the true minimum energy paths between initial and final state. Iterations were stopped when the two-norm of the displacement of each intermediate state relative to its position in the previous iteration was below 10^{-3}\AA , or, if this threshold was not reached, after a total number of 300 re-parameterizations. However, this threshold was reached in all average alloy calculations. Furthermore, the norm of \mathbf{F}^\perp at the transition state was less than $2.3 \times 10^{-4}\text{ eV \AA}^{-1}$, and the absolute maximum was $3.2 \times 10^{-4}\text{ eV \AA}^{-1}$, in Cu+79 at.% Ni. Convergence was slightly worse in random alloy calculations. In Cu-Ni, 35 out of 120 calculations stopped at 300 iterations, in Al-Mg 36 and in Ni-Al 25. The average value of $|\mathbf{F}^\perp|$ at the transition state was highest in Al-Mg; however, the influence of the stopping criterion was negligible. In calculations with less than 300 iterations, the average force was $7.1 \times 10^{-4}\text{ eV \AA}^{-1}$, and in those which stopped at 300 iterations, it was $8.1 \times 10^{-4}\text{ eV \AA}^{-1}$. The absolute maximum force was $3.4 \times 10^{-2}\text{ eV \AA}^{-1}$, in a calculation with Ni+15 at.% Al. See App. A.3 for a more detailed discussion of the convergence.

3.2 Results

3.2.1 Average Alloys

Our calculations yield two important pieces of information. First, they reveal the cross-slip mechanism to be the F-E mechanism. Fig. 3.1 shows the initial, transition and final state of cross-slip in Ni-15 at.% Al. The corresponding states in the other average alloys are similar. Second, they reveal the energy barrier ΔE_{act} , which is the maximum energy encountered along the transition path.

Fig. 3.2 shows representative paths for the three average alloy systems, one particular composition for each binary alloy; results for all other average-alloy systems are similar. The paths are characterized by a steep increase and decrease in energy near the start and end, respectively, and a region of small energy change near the center. The steep increase and decrease in energy correspond to constriction formation and annihilation, respectively, while the plateau in the center corresponds to moving apart of the constrictions. Note that the initial and final state have the same energy, because they are symmetrically equivalent in the

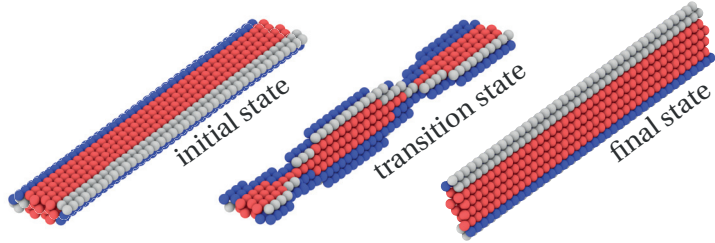


Figure 3.1: Typical states during dislocation cross-slip in average Ni+15 at.% Al. Atoms are colored according to their common neighbor value [52] (red=HCP, blue=BCC, white=other). Atoms in FCC coordination are not shown. Ovito [135] was used for visualization.

homogeneous A-atom materials.

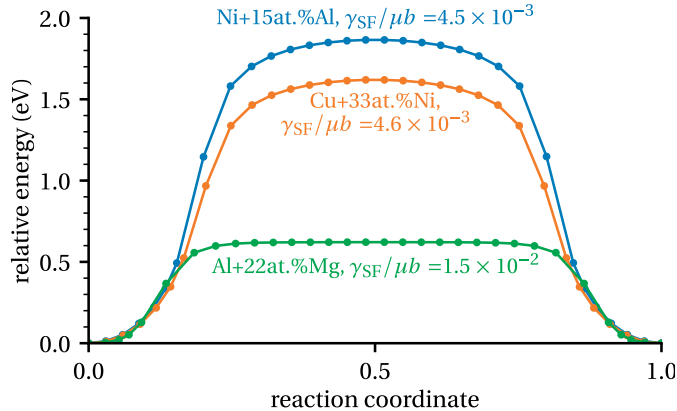


Figure 3.2: Relative energy along the cross-slip transition path in several average alloy systems. The reaction coordinate is the normalized displacement between the initial and final state, see Eq. 2.8. Note that a particular value does not correspond to the same configuration (e.g. same length on cross-slip plane) for two different paths. Thus, the shape of the paths should be compared only qualitatively.

The maximum of each curve is the activation energy ΔE_{act} . As expected, it correlates with the normalized stacking fault energy γ_{SF}/μ_b , which is shown in the figure. Al+22 at.% Mg has the highest γ_{SF}/μ_b and the lowest ΔE_{act} , whereas Ni+15 at.% Al has the lowest γ_{SF}/μ_b and the highest ΔE_{act} . The variation of ΔE_{act} in each alloy system is comparatively small, see Fig. 3.5. For Cu-Ni, the maximum change, relative to ΔE_{act} of Cu, is -0.08 eV, at 79% Ni. In Al-Mg, the maximum change is -0.15 eV, at 18% Mg and in Ni-Al, it is 0.14 eV, at 15% Al. As will be shown below, these changes are small compared to changes of ΔE_{act} due to compositional disorder in true random alloys.

3.2.2 True Random Alloys

Like the average-alloy calculations, the true random alloy calculations predict the F-E mechanism to be the operative cross-slip mechanism. Figs. 3.3a) shows an example of F-E cross-slip in Ni+15 at.% Al. Fig. 3.3a) and b) show the transition states from the paths with the

highest and lowest ΔE_{act} in Ni+15 at.% Al (3.09 and 0.86 eV). Note that the configurations are almost completely dissociated on the cross-slip and glide plane, respectively.

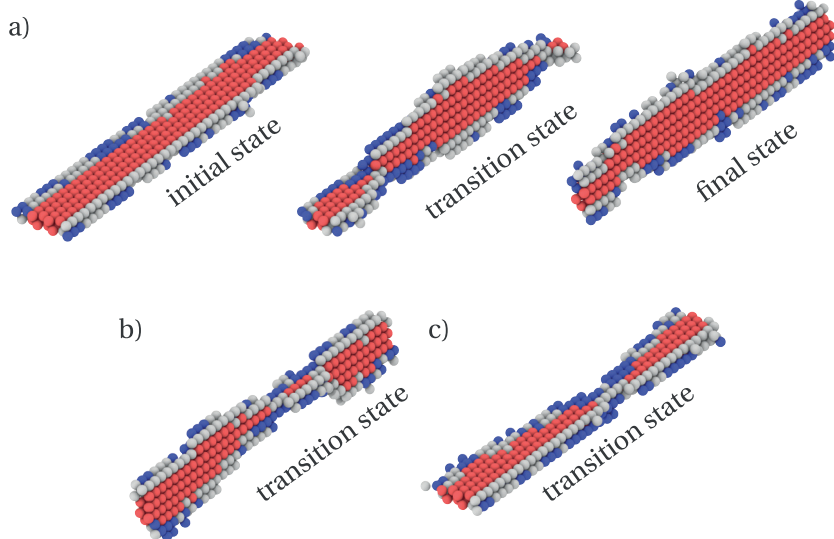


Figure 3.3: Typical states determined by a transition path calculation for random Ni+15 at.% Al: a) states from a path with $\Delta E_{\text{act}} = 1.07$ eV; b) and c) transition states from the paths with the highest and lowest ΔE_{act} in Ni+15 at.% Al (3.09 and 0.86 eV). Atoms are colored according to their common neighbor value [52] (red=HCP, blue=BCC, white=other). Atoms in FCC coordination are not shown. Ovito [135] was used for visualization.

The random alloy calculations predict the same F-E mechanism as found in the average alloy, but they show very different energy profiles. As an example, the transition paths of all the random samples of the Ni+15 at.% Al alloys are shown in Fig. 3.4, with the final state points being corrected as described earlier. The paths are colored according to their activation energy and the transition state is marked with a circle. In contrast to the average alloy calculations, initial and final states in true random alloys have different energies, because the solute field around the dislocation is different on the glide and cross-slip plane. Most importantly, ΔE_{act} varies significantly from sample to sample.

Note that for paths with high ΔE_{act} , the transition state tends to be closer to the final state. The transition states of the paths with the highest and lowest ΔE_{act} have the highest and lowest reaction coordinate, in agreement with the observation that they are almost completely dissociated on the final and initial planes, respectively. This trend agrees with Hammond's [45] postulate, which states that the transition state structure is similar to the initial state when ΔE_{act} is low.

Fig. 3.5 shows ΔE_{act} as a function of concentration. In every alloy system and at every concentration, the distribution of the random alloy energies is much larger than the change of the average alloy energy relative to that of the pure metal. Even in the dilute limit, the lowest value of ΔE_{act} of the random alloy is typically several tenths of an electron volt lower than ΔE_{act} of the corresponding average alloy. The significant statistical distribution of ΔE_{act} is the most important basic result of the random alloy calculations. In the following sections, we will

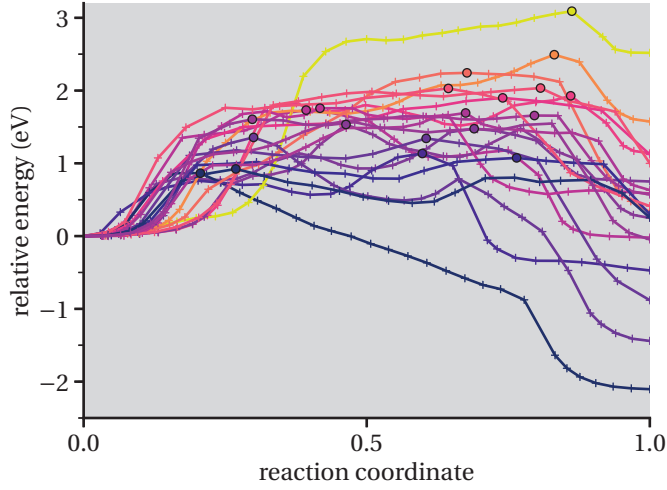


Figure 3.4: Transition paths for specific samples in the true random Ni+15 at.% Al alloy, colored according to ΔE_{act} ; transition states are indicated by circles.

discuss its implications and develop a model for predicting typical values of ΔE_{act} .

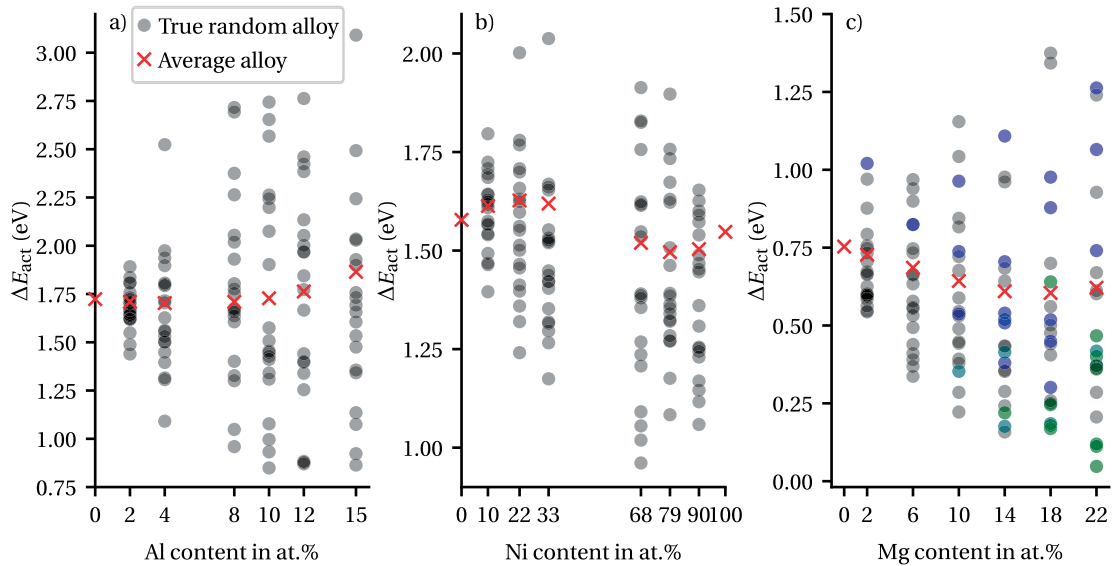


Figure 3.5: Cross-slip activation energies of the 20 individual samples of random alloys for (a) Ni-Al, (b) Cu-Ni, and (c) Al-Mg; also shown are the average alloy values at each composition; in (c) blue markers indicate samples with two nuclei; green markers indicate samples with a partially cross-slipped state with negative relative energy

Finally, we note that random Al-Mg exhibits two peculiarities. In 25 out of 120 calculations, cross-slip nucleated at two sites, and these two nuclei later coalesced to form the fully-cross-slipped segment. These cases are marked green in Fig. 3.5c). Furthermore, 17 samples have an intermediate minimum that corresponds to a partially cross-slipped state

and has a negative relative energy. Five of those samples also form two nuclei. The deepest minimum has a relative energy of -0.39 eV. These cases are marked blue in Fig. 3.5c). Note that the barrier for spreading of the cross-slipped segment is then higher and more important than the barrier taken from the initial state. However, for consistency with the other results we draw the latter.

3.3 Preliminary Discussion

The most striking feature of the random alloys is the large scatter of ΔE_{act} around the average value. This scatter is caused by fluctuations in the solute concentration, which are excluded *a priori* in the average alloys and in any models that consider only average material properties. As a consequence, ΔE_{act} in real random alloys may be significantly lower than the average value $\Delta E_{\text{act,avg}}$. This is important because cross-slip is a thermally activated process (see Eq. 1.7), so that small decreases in ΔE_{act} lead to exponentially faster cross-slip rates. Along a long dislocation line, regions where the concentration fluctuations give low values of ΔE_{act} will thus dominate the rate of cross-slip nucleation. The fluctuations occur around the average ΔE_{act} , so the average ΔE_{act} sets an initial scale, but the large fluctuations lead to significant lowering of ΔE_{act} in many cases, so that cross-slip nucleation is controlled by concentration fluctuations.

Accordingly, cross-slip in random alloys must be treated as a statistical problem and the effects of solute fluctuations must be accounted for. A simple model for typical values of ΔE_{act} in random alloys will be derived in the following section. Here, we continue with analysis of the simulation data. The activation energy ΔE_{act} and the difference in initial and final energies, ΔE_{end} , are strongly correlated, as shown in Fig. 3.6. If ΔE_{end} is low (more negative), then ΔE_{act} is smaller. Across all concentrations for a given alloy system, the correlation is accurately captured by a linear function,

$$\Delta E_{\text{act}} = \alpha \Delta E_{\text{end}} + \Delta E_{\text{ref}}, \quad (3.1)$$

where ΔE_{ref} is the activation energy at $\Delta E_{\text{end}} = 0$ and $\alpha \approx 0.5$ is a constant. The value of ΔE_{ref} is just slightly lower than the average ΔE_{act} of the corresponding average alloys shown in Fig. 3.5; the variations of the average alloy ΔE_{act} with concentration are small so that aggregating the data across all concentrations is acceptable. A linear correlation between ΔE_{act} and ΔE_{end} is sometimes observed for chemical reactions, where it is referred to as the Bell-Evans-Polanyi [6, 36] (BEP) principle, see also [21]. The BEP principle is usually applied for simple chemical reactions of the type $AB + C \rightarrow AC + B$, and the slope $\alpha = 0.5$ emerges for simple triangular, symmetric transition paths.

Considering the correlation shown in Fig. 3.6, we can express ΔE_{act} in terms of ΔE_{end} by taking $\Delta E_{\text{ref}} = \Delta E_{\text{act,avg}}$ so that

$$\Delta E_{\text{act}} = \Delta E_{\text{act,avg}} + 0.5 \Delta E_{\text{end}}. \quad (3.2)$$

Since the initial and final state energies are controlled by random solute concentration fluctuations, as in solute strengthening of random alloys, particular values are random variables chosen from a normal distribution [72]. The quantity ΔE_{end} is then also a random variable with standard deviation $\sigma [\Delta E_{\text{end}}]$. Assuming that ΔE_{end} follows a normal distribution,

3.3. Preliminary Discussion

we can write the probability distribution of ΔE_{act} as

$$P [\Delta E_{\text{act}}] = \frac{1}{\sqrt{\frac{1}{2}\pi\sigma [\Delta E_{\text{end}}]^2}} \exp\left(-\frac{(\Delta E_{\text{act}} - \Delta E_{\text{act,avg}})^2}{\frac{1}{2}\sigma [\Delta E_{\text{end}}]^2}\right). \quad (3.3)$$

The statistical distribution of ΔE_{act} is thus controlled by the distribution of ΔE_{end} . In the next section, we show that ΔE_{end} can be calculated analytically, thus leading to an analytic description for the statistical distribution of ΔE_{act} .

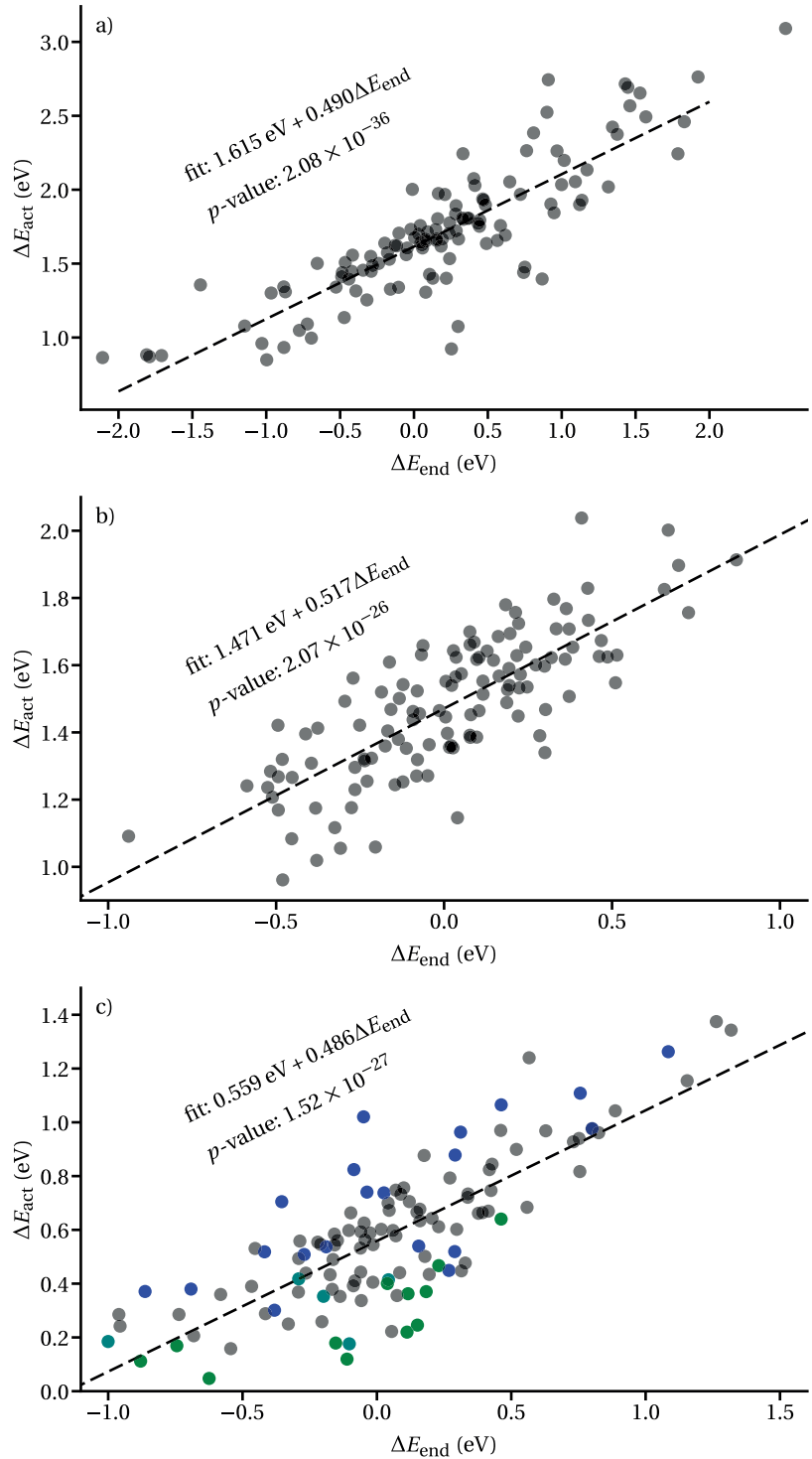


Figure 3.6: Cross-slip activation energy ΔE_{act} vs. end state energy difference ΔE_{end} , showing a linear correlation, for (a) Ni-Al, (b) Cu-Ni, and (c) Al-Mg; in (c) blue markers indicate samples with two nuclei; green markers indicate samples with a partially cross-slipped state with negative relative energy

3.4 Analytic Model for the Statistical Distribution of ΔE_{act}

3.4.1 General model

Due to the correlation between ΔE_{act} and ΔE_{end} , as shown in Fig. 3.6 and discussed in the previous section, the determination of the distribution of ΔE_{act} of the random alloy can be reduced to the problem of determining the distribution of ΔE_{end} . Recall that ΔE_{end} is the difference in total energies between the final and initial states of the cross-slip. We will characterize the distribution of ΔE_{end} in terms of its standard deviation.

The end states differ in energy because, in a given distribution of random solutes, the solute-dislocation and the solute-solute interaction energies are different for the two dislocation configurations (initial and final). Since the correlation shows, $\Delta E_{\text{act}} \approx \Delta E_{\text{act,avg}}$ when $\Delta E_{\text{end}} \approx 0$, we are concerned with determination of the standard deviation of ΔE_{end} in a given alloy system at a given alloy concentration. The analysis proceeds by considering a fixed specific random distribution of solutes, as indicated in Fig. 3.7, computing the energy difference of the initial and final states for this particular random distribution, and then performing an analytical statistical averaging over all possible random distributions to obtain the standard deviation of ΔE_{end} . There are two separate contributions to ΔE_{end} : (i) a contribution from changes in the solute/dislocation interaction energy and (ii) a contribution from changes in solute/solute interaction energy due to the fact that the change in position of the stacking fault alters the *relative* positions of solutes with respect to each other, especially those that are immediately on either side of the initial or final stacking fault plane. These two contributions in energy lead to two independent contributions to the standard deviation of ΔE_{end} , which we denote as $\sigma[\Delta E_{\text{end,s-d}}]$ and $\sigma[\Delta E_{\text{end,s-s}}]$. The total standard deviation for ΔE_{end} is then computed as

$$\sigma[\Delta E_{\text{end}}]^2 = \sigma[\Delta E_{\text{end,s-d}}]^2 + \sigma[\Delta E_{\text{end,s-s}}]^2. \quad (3.4)$$

3.4.2 Solute-Dislocation Contribution

The contribution $\sigma[\Delta E_{\text{end,s-d}}]$ to the standard deviation of ΔE_{end} due to solute-dislocation binding energies can be modeled by adapting the solute strengthening model of Leyson and Curtin [71, 72]. Consider a slice of material parallel to the dislocation line and having a thickness of one period along the line direction, as shown in Fig. 3.7a). We label the atomic sites by their $\{x, y\}$ positions in the plane of the figure as $\{x_i, y_j\}$, with the origin at the center of the dislocation structure, and x the direction along the glide plane. Similarly, let z be the direction along the dislocation line and label the sites by their z position as z_k . Define an equivalent coordinate system with respect to the cross-slipped dislocation, with positions denoted by (x'_i, y'_j, z'_k) . When the dislocation cross-slips, the relative position of the atom at (x_i, y_j, z_k) changes to (x'_i, y'_j, z'_k) . If we denote the solute/dislocation binding energy of a X -solute as $U_{\text{s-d},X}(x_i, y_j, z_k)$, then the change in total solute/dislocation binding energy is the sum over all sites given by [71]

$$\Delta E_{\text{end,s-d},X} = \sum_{ijk} s_{ijk} \left[U_{\text{s-d},X}(x'_i, y'_j, z'_k) - U_{\text{s-d},X}(x_i, y_j, z_k) \right], \quad (3.5)$$

where s_{ijk} is the occupation variable with $s_{ijk} = 1$ if a solute exists at site (i, j, k) and $s_{ijk} = 0$ otherwise.

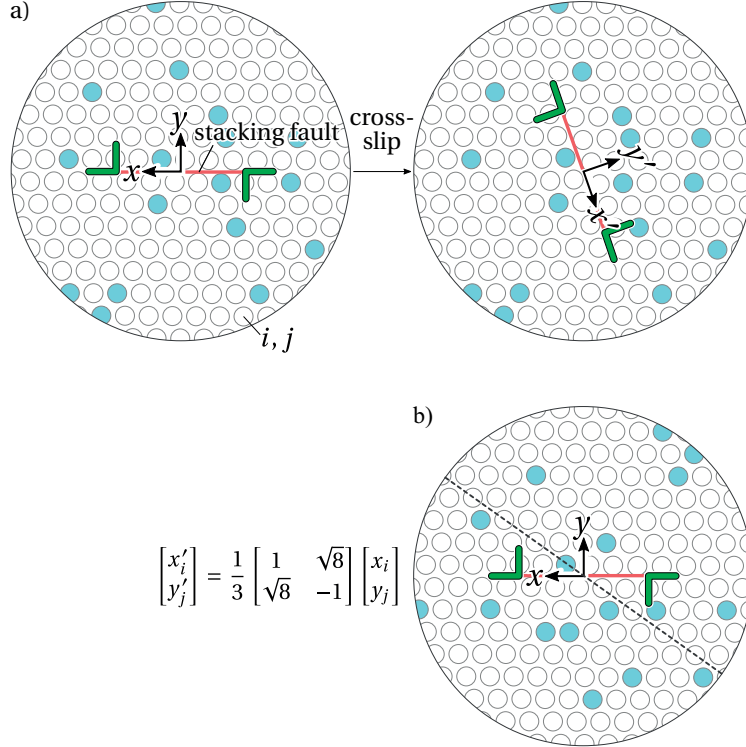


Figure 3.7: a) Reference frames for measuring the relative solute/dislocation positions before and after cross-slip; note that the solute distribution across sites (i, j) does not change. b) The result of cross-slip is the same as a mirroring of the dislocation at $(\bar{1}0\bar{1})$ (dashed line), leading to simplifications in the analysis.

If the solute concentration is high, the corresponding average alloy should be used as matrix material, so that the solute-dislocation binding energies are the binding energies in an average solute environment, and with respect to the dislocation structure in that environment [140].

Eq. 3.5 gives the total energy change for a unit dislocation segment. We are interested in typical fluctuations for a dislocation with finite length ζ_{csn} , which corresponds to $N_b = \zeta_{\text{csn}}/b$ slices along z . For this line length, there are N_b sites with the same in-plane coordinate (x, y) , and solutes occupying any of these sites have the same solute/dislocation interaction energy. The typical energy change resulting from cross-slip of this length of dislocation is the standard deviation given by

$$\sigma [\Delta E_{\text{end,s-d},X}(\zeta_{\text{csn}})] = \sqrt{\langle (\Delta E_{\text{end,s-d},X}(\zeta_{\text{csn}}))^2 \rangle - \langle \Delta E_{\text{end,s-d},X}(\zeta_{\text{csn}}) \rangle^2}, \quad (3.6)$$

where $\langle \cdot \rangle$ denotes an average over all values of the occupation variables. The derivation of $\sigma [\Delta E_{\text{end,s-d},X}(\zeta_{\text{csn}})]$ is analogous to the derivation of the standard deviation of the energy change during regular slip in a random alloy, see [72]. The following assumptions are made (i) the s_{ijk} are uncorrelated Bernoulli random variables, (ii) $U_{\text{s-d},X}(x_i, y_j, z_k)$ depends only on the atom at site (i, j, k) , and, as noted above, (iii) $U_{\text{s-d},X}(x_i, y_j, z_k)$ is only a function of x_i and y_j , i.e.

3.4. Analytic Model for the Statistical Distribution of ΔE_{act}

$U_{\text{s-d},X}(x_i, y_j, z_k) \rightarrow U_{\text{s-d},X}(x_i, y_j)$ due to periodicity along z . We do not repeat the statistical analysis here, which involves standard but extensive manipulations. The final result is

$$\sigma [\Delta E_{\text{end,s-d},X}] = \sqrt{c_X (1 - c_X) \frac{\zeta_{\text{csn}}}{b} \sum_{ij} \left[U_{\text{s-d},X}(x'_i, y'_j) - U_{\text{s-d},X}(x_i, y_j) \right]^2}, \quad (3.7)$$

where c_X is the concentration of X -solutes. The total value of $\sigma [\Delta E_{\text{end,s-d}}]$ for an alloy with N_T components is obtained using the rule for the standard deviation of a sum of normally distributed random variables,

$$\sigma [\Delta E_{\text{end,s-d}}] = \sum_X^{N_T} (\sigma [\Delta E_{\text{end,s-d},X}])^2. \quad (3.8)$$

Finally, note that in the idealized picture of Fig. 3.7a), cross-slip is geometrically equivalent to performing a mirror operation of the random solute distribution across the $(\bar{1}\bar{0}\bar{1})$ plane, as shown schematically in Fig. 3.7c). This operation is described by the affine transformation

$$\begin{bmatrix} x'_i \\ y'_j \end{bmatrix} = \frac{1}{3} \begin{bmatrix} 1 & \sqrt{8} \\ \sqrt{8} & -1 \end{bmatrix} \begin{bmatrix} x_i \\ y_j \end{bmatrix}. \quad (3.9)$$

Due to this symmetry, the only inputs to the theory are the binding energies $U_{\text{s-d},X}(x_i, y_j)$ in the initial state since the binding energy $U_{\text{s-d},X}(x'_i, y'_j)$ at site (i, j) is the binding energy at the symmetry-equivalent site in the undeformed lattice. The number of required calculations can be further reduced by exploiting the fact that the configuration has two-fold rotation symmetry about a line parallel to the z axis through the center. Thus, binding energies need only be calculated for the atoms in the upper half of the xy -plane.

3.4.3 Solute-Solute Contribution

The second contribution to ΔE_{end} comes from changes in direct solute-solute binding energies. For example, solute pairs (first, second, ... neighbors) may be formed or destroyed along the stacking fault ribbon when it is annihilated on the glide plane and/or reformed on the cross-slip plane. Du et al. [25] have shown that this effect is important for cross-slip in Ni-Al, and Rodary et al. [115] have shown that it is important for the related problem of solute strengthening, due to the strong repulsion of Al-Al near-neighbor pairs.

Here, we restrict our attention to first-nearest neighbor pairs. The contribution to ΔE_{end} from formation and annihilation of pairs of X solutes is

$$\Delta E_{\text{end,s-s}} = U_{\text{s-s},XX,1} \Delta N_{\text{s-s}}, \quad (3.10)$$

where $U_{\text{s-s},XX,1}$ is the solute-solute binding energy, and $\Delta N_{\text{s-s}}$ is the dimensionless net change in the number of solute pairs due to cross-slip. The contribution to $\sigma [\Delta E_{\text{end}}]$ can then be estimated as

$$\sigma [\Delta E_{\text{end,s-s},XX}] = U_{\text{s-s},XX,1} \sigma [\Delta N_{\text{s-s}}]. \quad (3.11)$$

Chapter 3. Cross-Slip of Short Dislocations

Like in the case of solute-dislocation binding energies, the total contribution for an alloy with N_T components is obtained using the rule for the standard deviation of a sum of normally distributed random variables,

$$\sigma [\Delta E_{\text{end,s-s}}] = \sum_X^{N_T} (\sigma [\Delta E_{\text{end,s-s,XX}}])^2, \quad (3.12)$$

where we have neglected unlike pairs of atoms.

$\sigma [\Delta N_{\text{s-s}}]$ in Eq. 3.11 can be approximated using a simple model of solute pair formation and annihilation in the stacking fault of a single dislocation. We make the simplifying assumption that the dislocation is straight and the stacking fault is an ideal stacking fault everywhere. In reality, the dislocations may be curved and the atomic displacement close to the partial dislocation cores that delimit the fault is not exactly the displacement corresponding to a perfect fault. Furthermore, we assume that the solute distribution is random and uncorrelated, so that we can replace occupation numbers by the average solute concentration.

Fig. 3.8 shows the two atomic layers in a section of a stacking fault. Atoms in the lower layer are gray. A crystallographic unit cell is shaded red. In a stacking fault ribbon of length ζ along $[10\bar{1}]$, the dislocation line direction, and width d along $[1\bar{2}1]$, there are $\zeta/b \times d/b\sqrt{3}$ such cells. In each cell, there are two atoms in the upper layer. Each atom exchanges one nearest neighbor in the lower plane when the fault is formed or annihilated.

Let $N_\zeta \equiv 2\zeta/b$ and $N_d \equiv d/b\sqrt{3}$. Label the atoms in the upper layer by $i = 1 \dots N_\zeta$ along $x \parallel [10\bar{1}]$ and by $j = 1 \dots N_d$ along $y \parallel [1\bar{2}1]$. The net change in solute-solute pairs when the fault in Fig. 3.8 is formed or destroyed is:

$$\Delta N_{\text{s-s,sf}} = \sum_i^{N_l} \sum_j^{N_d} s_{ij} (s_{ij,2} - s_{ij,1}), \quad (3.13)$$

where s_{ij} , $s_{ij,1}$ and $s_{ij,2}$ are the occupation numbers of the atom at site (i, j) and the two nearest neighbors in the lower plane that are exchanged in the process. s_{ij} is one if there is a solute at site (i, j) , and zero otherwise. The same applies to $s_{ij,1}$ and $s_{ij,2}$. For convenience, let $u_{ij} \equiv (s_{ij,2} - s_{ij,1})$. Note that $\langle u_{pq} \rangle = c_X - c_X = 0 \forall p, q$.

Calculating the standard deviation of $\Delta N_{\text{s-s,sf}}$ requires $\langle \Delta N_{\text{s-s,sf}} \rangle^2$ and $\langle \Delta N_{\text{s-s,sf}}^2 \rangle$. The former is zero, because

$$\begin{aligned} \langle \Delta N_{\text{s-s,sf}} \rangle &= \sum_i^{N_l} \sum_j^{N_d} \langle s_{ij} (s_{ij,2} - s_{ij,1}) \rangle \\ &= \sum_i^{N_l} \sum_j^{N_d} \langle s_{ij} \rangle (\langle s_{ij,2} \rangle - \langle s_{ij,1} \rangle) \\ &= \sum_i^{N_l} \sum_j^{N_d} c_X (c_X - c_X) \\ &= 0. \end{aligned}$$

3.4. Analytic Model for the Statistical Distribution of ΔE_{act}

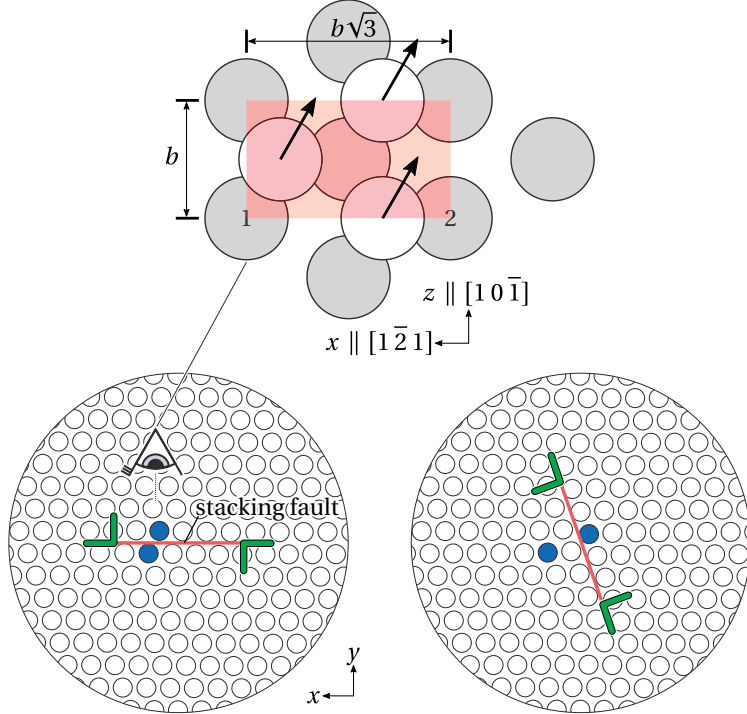


Figure 3.8: Lower images: layer of atoms perpendicular to the dislocation line; a nearest-neighbor pair of solutes (blue) in the stacking fault (red) is destroyed as the dislocation moves from the glide to the cross-slip plane; top: view from top onto the stacking fault; gray atoms are in the lower layer of the fault; per unit cell in the fault (shaded red), there are three atoms in the upper layer of the fault (white), however, two are shared with neighboring cells and thus are counted as one half; during cross-slip, each atom in the upper layer exchanges one nearest neighbor atom in the lower layer

Furthermore,

$$\begin{aligned} \Delta N_{\text{s-s,sf}}^2 &= \left[\sum_i^{N_l} \sum_j^{N_d} s_{ij} u_{ij} \right]^2 \\ &= \sum_i^{N_l} \sum_j^{N_d} (s_{ij} u_{ij})^2 + \sum_i^{N_l} \sum_j^{N_d} \sum_{k \neq j}^{N_d} s_{ij} u_{ij} s_{ik} u_{ik} + \sum_i^{N_l} \sum_{k \neq i}^{N_l} \sum_j^{N_d} s_{ij} u_{ij} s_{kj} u_{kj} \\ &\quad + \sum_i^{N_l} \sum_{k \neq i}^{N_l} \sum_j^{N_d} \sum_{l \neq j}^{N_d} s_{ij} u_{ij} s_{kl} u_{kl}. \end{aligned}$$

Averaging eliminates all but the first term, therefore:

$$\langle \Delta N_{\text{s-s,sf}}^2 \rangle = \sum_i^{N_l} \sum_j^{N_d} \langle s_{ij}^2 \rangle \langle u_{ij}^2 \rangle. \quad (3.14)$$

s_{ij} , $s_{ij,1}$ and $s_{ij,2}$ are Bernoulli random variables, hence:

$$\begin{aligned}\langle u_{ij}^2 \rangle &= \langle s_{ij,2}^2 - 2s_{ij,2}s_{ij,1} + s_{ij,1}^2 \rangle \\ &= \langle s_{ij,2}^2 \rangle - 2\langle s_{ij,2}s_{ij,1} \rangle + \langle s_{ij,1}^2 \rangle \\ &= c_X - 2c_X^2 + c_X \\ &= 2c_X(1 - c_X).\end{aligned}$$

Thus

$$\begin{aligned}\langle \Delta N_{s-s,sf}^2 \rangle &= \sum_i^{N_l} \sum_j^{N_d} 2c_X^2(1 - c_X) \\ &= 2c_X^2(1 - c_X)N_l N_d \\ &= 4c_X^2(1 - c_X) \frac{\zeta d}{b^2 \sqrt{3}}.\end{aligned}$$

Assuming that pair formation and destruction on the glide and cross-slip plane is independent, the variance of the net pair change due to cross-slip is:

$$\text{Var} [\Delta N_{s-s}] = 2 (\langle \Delta N_{s-s,sf}^2 \rangle - \langle \Delta N_{s-s,sf} \rangle^2). \quad (3.15)$$

The standard deviation is therefore:

$$\sigma [\Delta N_{s-s}] = \sqrt{8c^2(1 - c_X) \frac{\zeta d}{b^2 \sqrt{3}}}. \quad (3.16)$$

3.4.4 Results and Comparison to Simulations

In order to verify our model, we compared estimates of $\sigma [\Delta E_{\text{end}}]$ based on Eq. 3.4, Eq. 3.8 and Eq. 3.12 to results from direct atomistic calculations. In the case of Al-Mg and Ni-Al, only Mg and Al solutes, respectively, were taken in the account. However, in the case of Cu-Ni, both Cu and Ni solutes were considered. The average stacking fault width d , which is required for Eq. 3.16, was determined using the Dislocation Extraction Algorithm [136] as implemented in OVITO [135], by taking the average distance between the extracted partial core coordinates in the corresponding average alloy.

Recall that our explicit cross-slip transition state computations were performed on only 20 samples. To obtain accurate estimates for the statistical distribution (standard deviation) of the end state differences ΔE_{end} , we have generated 100 sets of initial and final states for each alloy composition. In these cases, we impose the constraint on off-center displacements (see Sec. 2.3.1) for both initial and final states. In the case of Cu-Ni, the 20 sets of data from the transition path calculations were added, because there the constraint was active in both states, and thus this data was equivalent to the newly generated data.

The predicted and measured values for $\sigma [\Delta E_{\text{end}}]$ are compared in Fig. 3.9, and the two individual contributions from solute-dislocation and solute-solute interactions are also

3.4. Analytic Model for the Statistical Distribution of ΔE_{act}

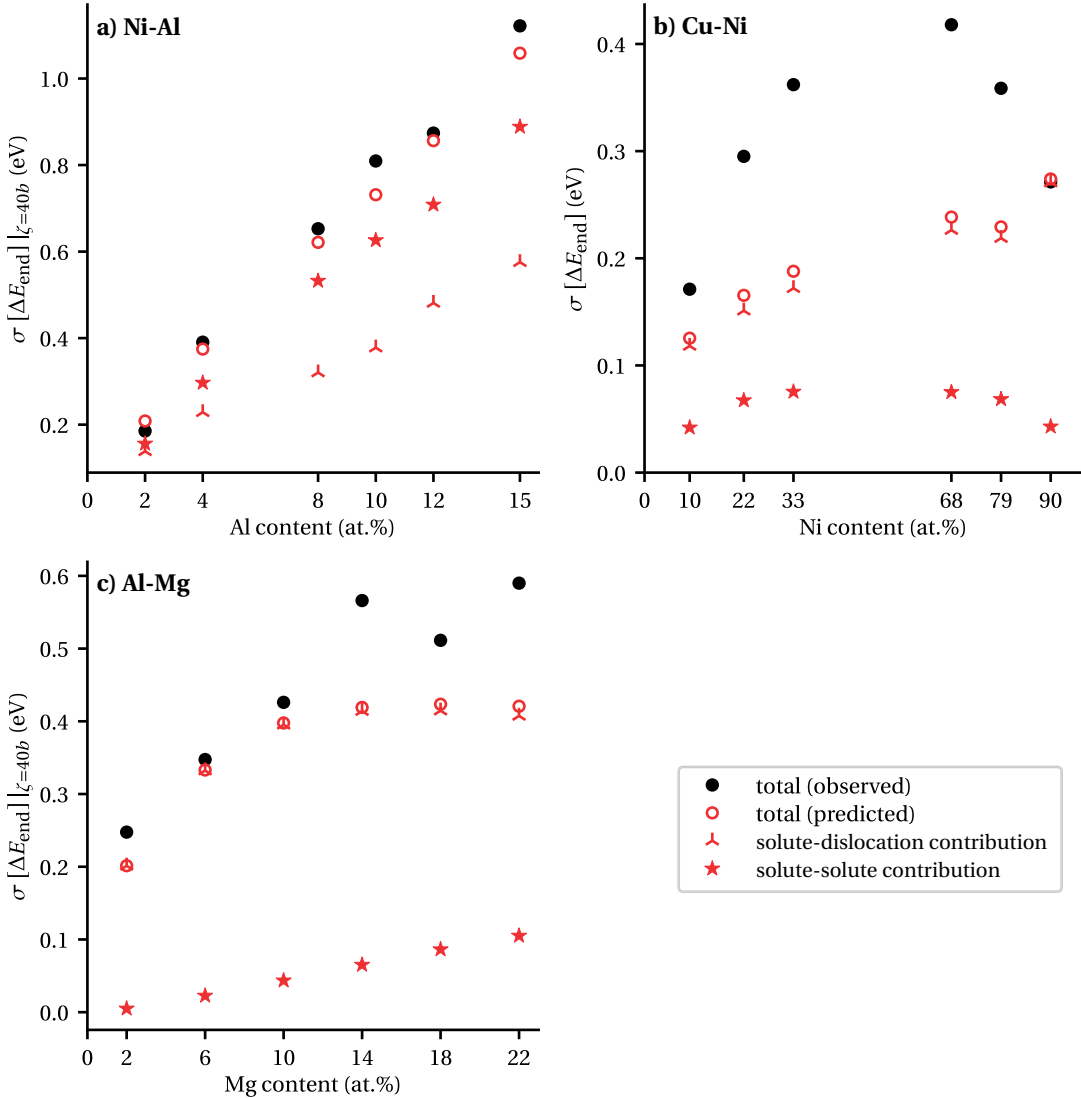


Figure 3.9: Observed (filled symbols) and predicted (open symbols) standard deviation of the end state energy difference ΔE_{end} in (a) Ni-Al, (b) Cu-Ni, and (c) Al-Mg. The individual contributions to the overall standard deviation, due to solute-dislocation (star symbols) and solute-solute interactions (triangle symbols) are also shown.

shown. For Ni-Al, the prediction is satisfactory, with a maximum error of 0.1 eV at 10 at.% Al. For Ni-Al, the solute-solute interaction dominates the distribution. For Al-Mg, the prediction is also satisfactory up to 10 at.% Mg, with the solute/dislocation interaction dominating. At higher concentrations, the predicted standard deviation saturates while the measured value continues to increase. This deviation is due to the increasing importance of non-near-neighbor solute-solute interactions which, though individually small, are very numerous and so contribute non-negligibly to the standard deviation at higher solute concentrations. These interactions can be included in the analysis as a generalization of the near-neighbor pair analysis. An extended model will be presented in Ch. 4. Finally, in Cu-Ni, the prediction is accurate at the lowest Cu and Ni concentrations but then deviates

more significantly at intermediate concentrations. The reason for these deviations is that the solute/dislocation and solute/solute interaction energies in Cu-Ni are generally quite small in magnitude, and hence the neglect of all of the small but much larger number of further-neighbor solute-solute interactions is not accurate; again this can be computed and the agreement with simulations improved, but we do not present the details here.

Summarizing the analysis in this section, we have developed an analytic prediction for the standard deviation of the end-state energy difference ΔE_{end} in terms only of measurable solute/dislocation and solute/solute interaction energies. Explicitly combining the above results for X -solutes, the analysis yields

$$\begin{aligned} \sigma [\Delta E_{\text{end},X}]^2 &= c_X (1 - c_X) \frac{\zeta_{\text{csn}}}{b} \sum_{ij} \left[U_{\text{s-d},X}(x'_i, y'_j) - U_{\text{s-d},X}(x_i, y_j) \right]^2 \\ &\quad + U_{\text{s-s},XX,1}^2 \left(8c_X^2 (1 - c_X) \frac{\zeta_{\text{csn}} d}{b^2 \sqrt{3}} \right). \end{aligned} \quad (3.17)$$

This result, while validated against simulations for the current set of alloys and concentrations, is completely general. It can thus be applied to obtain the statistical distribution of ΔE_{end} relevant for the subsequent computation of cross-slip activation barriers for any other FCC alloys, whether existing or proposed alloys.

3.5 Discussion

We have shown that (i) the cross-slip activation energy ΔE_{act} in random FCC solid solutions is a stochastic variable due to the explicit variations in solute positions relative to the dislocation undergoing cross-slip, with large variations around the average cross-slip barrier; (ii) there is a linear correlation between ΔE_{act} and the difference ΔE_{end} between the initial and final cross-slip states; (iii) the standard deviation of ΔE_{end} can be computed analytically as a function of alloy concentration, solute/dislocation interaction energies, solute-solute interaction energies, for the characteristic cross-slip nucleation length ζ_{csn} ; and therefore (iv) we have an analytic model for the distribution of cross-slip activation energies in random FCC alloys. We now discuss various implications of these results.

First, average material properties are insufficient for predicting the rate of cross-slip in a real alloy. As noted in Sec. 3.3, low values of ΔE_{act} caused by random solute fluctuations will control the rate. In particular, an average parameter like the normalized stacking fault energy $\gamma_{\text{sf}}/\mu b$ is not a useful measure for the ease of cross-slip in random alloys. Another consequence of the strong influence of random fluctuations on the activation barrier is that the probability of cross-slip nucleation in an alloy depends more strongly on the length of the dislocation. Here, we must clearly distinguish between nucleation, i.e. cross-slip of a short (length ζ_{csn}) segment, and lateral growth of this segment. A dislocation line with a length of ζ consists of $N = \zeta/\zeta_{\text{csn}}$ segments of length ζ_{csn} . A long dislocation with large N will sample many different local solute configurations and hence many local cross-slip nucleation environments and is therefore likely to contain segments with cross-slip energy barriers that are much lower than the average value. Among the N segments, the segment with the lowest activation barrier

satisfies, on average,

$$\int_{-\infty}^{\Delta E_{\text{act}}^*} P(\Delta E'_{\text{act}}) d\Delta E'_{\text{act}} = \frac{1}{N}. \quad (3.18)$$

where $P(\Delta E_{\text{act}})$ is the Gaussian distribution of activation energies Eq. 3.3. Thus, ΔE_{act}^* can be obtained from the inverse normal cumulative distribution function. An asymptotic approximation for large N [23] yields

$$\Delta E_{\text{act}}^* \approx \Delta E_{\text{act,avg}} - \frac{\sigma}{2} \sqrt{\log\left(\frac{N^2}{2\pi}\right) - \log\left(\log\left(\frac{N^2}{2\pi}\right)\right)}. \quad (3.19)$$

The weak dependence of the smallest activation energy on the number of segments N allows for reasonable estimates of the barrier over a wide range of lengths. Typical dislocation densities in metals range from well-annealed materials with dislocation density $\rho = 10^{11}-10^{12} \text{ m}^{-2}$ to highly deformed materials with $\rho = 10^{14} \text{ m}^{-2}$. The corresponding dislocation segment lengths are $\zeta \propto 1/\sqrt{\rho}$ and thus vary from 100 nm to 3000 nm. For $\zeta_{\text{csn}} = 40b$ and $\rho \approx 10^{12} \text{ m}^{-2}$, the minimum activation barriers for such segment lengths are $\Delta E_{\text{act}} \approx \Delta E_{\text{act,avg}} - 1.54\sigma [\Delta E_{\text{end}}]$. For a typical Al+2 at.% Mg alloy, this activation energy is only 0.42 eV. For a typical Ni+10 at.% Al alloy (model matrix for Ni-Al superalloys), the operative barrier would be 0.55 eV. For a Cu+33 at.% Ni alloy, the operative barrier would be 1.06 eV. All of these energy barriers are significantly below the average energy barrier of the same alloy, and correspond to very large increases in cross-slip rate at moderate temperatures (for instance, see Eq. 1.7 with $kT = 0.0254 \text{ eV}$ at $T = 300 \text{ K}$).

The barriers for cross-slip *nucleation* can therefore be very low in Ni-Al and Al-Mg. However, a nucleus of length $40b$ must subsequently expand along the dislocation line by lateral motion of the two constrictions in order to grow the cross-slip region. Expansion involves sequentially overcoming smaller energy changes of the order of $\sigma [\Delta E_{\text{end}}(\zeta = 1b)]$ for the lateral advance of the cross-slipped segment by one Burgers vector. These energy changes can be positive or negative, depending on whether the glide or cross-slip plane is energetically favorable at each site. For a long dislocation line, the growing nucleus will eventually encounter regions where there is a long sequence of small positive energy changes, and this sequence can create a significant barrier against further lateral expansion of the cross-slip segment nucleation. On the other hand, if the nucleated segment can expand sufficiently before encountering such a barrier, it can still activate the myriad processes associated with cross-slip. That is, extension of the cross-slip across the entire screw-oriented portion of the line length is not necessary to create cross-slip processes in the alloy. The analysis of characteristic cross-slip segment lengths, and barriers, is a statistical problem that will be addressed in the next chapter. The discussion here serves to identify the problem, and to emphasize that while cross-slip is not driven the average barrier, neither is it driven completely by the single lowest barrier (weak-link behavior).

4 Cross-Slip of Long Dislocations

In the previous chapter, we demonstrated that cross-slip nucleation, which occurs over scales of $\sim 40b$, is strongly influenced by fluctuations in the spatial distribution of solutes over the scale of the critical nucleus. However, full cross-slip of a long ($\sim 10^3b$) dislocations requires that the nucleated segment expand laterally out to longer lengths. One the one hand, it becomes more likely to find easy spots for cross-slip nucleation. On the other hand, unfavorable binding energy fluctuations could accumulate and block cross-slip of the whole dislocation. Another interesting scenario for long dislocations is discussed in App. A.5, where we consider the possibility that partially cross-slipped configurations are equilibrium states.

Thus, cross-slip of long dislocations is more complicated. We are interested in the distribution of activation energies for lengths of $\sim 10^3b$, which are important for understanding real alloys. However, it is not clear whether the BEP principle applies at these lengths so that Eq. 3.2 can be used to predict the distribution of ΔE_{act} . At the same time, it is infeasible to study the behavior at the necessary lengths using atomistic simulations.

In this chapter, we present a new model that does not rely on Eq. 3.2, and that can predict the activation energy distributions for dislocations of arbitrary lengths, at zero and nonzero stress. Cross-slip is seen as a random walk, where each step corresponds to the cross-slip of a $1b$ long segment of the dislocation. In this process, deterministic and random energies are accumulated. The former reflect constriction formation and stress effects, and can be calculated from zero-stress parameters alone. To predict the random energies more accurately, the model presented in Sec. 3.4 is extended to account for solute pairs of first to eight order.

The rest of the chapter is structured as follows. In the first section, we present the extended model of $\sigma [\Delta E_{\text{end}}]$. In Sec. 4.2 we then introduce the random walk model. In Sec. 4.3, we validate the random walk model predictions of the activation barrier by comparisons with fully atomistic results at the short nucleation length of $40b$ for zero stress and non-zero stresses. In Sec. 4.4, we then use the validated random walk model to study long dislocations, which cannot be treated using atomistic calculations, again for zero stress and non-zero stresses. Finally, in Sec. 4.5, we summarize the broad general findings and discuss their implications for cross-slip processes in metal alloys.

4.1 Random Energy Change

In Ch. 3, we derived an analytical, parameter-free model of the standard deviation of ΔE_{end} . However, only first-nearest neighbor pairs of solutes were considered in the solute-solute part. The standard deviation of solute-solute binding energies is then approximately the energy of such a pair times the standard deviation of the change in number of pairs when the stacking fault is destroyed on the glide plane and regenerated on the cross-slip plane. This model is sufficient for Ni-Al and Al-Mg at concentrations up to ca. 15 at.% Al and Mg, respectively. In Cu-Ni alloys with higher concentrations of the secondary atom (up to 33 at.%), the standard deviation was previously underestimated. We now present an extended model, which includes up to eight-nearest neighbor pairs, see Tab. 4.1 for the corresponding distances. In the derivation, we consider pair changes for all atoms in a unit cell below the stacking fault, see Fig. 4.1. Thus, certain correlations between pair cutting processes are taken into account. For example, the uppermost atom is initially a second-nearest neighbor of atoms 1 and 2. After a displacement $a/6[11\bar{2}]$, which creates the fault, the upper atom is a third-nearest neighbor of atom 1 and a first-nearest neighbor of atom 2. Thus, there is a correlation between the neighbor changes of atoms 1 and 2. Moreover, for each atom individually, there is a correlation between second- and first or between second- and third-nearest neighbor pair changes. In addition to higher order pairs and correlations, we also take pairs of unlike atom types into account. The derivation of $\sigma [\Delta E_{\text{end,s-s}}]$ is along the lines of the derivation in Sec. 3.4.3, but much more involved, hence we explain it in App. A.6 and present only the final result here.

Let $U_{\text{s-s},XY,n}$ be the binding energy of a n th order pair of solutes X and Y . Write the pair energies of different order as a vector $\mathbf{U}_{\text{s-s},XY}$, i.e. $\mathbf{U}_{\text{s-s},XY}^{\top} = (U_{\text{s-s},XY,1}, U_{\text{s-s},XY,2}, \dots, U_{\text{s-s},XY,8})$, where the superscript \top indicates transposition. In A.6, it is shown that the contribution to $\sigma [\Delta E_{\text{end,s-s}}]$ from cutting/formation of $X-Y$ pairs can be written using vector-matrix notation,

$$\sigma [\Delta E_{\text{end,s-s},XY}] = \left[\frac{\zeta d}{b^2 \sqrt{3}} \frac{1}{(1 + \delta_{XY})} c_X c_Y \times \mathbf{U}_{\text{s-s},XY}^{\top} [\mathbf{C}_1 + \mathbf{C}_2 (c_X + c_Y) - (\mathbf{C}_1 + 2\mathbf{C}_2) c_X c_Y] \mathbf{U}_{\text{s-s},XY} \right]^{1/2}, \quad (4.1)$$

where c_X and c_Y are the average concentrations of atom types X and Y , respectively; and \mathbf{C}_1 and \mathbf{C}_2 are matrices of constant coefficients, see Eq. A.22. Note that the form above accounts for the fact that pairs XY and YX are equivalent. Thus, the total standard deviation of the solute-dislocation binding energy for an alloy with N_T atom types is the double sum

$$\sigma [\Delta E_{\text{end,s-s}}] = \sum_{\substack{X, \\ Y \geq X}}^{N_T} (\sigma [\Delta E_{\text{end,s-s},XY}])^2. \quad (4.2)$$

The contribution of solute-dislocation binding energies to $\sigma [\Delta E_{\text{end}}]$ is modeled as before using Eq. 3.7 and Eq. 3.8, and $\sigma [\Delta E_{\text{end}}]$ is given by Eq. 3.4.

To verify the model, we compared predictions for $\sigma [\Delta E_{\text{end}}]$ in Ni-Al, Al-Mg and Cu-Ni alloys to results from direct atomistic calculations. All solute-solute pairs, including mixed pairs, and all solute-dislocation interactions were considered in the analytical calculation. The binding energies were calculated as described in Sec. 2.4, using the average-atom approximation for the matrix.

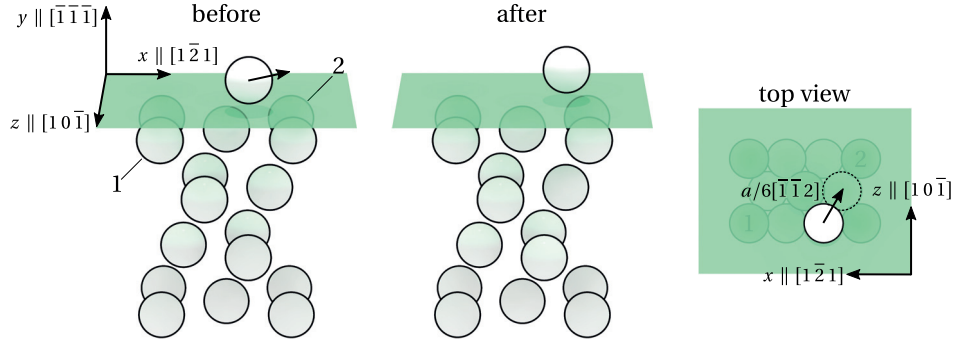


Figure 4.1: Schematic of correlation between pair loss and formation during formation of a stacking fault; left: before before formation of the fault; one unit cell of atoms below the fault and a single atom above the fault are shown; the green plane indicates the center of the fault along z ; the fault is produced by displacing all atoms above the green plane by $a/6[\bar{1}\bar{1}2]$; initially, the atom above the plane is a second-nearest neighbor of atoms 1 and 2; after formation of the fault, it is a third-nearest neighbor of atom 1 and a first-nearest neighbor of atom 2

Table 4.1: Neighbor distances

neighbor order	1	2	3	4	5	6	7	8
distance (a)	$\sqrt{1/2}$	1	$\sqrt{3/2}$	$\sqrt{2}$	$\sqrt{5/2}$	$\sqrt{3}$	$\sqrt{7/2}$	2

The predictions are compared to the results of the atomistic calculations described in Ch. 3. Recall that the dislocation length ζ was $40b$, and the number of realizations was 100 (Ni-Al and Al-Mg alloys) or 120 (Cu-Ni alloys). In addition, new atomistic transition path calculations were carried out during development of the random walk model. In these calculations, the inner radius of the cylinder was increased from $10\sqrt{3}a$ to $13\sqrt{3}a$, in order to be consistent with simulations of cross-slip under stress, where a larger radius is required to avoid image effects due to increased splitting of the dislocation. The calculations with applied stress are explained further below. In addition, the criterion limiting slip of the dislocation away from the center, see Sec. 2.3.1, was applied both to the initial and final state in these calculations. The number of realizations was 100 for each concentration.

Predicted and observed values are compared in Fig. 4.2. Black bars show the atomistic data from Ch. 3. Gray bars show the new atomistic data. In Ni-Al alloys (Fig. 4.2a)) first nearest neighbor pairs dominate; including higher order pairs has little effect. However, such pairs are important in Al-Mg (Fig. 4.2b)) at higher concentrations and in the Cu-Ni alloys (Fig. 4.2c)). In the latter case, the higher order pair model correctly predicts the peak at ca. 68 at.% Ni, which is not seen if only first-nearest neighbor pairs are taken into account. Note that predictions including up to fifth nearest neighbors are shown in Fig. 4.2. Contributions from sixth to eighth order pairs are typically less than 0.01 eV. The maximum absolute difference between a prediction with first to fifth neighbor pairs and the corresponding atomistic result is -0.084 eV, in Al+14 at.% Mg.

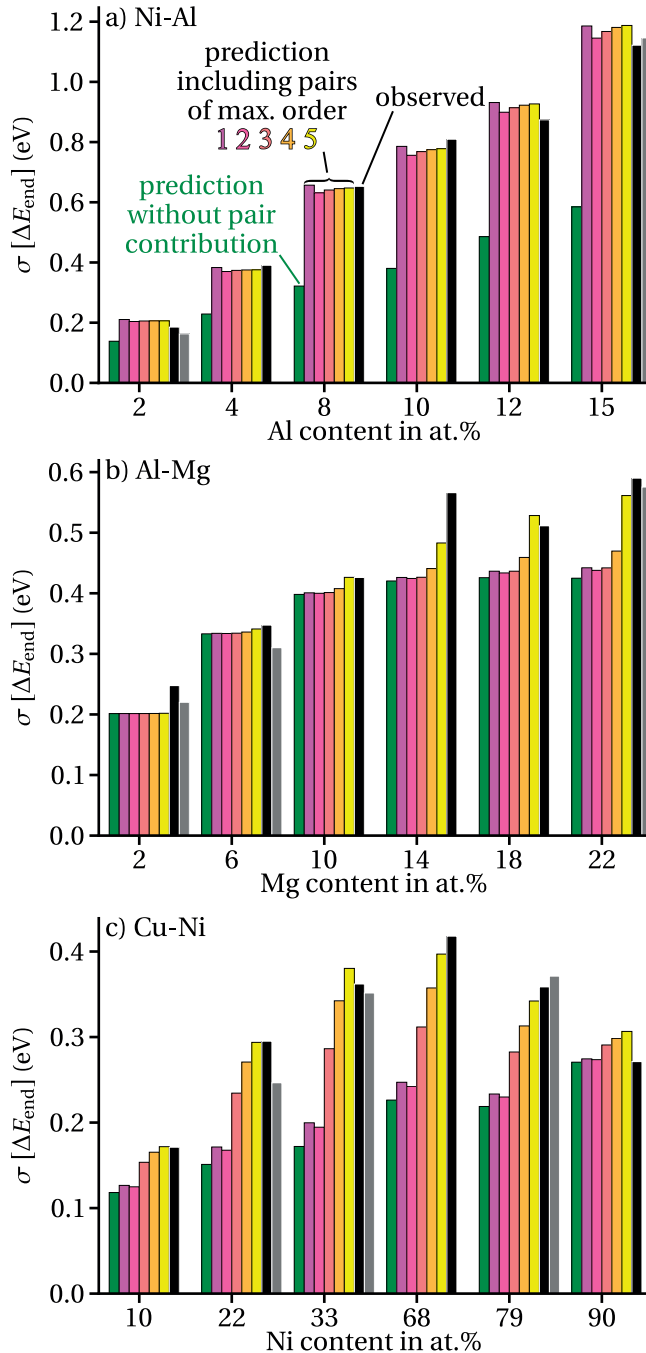


Figure 4.2: Standard deviation of ΔE_{end} for a 40b long dislocation. Colored bars: predictions made with Eq. 3.4 and the extended solute pair model; the different colors indicate the maximum order of neighbor pairs included in the calculation. Black bars: observations from atomistic calculations reported in Ch. 3; the number of realizations 100 in Ni-Al and Al-Mg, and 120 in Cu-Ni. Gray bars: observations from additional atomistic calculations discussed in this chapter (100 realizations); ΔE_{end} also includes solute-dislocation binding energies.

4.2 Random Walk Model

ΔE_{end} depends on the length of the cross-slipped segment. As the segment grows, more and more solute binding energy differences are accumulated. The energy barrier for cross-slip is then the sum of these energies, which is a statistically distributed variable, plus a deterministic energy corresponding to constriction formation. The accumulation of energies can be simulated using a random walk model, where cross-slip of a subsegment is a step and the associated random change in energy is the step length.

Consider a screw dislocation with a length of N_b times the Burgers vector magnitude b . Partition the dislocation into N_b unit segments of length $1b$. We view cross-slip as the discrete process of moving the dislocation unit segment by unit segment from the glide to the cross-slip plane, as shown schematically in Fig. 4.3b). Each unit segment is either fully dissociated on the glide plane or fully dissociated on the cross-slip plane, and the current cross-slip segment consists of a contiguous set of N_{flip} flipped unit segments each of length b . We ignore the shape of the constrictions joining segments on the glide and cross-slip planes. The constriction energy must be determined with some other method and merely enters as input parameter, as we shall see. Cross-slip can nucleate in any of the N_b unit segments. However, we assume that there can be only one nucleus. On each step after the first, this nucleus grows by attaching the left or right neighboring segment on the glide plane. Associated with each step is a random change in binding energies, which is obtained from the model in Sec. 4.1. Before simulation of the cross-slip process, a random energy change is drawn for each unit segment from a normal distribution with standard deviation σ [ΔE_{end}] (Eq. 3.4) and mean zero. Note that $\zeta = 1b$ in Eq. 3.7 and Eq. 4.1, since the segments are one Burgers vector long. During the initial growth of the cross-slip nucleus ($N_{\text{flip}} < N_c$ where $N_c b$ is the total length of the two constrictions), the energy cost to form a constriction must also be introduced, as described below.

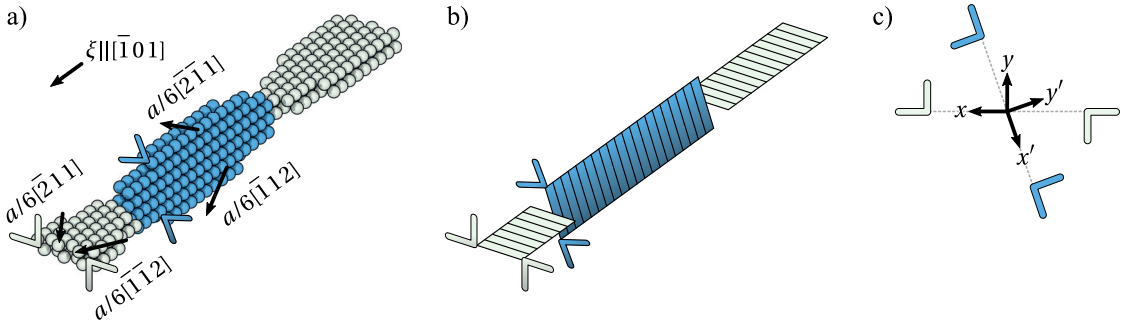


Figure 4.3: a) Cross-slip transition state in a Ni-15at.% Al average alloy, from an atomistic transition path calculations reported in Ch. 3; only atoms that don't have regular FCC coordination are shown; gray: segment on the glide plane; blue: cross-slip plane; atoms visualized using Ovito [135]. b) Simplified picture of the process, as used in the random walk model; the dislocation is partitioned into N_b segments of $1b$ length; cross-slip is the discrete process of moving the segments one by one from the glide to the cross-slip plane. c) A coordinate system showing a 3D space with axes x , y , and z , and a rotated coordinate system x' , y' , z' .

On each step, the unit segment (left or right) chosen for the next flip is the unit segment with the lower energy change, see Fig. 4.4. For a given starting point, the total accumulated energy (constriction contributions plus random contributions) after N_{flip} flips is computed as a function of the total length $N_{\text{flip}} b$ of the cross-slipped segment. The process is continued until

$N_{\text{flip}} = N_b$, i.e. until the entire dislocation has cross-slipped. The activation barrier for the entire cross-slip is the maximum energy encountered over the entire process. The activation barrier for the given segment is then the minimum of the activation barriers over all N_b possible starting points for cross-slip nucleation. In the presence of Escaig stresses or Schmid stresses, additional deterministic energies are added to account for these effects, as described below.

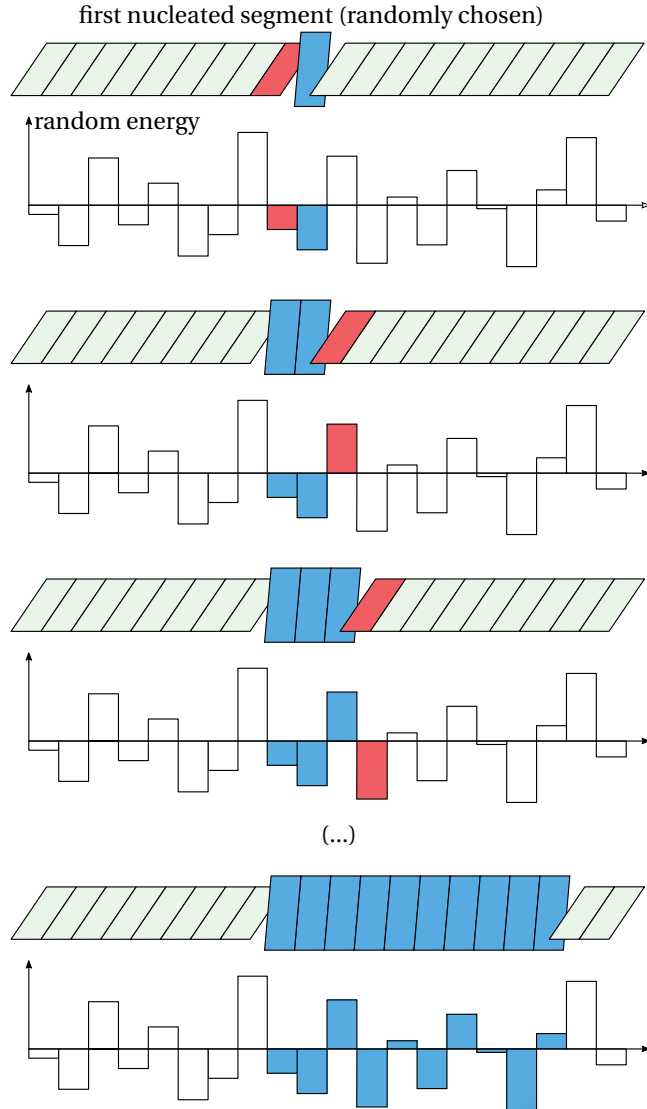


Figure 4.4: Step selection in the random walk; cross-slip can nucleate in any of the $1b$ segments; subsequently, however, low-energy steps are preferred

4.2.1 Deterministic Energy Change

In addition to the random change of solute-dislocation binding energies, there is a deterministic energy change due to constriction formation. In pure metals at zero stress,

the activation energy of F-E-cross-slip is approximately the formation energy of two point constrictions, i.e. $\Delta E_{\text{act,avg}} \approx 2E_c$ [99]. This total energy is distributed over a physical length $N_c b$; that is, the full two-point-constriction energy builds gradually over some physical length, as seen in directly atomistic models of the transition path. To capture the energetics of the constriction formation, we proceed as follows.

The first unit segment on the cross-slip plane cannot nucleate without the formation of a full constriction on the glide plane. Thus, there is an additional energy cost for the first flip of $E_c = \Delta E_{\text{act,avg}}/2$. The two half-constrictions on the cross-slip plane then grow as the cross-slipped segment becomes longer. At a length $N_c b$, the half-constrictions are well-separated and the total energy cost of forming the constrictions has been accumulated. To model this, we assume that the additional constriction energy per flip decreases linearly as the segment length grows from b to $N_c b$. The total energy thus increases quadratically. At flip i of the nucleation process, the total deterministic energy is thus given as

$$E_{\text{det}}(i) = \begin{cases} \left(\frac{1}{2} + \frac{i(1-i+2N_c)}{2N_c(N_c+1)} \right) \Delta E_{\text{act,avg}} & i \in [1, N_c] \\ \Delta E_{\text{act,avg}} & i \in (N_c, N_b - N_c + 1) \end{cases}. \quad (4.3)$$

For simulations, we use periodic boundary conditions to eliminate end effects. Thus, when the cross-slip process is nearly complete, the constrictions should annihilate, and the energy regained. Thus, the deterministic energy is modified as follows for i in the range $[N_b - N_c + 1, N_b]$:

$$E_{\text{det}}(i) = \Delta E_{\text{act,avg}} \left(1 - \frac{(i - N_b + N_c)(1 + i - N_b + N_c)}{2N_c(N_c+1)} \right), \quad (4.4)$$

and $E_{\text{det}}(N_b) = 0$. Fig. 4.5 shows the energy vs. cross-slipped length from an atomistic transition path calculation for Ni+15 at.% Al as compared to the deterministic energy of Eq. 4.3 using the atomistic activation energy and $N_c = 10$. The length of the cross-slipped segment in the atomistic calculation was measured using the dislocation analysis (DXA) algorithm implemented in Ovito [135]. Atomistically, the constriction forms at zero length, but this energy must be assigned to the first unit segment of length b . The use of $\Delta E_{\text{act,avg}}/2$ for the first flip underestimates the atomistic energy by approximately 0.19 eV on the first step. Larger errors are seen in the region of constriction annihilation. This may explain later results in which there are small (< 0.1 eV) differences between the median values of activation energy distributions from atomistic and random walk calculations, but the model of annihilation is only of importance for comparing to the simulation results at short total lengths ($N_b = 40$). Overall, the model for constriction formation and annihilation is in good qualitative agreement with the atomistic simulation, and is fully satisfactory for the purposes of this work.

4.2.2 Stress Effects in the Random Walk Model

Escaig stresses that lower the energy of the final state relative to the initial state will facilitate cross-slip. Net Schmid stresses acting on the cross-slip plane will also facilitate cross-slip. Both types of stresses will also help to overcome very high activation barriers that can arise in the

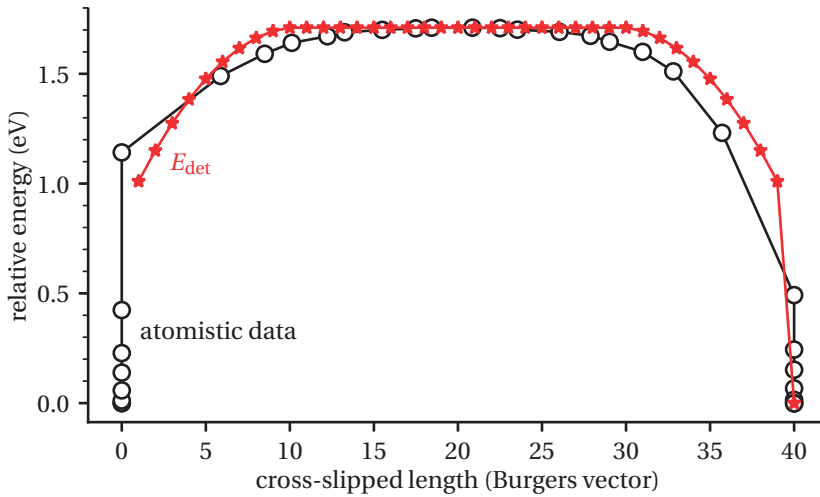


Figure 4.5: Energy as a function of the length of the cross-slipped segment from an atomistic transition path calculation with average Ni+15 at.% Al and the corresponding approximate profile E_{det} used in random walk calculations; the first few points at zero length in the atomistic profile correspond to formation of the constriction on the glide plane.

random walk under zero stress. The work done by such external stresses is deterministic and hence can be included in the random walk model by modifying the deterministic energy contribution in Eq. 4.3.

We first address Escaig stresses, which couple to the edge components of the partial dislocations of the dissociated screw dislocation in FCC materials. These stresses change the width of the partial separation. Let $\tau_{\text{glide}}^{\text{Esc}}$ and $\tau_{\text{cross}}^{\text{Esc}}$ be the Escaig stresses on the glide and cross-slip plane, respectively. These stresses have two effects. First, they do work on the system when the splitting width changes from its equilibrium value on the glide plane to its equilibrium value on the cross-slip plane. These deterministic energies can be computed in atomistic simulations, but models using anisotropic elasticity are more general. When comparing with atomistic simulations, the atomistic result for $E_{\text{det}}^{\text{Esc}}$ was used. In other cases, an anisotropic-elastic estimate¹ was used,

$$E_{\text{det}}^{\text{Esc}} = -\frac{b^3}{8\pi} \left(K_s - \frac{K_e}{3} \right) \log \left(\frac{\gamma_{\text{eff},g}}{\gamma_{\text{eff},c}} \right), \quad (4.5)$$

where K_e and K_s are the energy prefactors of the edge and screw dislocation, respectively, see Eq. 1.3; and $\gamma_{\text{eff},g}$ and $\gamma_{\text{eff},c}$ are the effective stacking fault energies on the glide and cross-slip plane,

$$\gamma_{\text{eff},g} = \left(\gamma_{\text{SF}} + \frac{b\tau_{\text{glide}}^{\text{Esc}}}{2\sqrt{3}} \right), \quad \gamma_{\text{eff},c} = \left(\gamma_{\text{SF}} - \frac{b\tau_{\text{cross}}^{\text{Esc}}}{2\sqrt{3}} \right). \quad (4.6)$$

Second, the Escaig stresses change the constriction energy. According to Püschl and Schöck [99, 100] $E_c \propto \log(2d/b) d/b$, thus we scale the energy of the constriction on the glide plane by

¹ Equ. 5.7 in Ref. [14] with $d_M = d$ and splitting widths from anisotropic elasticity [1, Equ. 13.149b]

the ratio $(\log(2d^*/b)/\log(2d/b))(d^*/d)$, where d^* is the stressed equilibrium dissociation width. Using the anisotropic-elastic solution for d^* , Eq. 1.2, this ratio can be written as

$$f_c = \frac{\gamma_{SF}}{\gamma_{eff,g}} \frac{\log((K_s - K_e/3)b/(4\pi\gamma_{eff,g}))}{\log((K_s - K_e/3)b/(4\pi\gamma_{SF}))}. \quad (4.7)$$

Taking into account the effect of τ_{cross}^{Esc} on the constriction on the cross-slip plane is more complicated, because the stress also changes the constriction size, and hence N_c . Thus, we neglect this energy contribution. Nevertheless, we obtain a good agreement between predicted activation energies and atomistic data, see App. A.7.

Out of the two Schmid stress components, only the one on the cross-slip plane needs to be considered. A Schmid stress on the glide plane simply causes the dislocation to slip away. The segment on the cross-slip plane, however, is pinned by the two constrictions and is therefore expected to bow out. The work done by bowing out can then also drive lateral expansion of the cross-slipped segment. We assume that the bow-out takes the shape of a circular arc with radius R , arc-length s and swept area A . Within isotropic linear elasticity, the total energy of bowing out can be described analytically [156]. For a size ib of cross-slipped segment, the total energy due to bow-out is

$$E_{det}^{Sch}(i) = Ts(i) - \tau_{cross}^{Sch}bA(i),$$

where

$$\begin{aligned} s(i) &= \left[2R \sin^{-1} \left(\frac{ib}{2R} \right) - ib \right], \\ A(i) &= R^2 \sin^{-1} \left(\frac{ib}{2R} \right) \sqrt{1 - \left(\frac{ib}{2R} \right)^2}, \\ R &= \frac{T}{\tau_{cross}^{Sch}b} \end{aligned} \quad (4.8)$$

and T is an effective dislocation line tension representing the cost of creating additional dislocation line length.

The value of T is guided by the work of Kang et al. [60], who compared the stress dependence of the cross-slip activation energy in the Friedel-Escaig model and in atomistic simulations. Comparing the shape of the cross-slipped segment in the two models, the authors suggested $T = \alpha \mu b^2/2$, where α is a parameter in the range [0.1, 0.6], and μ is an effective isotropic shear modulus. Following the authors and Scattergood and Bacon [119], we use

$$\mu \equiv K_s = \sqrt{\frac{(C_{11} - C_{12})C_{44}}{2}}. \quad (4.9)$$

Kang et al. used a value of 0.45 for α . However, the FE-model overestimated the activation energy. Even after applying a constant shift of -0.7 eV, the energy was slightly too high at high ($\propto 10^2$ MPa) Schmid stresses. Thus, we use a smaller line tension of $1/2 \times 0.45\mu(b/\sqrt{3})^2/2 = 0.075\mu b^2/2$, which is slightly below the lower bound suggested by Kang et al. The activation energies predicted using this line tension in Eq. 4.8 are closer to their atomistic results than the corresponding predictions of the FE-model, see Fig. A.14. Additional

random energy fluctuations during slip from the straight to the bowed-out configuration due to solute-dislocation interactions (essentially solute strengthening) are neglected.

In total, in the presence of Escaig and/or cross-slip Schmid stress, the deterministic energy profile for the random walk model is

$$E_{\text{det}}(i) = \begin{cases} \left(\frac{f_c}{2} + \frac{i(1-i+2N_c)}{2N_c(N_c+1)} \right) \Delta E_{\text{act,avg}} + iE_{\text{det}}^{\text{Esc}} + E_{\text{det}}^{\text{Sch}}(i) & i \in [1, N_c] \\ \left(\frac{f_c+1}{2} \right) \Delta E_{\text{act,avg}} + iE_{\text{det}}^{\text{Esc}} + E_{\text{det}}^{\text{Sch}}(i) & i > N_c \end{cases}. \quad (4.10)$$

Under periodic boundary conditions for comparison to atomistic simulations, the constriction is annihilated in the manner used at zero stress; this is only relevant for pure Escaig stresses.

4.3 Validation Against Atomistic Simulations

Here, we compare predictions of the random walk model against full atomistic transition state simulations at $N_b = 40$ using periodic boundary conditions, for both zero stress and applied Escaig stresses. The results demonstrate that the random walk model captures all major features of the simulations with very good quantitative accuracy, justifying its application to long dislocation lines ($N_b \gg 40$) in the next section.

Note that the atomistic calculations were carried out with slightly larger configurations (inner radius $13\sqrt{3}a$ instead of $10\sqrt{3}a$), in order to minimize boundary effects when an Escaig stress is applied on the cross-slip plane, see App. A.4. $\Delta E_{\text{act,avg}}$ was recalculated with the slightly larger geometry as well, although the differences are negligible (< 0.03 eV). $\Delta E_{\text{act,avg}}$ and the standard deviation of the random energy per step are listed in Tab. 4.2.

Table 4.2: Average-alloy cross-slip activation energy $\Delta E_{\text{act,avg}}$ and standard deviation of the random energy per $1b$ step, as calculated with Eq. 3.4

alloy	$\Delta E_{\text{act,avg}}$ (eV)	$\sigma [\Delta E_{\text{end}}] _{\xi=1b}$ (eV)
Ni+02%Al	1.73	0.033
Ni+15%Al	1.89	0.189
Al+02%Mg	0.73	0.032
Al+06%Mg	0.69	0.054
Al+22%Mg	0.63	0.088
Cu+22%Ni	1.65	0.047
Cu+33%Ni	1.64	0.062
Cu+79%Ni	1.51	0.054

4.3.1 Zero Stress

At zero Escaig stresses, a total of 100 realizations were used to generate the atomistic results and a total of 10000 realizations were used in the (much faster) random walk calculations. Fig.

4.3. Validation Against Atomistic Simulations

Figure 4.6 shows a box plot of the activation energy distributions at zero stress for a number of alloys. The line in each box indicates the median, while the lower and upper edges show the first and third quartile, respectively.

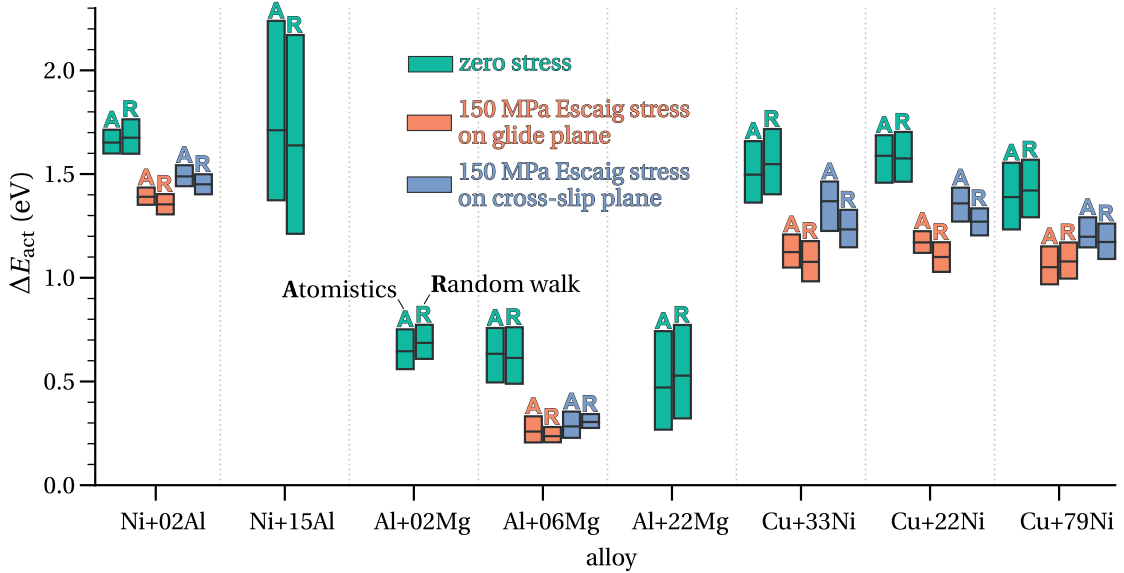


Figure 4.6: Distributions of cross-slip activation energies in solid solution alloys for $N_b = 40$ with periodic boundary conditions, from atomistic (A) and random walk (R) simulations; the upper and lower edge of each box represent the third and second quartile of the data, i.e. 50% of all values lie in this range; the horizontal line indicates the median. The number of realizations in atomistic calculations was 100, except in the case of Cu+22 at.% Ni and Cu+79 at.% Ni at finite stress where only 50 realizations were used; 10000 random walk realizations are used in all cases.

Atomistic and random walk results are typically similarly distributed. The difference in median values is always less than 0.07 eV (in Ni+15 at.% Al) and the largest relative difference is 12% (in Al+22 at.% Mg). The largest relative difference in variance is 78% (in Ni+02 at.% Al) but the actual difference is very small (0.007 eV higher than the atomistic value). The similitude of the distributions is assessed by the two-sided Kolmogorov-Smirnov (K-S) [64, 130] statistic. The Null hypothesis that the samples are drawn from the same continuous distribution can only be rejected at significance level 0.05 in the case of Al+02 at.% Mg and Ni+02 at.% Mg. If the random walk samples are shifted to eliminate the difference in median values, the Null hypothesis cannot be rejected in any case. Thus, the random walk model typically yields distributions very similar to those obtained from the atomistic calculations.

Small differences in median values are likely caused by deviations of E_{det} from the true deterministic energy profile. For example, in the case of Ni+02 at.% Al, E_{det} overestimates the true energy at the end of constriction formation and during annihilation, see Fig. 4.5. However, the maximum of the random walk frequently occurs in these regions, see Fig. 4.7. Thus, the random walk tends to yield slightly higher energies, see Fig. 4.6. For completeness, we note that in the case of Ni+15 at.% Al, where $\sigma[\Delta E_{\text{end}}]$ is higher, the maximum frequently occurs on the first and last few steps, see Fig. 4.7.

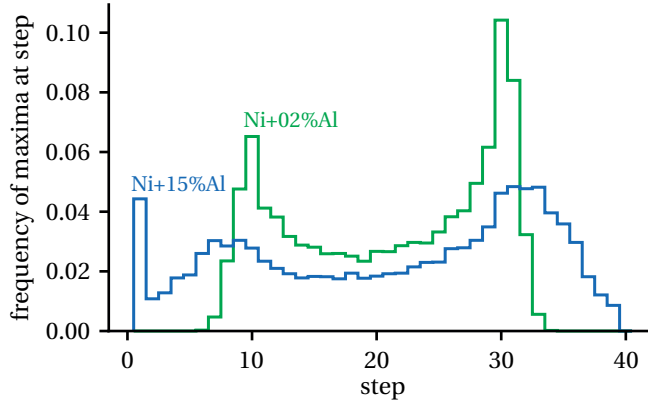


Figure 4.7: Frequency of the location of the maximum as a function of step

Furthermore, the random walk model *predicts* the correlation between the activation energy ΔE_{act} and the end-state difference ΔE_{end} that was empirically found in the atomistic simulations at length $40b$. For example, Fig. 4.8 shows ΔE_{act} versus ΔE_{end} from the atomistic and random walk calculations for Ni+15 at.% Al. Linear regression of both data sets yields slopes of 0.5 and 0.54, respectively. Slopes of 0.53–0.54 are obtained from the random walk calculations in other materials, see Fig. A.15 in App. A.8. Therefore, the random walk model, with only the average barrier height and solute-solute and solute-dislocation interaction energies as inputs, reproduces a major empirical feature of the atomistic simulations.

In fact, the correlation is not much different from the correlation between the maximum and location of a regular normal random walk, where there is no preference for small steps, and no preference for paths with low maximum. A joint plot for such a walk is shown in Fig. 4.8b). A linear fit to the data yields a slope of 0.51. However, the trends are different in the region of positive and negative ΔE_{end} . In the region of positive ΔE_{end} , ΔE_{act} is bounded from below by ΔE_{end} , since, by construction, the maximum cannot be less than the final location of the walk. In the region of negative ΔE_{end} , the slope decreases, an effect which can also be seen in the random walk data of Fig. 4.8a). This difference between the regions of positive and negative ΔE_{end} becomes very clear when the number of steps is increased. Fig. 4.8c) shows random walk energies for $N_b = 1000$. In this case, using $\Delta E_{\text{act}} \approx \Delta E_{\text{act,avg}} + 0.5\Delta E_{\text{end}}$ to predict typical values of ΔE_{act} would be very inadequate.

4.3.2 Non-zero Escaig Stresses

Using the same atomistic methods as in our previous work, transition state calculations were carried out for Escaig stresses of $\tau_{\text{glide}}^{\text{Esc}} = 150 \text{ MPa}$ and $\tau_{\text{cross}}^{\text{Esc}} = 150 \text{ MPa}$ for several alloys. For Cu+22 at.% Ni and Cu+79 at.% Ni, only 50 realizations were simulated. In applying the random walk model, the value of $E_{\text{det}}^{\text{Esc}}$ was taken from the average of the end-state difference obtained in the atomistic simulations. The results are shown in Fig. 4.6. The difference in median values is typically small, with a maximum relative difference of 10% (0.14 eV) in Cu+33 at.% Ni with stress on the cross-slip plane. The widths of the distributions are typically similar. However, in Al+06 at.% Mg there is a comparatively large relative difference in the variances, –68% and –78% for stresses on the glide and cross-slip plane, respectively, but only small

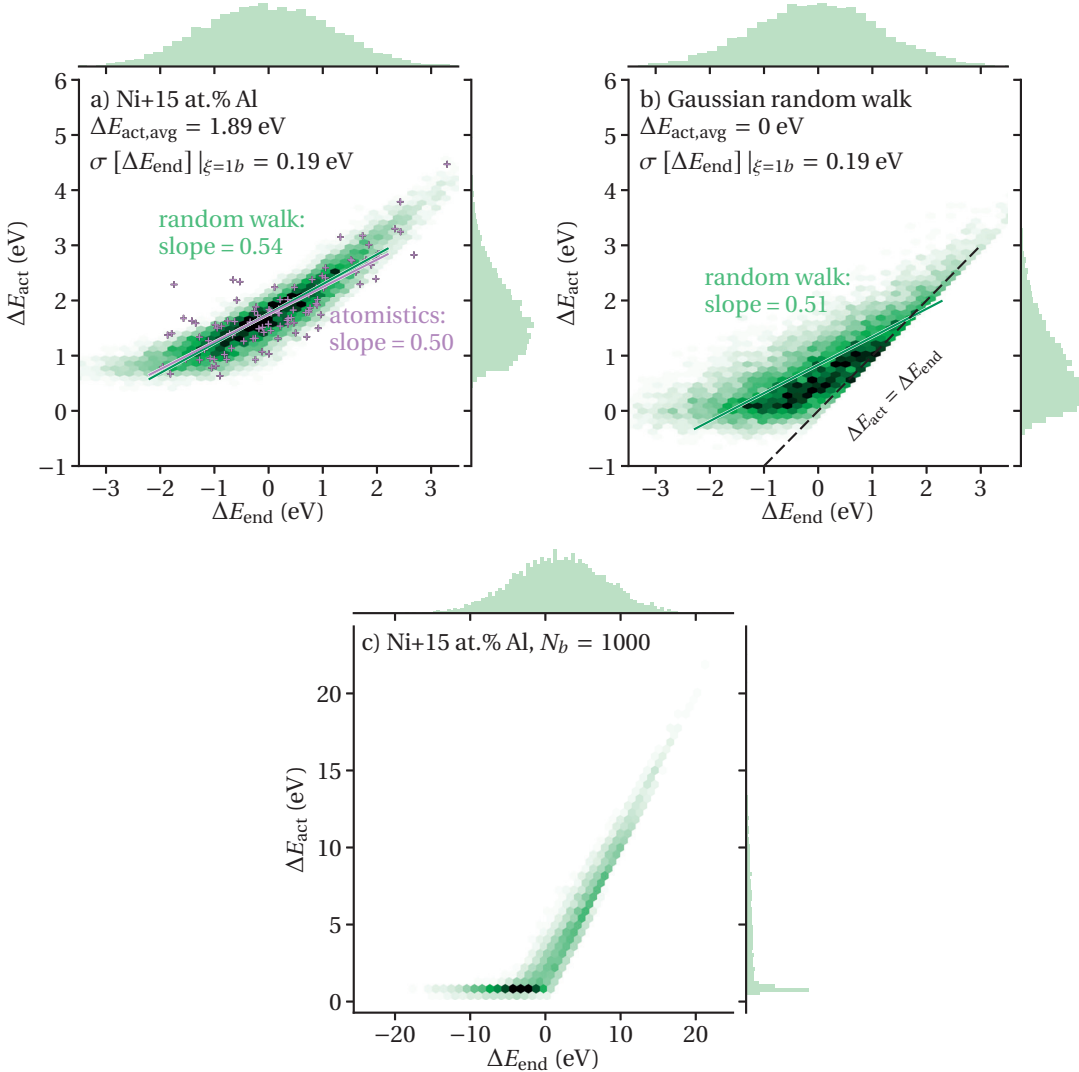


Figure 4.8: Joint plots of the distributions of activation energies ΔE_{act} and end state energy differences ΔE_{end} ; a) comparison of random walk and atomistic data for Ni+15 at.% Al and $N_b = 40$; hexagonal bins: random walk data, color indicates frequency, see marginal distributions; "+": atomistic data; lines: linear regression; b) distribution for an ideal random walk without drift, i.e. $E_{\text{det}} = 0$, and no selection of low-energy steps or low-energy paths; c) random walk data (our model) for Ni+15 at.% Al and $N_b = 1000$ (no periodic boundary conditions)

absolute differences (-0.008 eV and -0.012 eV). The K-S statistical analysis shows that the Null hypothesis that the samples are drawn from the same continuous distribution can be rejected at significance 0.05 for all alloys and stresses except in the case of Cu+79 at.% Ni. However, if the difference in median values is subtracted, then the hypothesis can only be rejected in the case of Al+06 at.% Mg. Thus, most of the error comes from the difference in median values, which is likely a consequence of errors in the deterministic energy profile, as discussed in Sec. 4.3.

4.4 Cross-Slip of Long Dislocations

Useful cross-slip in real materials requires the cross slip of segments much longer than $40b$, although $40b$ is the critical nucleation size in elemental metals. Having validated the random walk model at atomistically-accessible sizes, we can now apply it to much larger lengths relevant to real materials. Simulations were performed at lengths $N_b = 40, 100, 200, 500, 1000$ with no periodic boundary conditions, so the constrictions were not annihilated at the end of the process, and results effectively corresponding to cross-slip of a slightly longer segment or a segment pinned by obstacles.

4.4.1 Zero Stress

For zero applied stresses, Fig. 4.9 shows distributions of ΔE_{act} for lengths between $40b$ and $1000b$. A clear trend is seen: with increasing length, the frequency of high activation energies increases. For the third quartile, we observe a trend $\Delta E_{\text{act,avg}} + \sigma [\Delta E_{\text{end}}] x \sqrt{N_b}/2$ with $x = 1.2$. The scaling of higher percentile levels follows the same form, but with larger x . On the other hand, the lower tail of the distribution does not change significantly. The decrease of the first quartile is much less pronounced than the increase of the third quartile. Accordingly, the median values increase by several tenths of an electron volt, in the case of Ni+15 at.% Al even by more than one electron volt. The minimum barrier, however, barely changes. The increasing frequency of high activation energies means that cross-slip of long dislocations is much harder and less frequent in solid solutions. However, this result pertains only to zero stress. As shown in the next section, the high barriers are easily overcome by fairly modest applied stresses, leading to much lower activation energies.

Histograms of the energy distributions of Cu+33 at.% Ni, for $N_b = 40, 200, 1000$ clearly show the tail of high ΔE_{act} that develops with increasing length, see Fig. 4.10. The inset plot shows for each step in the $N_b = 200$ calculation the frequency with which the maximum occurred on this step, and the median energy of the corresponding maxima. The distribution of the maxima between the peaks is reminiscent of the arcsine distribution expected for Wiener processes [70]. The low energy paths are those where the maximum occurs early on. Conversely, high energy paths are those where the maximum occurs near the end. Accordingly, these paths are particularly sensitive to the work done by an external stress in extending or bowing out the dislocation on the cross-slip plane.

4.4.2 Non-zero Stress

Schmid and Escaig stresses in the range 1–200 MPa were applied to dislocations with length $N_b = 500$. The constrictions were not annihilated at the end of the process and no periodic boundary conditions were used. In contrast to the calculations with short segments in Sec. 4.3.2, we did not use the atomistic value for $E_{\text{det}}^{\text{Esc}}$, but rather the elastic estimate according to Eq. 4.5.

Fig. 4.11 shows energy distributions for Cu+33 at.% Ni. The other alloys exhibit similar behavior, see Fig. 4.12. Applied stresses tend to eliminate the high energy barriers. The additional work done by the applied stresses as the cross-slip segment length increases are

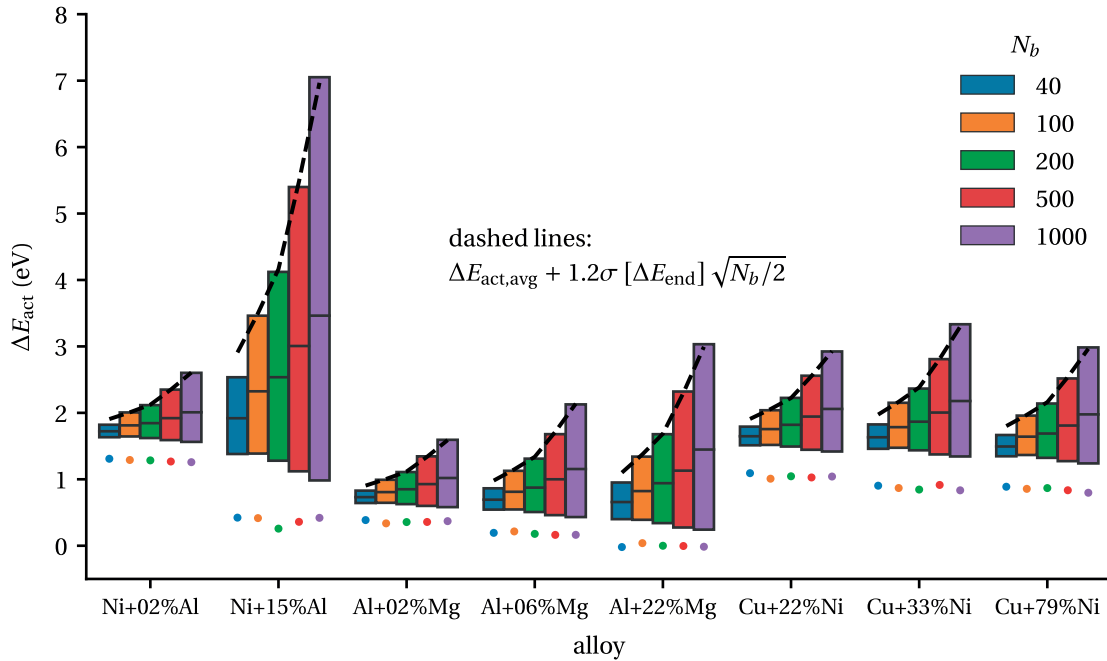


Figure 4.9: Distributions of ΔE_{act} for different alloys and dislocation lengths N_b ; the upper and lower edge of each box represent the third and second quartile of the data, i.e. 50% of all values lie in this range; the horizontal line indicates the median; the dot marks the minimum value

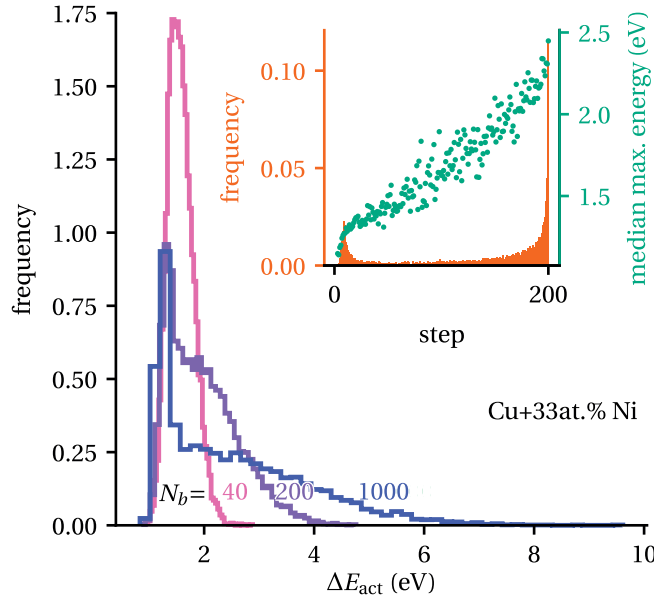


Figure 4.10: Histograms of activation energy distributions in Cu+33 at.% Ni for three dislocation lengths N_b (sample size 10000, no periodic boundaries); inset: distribution of the step at which the maximum occurs (histogram, left axis) and median energy of those maxima that occur on a particular step (points, right axis)

more than sufficient to overcome the slowly accumulating random energies that cause the large barriers. A Schmid stress on the cross-slip plane is particularly effective, with the third quartile being reduced by 1.1 eV upon increasing the Schmid stress from 1 MPa to 5 MPa. Such low Schmid stress could easily be reached in real materials due to long range stresses and stress fluctuations caused by the local dislocation network. Escaig stresses, by comparison, are less effective in that higher stresses in the range of 25–50 MPa are required to eliminate the high activation barriers. Nonetheless, such stress levels remain moderate. Note that the observed stress effects are more complicated than in elastic or atomistic models for pure metals. Usually, $\tau_{\text{glide}}^{\text{Esc}}$ is expected to be the most effective stress for reducing the activation energy while $\tau_{\text{cross}}^{\text{Sch}}$ is supposed to be least effective [60]. Fig. 4.11 shows that this is only true at higher stresses.

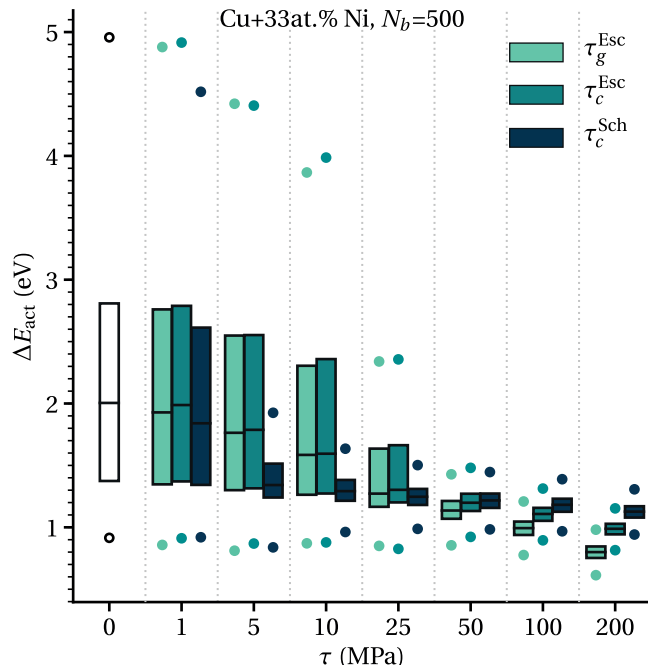


Figure 4.11: Activation energy distributions in Cu+33 at.% Ni with $N_b = 500$ for different Escaig and Schmid stresses; the upper and lower edge of each box represent the third and second quartile of the data, i.e. 50% of all values lie in this range; the horizontal line indicates the median; the dots mark the minimum and maximum value of each dataset

The characteristic stress required to eliminate high activation energies can be estimated as follows. As noted above, the maximum barrier is unlikely to occur at the end of the random walk if the magnitude of work performed by the external stress after N_b steps is likely to exceed the accumulated random energy contributions. As shown in Fig. 4.9, a majority of the activation energies have an energy of less than $\Delta E_{\text{act},\text{avg}} + \sigma [\Delta E_{\text{end}}] 1.2\sqrt{N_b/2}$. Thus, the work should exceed $\sigma [\Delta E_{\text{end}}] 1.2\sqrt{N_b/2}$, and limit stresses can be obtained by solving

$$N_b E_{\text{det}}^{\text{Esc}}(\tau_{\text{glide}}^{\text{Esc}}, \tau_{\text{cross}}^{\text{Esc}}) + E_{\text{det}}^{\text{Sch}}(\tau_{\text{cross}}^{\text{Sch}}, N_b) + \sigma [\Delta E_{\text{end}}] 1.2\sqrt{N_b/2} = 0. \quad (4.11)$$

The energy change of the constriction on the glide plane due to $\tau_{\text{glide}}^{\text{Esc}}$ has been ignored. It only contributes an offset to the total energy and thus has no influence on the position of the maximum. Assuming pure Escaig and Schmid stresses, one obtains characteristic stresses of

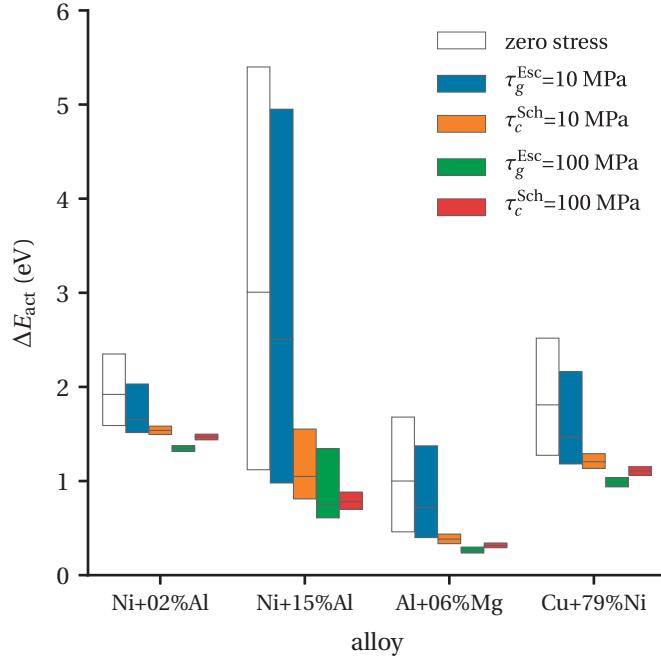


Figure 4.12: Activation energy distributions in solid solution alloys for $N_b = 500$ and high or low Escaig and Schmid stresses; the upper and lower edge of each box represent the third and second quartile of the data, i.e. 50% of all values lie in this range; the horizontal line indicates the median;

$\tau_{\text{glide}}^{\text{Esc}} = 21.3 \text{ MPa}$, $\tau_{\text{glide}}^{\text{Esc}} = 20.7 \text{ MPa}$, and $\tau_{\text{cross}}^{\text{Sch}} = 2.1 \text{ MPa}$ for Cu+33 at.% Ni at $N_b = 500$, consistent with the results in Fig. 4.11.

In summary, moderate applied stresses that act to facilitate cross-slip are sufficient to eliminate high barriers and drive the entire distribution of activation barriers to much lower values than the mean value at short lengths.

4.4.3 Weakest-Link Scaling

The previous observations motivate us to treat cross-slip under stress as a weakest-link problem. At sufficiently large stress, most maxima occur early in the random walk. Thus, the activation energy distribution at a long length N_b can be inferred from the corresponding distribution for a much shorter length N_{ref} by accounting for the number $n = N_b/N_{\text{ref}}$ of approximately statistically-independent segments of size N_{ref} at which cross-slip can initiate. The cumulative distribution $P(\Delta E_{\text{act}}, N_b, \tau)$ for length N_b at the given stress τ should then obey

$$P(\Delta E_{\text{act}}, N_b, \tau) = 1 - (1 - P(\Delta E_{\text{act}}, N_{\text{ref}}, \tau))^{(N_b/N_{\text{ref}})}, \quad (4.12)$$

where $P(\Delta E_{\text{act}}, N_{\text{ref}}, \tau)$ is the cumulative distribution function of activation energies at N_{ref} at the given stress. To test this hypothesis, we carried out further random walk calculations with lengths $N_b = 5000$ and $N_b = 10000$. We then used the random walk data from calculations at $N_b = 500$ as reference, i.e. $N_{\text{ref}} = 500$. Calculations were carried out for Cu+33 at.% Ni,

Al+06 at.% Mg and Ni+15 at.% Al.

Fig. 4.13 shows the cumulative distribution functions for the cross-slip activation energy for 5 MPa Schmid stress on the cross-slip plane, and also 50 MPa for Cu+33 at.% Ni, for $N_b = 500$, $N_b = 5000$, and $N_b = 10000$. The figure also shows the predictions for $N_b = 5000$ and $N_b = 10000$ as obtained from weak-link scaling. The weak-link scaling is very accurate, within fractions of a percent, in all cases. The agreement is achieved because, even at the lower stress level, all large barriers have been eliminated within the length $N_b = 500$.

Fig. 4.14 shows the cumulative distribution functions for the cross-slip activation energy at both 5 MPa Escaig stress, for Cu+33 at.% Ni and Ni+15 at.% Al. As can be expected from Fig. 4.11 and Fig. 4.12, the weakest-link prediction is not accurate at this low stress because the largest barriers can be encountered at lengths larger than the reference length $N_b = 500$. Thus, higher activation energies are underestimated. The error is smaller in Cu+33 at.% Ni because the characteristic stress calculated with Eq. 4.11 is only $\tau_{\text{cross}}^{\text{Esc}} = 6.6$ MPa for $N_b = 5000$ and $\tau_{\text{cross}}^{\text{Esc}} = 4.7$ MPa for $N_b = 10000$, close to 5 MPa. Nevertheless, the differences in median values are only -0.12 eV and -0.08 eV, respectively, and so the weak-link scaling captures much of the shift of the activation barriers to lower values, but overestimates the shift.

At 50 MPa Escaig stress, the prediction of weak-link scaling is excellent. At this stress level, all large barriers are overcome well within the length of $N_b = 500$, making the weak-link model applicable. This is consistent with the estimates for the characteristic stresses of $\tau_{\text{cross}}^{\text{Esc}} = 20.8$ MPa and 14.8 MPa for $N_b = 5000$ and $N_b = 10000$, respectively, in Ni+15 at.% Al.

4.4.4 Predictions Based on Zero Stress Data

At sufficiently high stresses, Eq. 4.12 allows for the prediction of the activation energy distributions of very long dislocations based on knowledge of the distribution at length N_{ref} . However, the reference distribution needs to be calculated at the given applied stress, and this distribution is not readily accessible. Making predictions would be easier if the reference distribution at zero stress could be used, because this distribution is computable from the underlying solute/dislocation and solute/solute interaction energies. At zero stress, however, N_{ref} must then be small so that the reference distribution does not have a large tail at high energy barriers. This suggests using the distribution at the fundamental cross-slip length of $N_b \approx 40$. This length is also accessible by atomistic simulations if suitable potentials are available.

The effect of stress can then be approximated by shifting the reference distribution to lower energies, according to the deterministic change of $\Delta E_{\text{act,avg}}$. However, not all energy levels should be shifted by the same amount. Low barriers typically correspond to paths where the energy barrier occurs early. These barriers are relatively insensitive to the work done by the stress in extending or bowing out the dislocation on the cross-slip plane. Conversely, energy barriers equal to $\Delta E_{\text{act,avg}}$ or higher likely correspond to paths where the maximum occurs later, and these see the full stress effect. To approximate this difference in sensitivity, we make the shift a linear function of ΔE_{act} for $\Delta E_{\text{act}} < \Delta E_{\text{act,avg}}$, i.e.

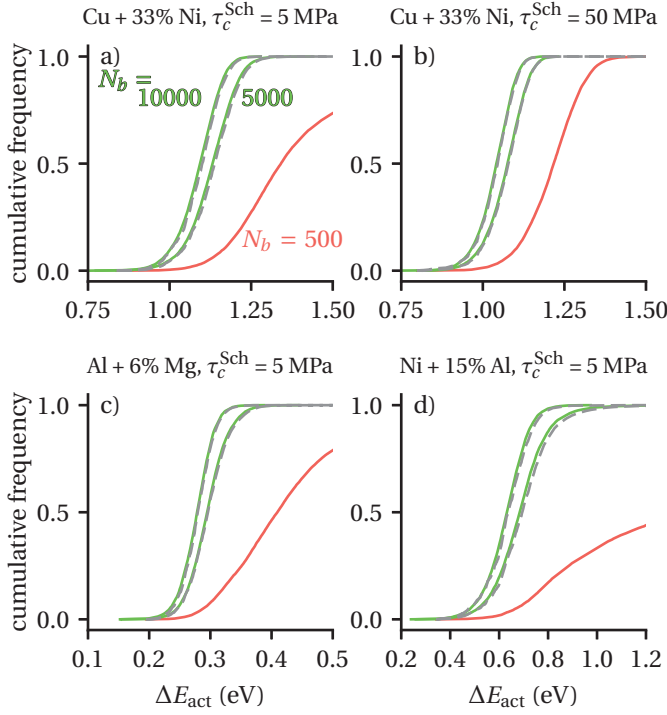


Figure 4.13: Testing the validity of the weakest-link scaling relation (Eq. 4.12); lines: cumulative distributions of ΔE_{act} at 5 or 50 MPa Schmid stress on the cross-slip plane, in different alloys and for different lengths N_b ; red: distribution for $N_b = 500$; green: distributions for $N_b = 5000$ and $N_b = 10000$; red and green data were calculated with the random walk model; dashed lines: predictions using Eq. 4.12 for $N_b = 5000$ and $N_b = 10000$, based on the data for $N_b = 500$

$P(\Delta E_{\text{act}}, N_{\text{ref}}, \tau) \rightarrow P(\Delta E_{\text{act}} - \Delta E_{\text{shift}}, N_{\text{ref}}, 0)$ with

$$\Delta E_{\text{shift}} = \begin{cases} \left[\left(\frac{f_c - 1}{2} \right) \Delta E_{\text{act,avg}} + \left(\frac{\Delta E_{\text{act,avg}}(\tau)}{\Delta E_{\text{act,avg}}} - \frac{f_c + 1}{2} \right) \Delta E_{\text{act}} \right] & \Delta E_{\text{act}} < \Delta E_{\text{act,avg}}, \\ \Delta E_{\text{act,avg}}(\tau) - \Delta E_{\text{act,avg}} & \Delta E_{\text{act}} \geq \Delta E_{\text{act,avg}} \end{cases}, \quad (4.13)$$

where $\Delta E_{\text{act,avg}}(\tau)$ is the average-alloy activation energy at stress τ , i.e. the maximum of E_{det} . The first term for $\Delta E_{\text{act}} < \Delta E_{\text{act,avg}}$ is the contribution from the change of energy of the constriction on the glide plane, which applies to all paths, and the second term is the contribution from the work on the cross-slip plane, which has only limited effect for paths with low ΔE_{act} , as explained above. Note that paths with $\Delta E_{\text{act}} \geq \Delta E_{\text{act,avg}}$ see the full stress effect.

Using the activation energy distribution of $40b$ long lines as reference data, we predicted the corresponding activation energy distributions at a dislocation length of $1000b$ under Schmid or Escaig stresses of 50, 200 and 600 MPa. Note that $N_b = 1000$ corresponds to a dislocation density of roughly 10^{13} m^{-2} in the alloys considered here, typical of the range during deformation of engineering alloys. The highest stress level is not necessarily relevant for real alloys. For example, reported stresses in compression tests with Al+3 wt.% Mg at room temperature are below 300 MPa [75]. Cu-Ni single crystals deform in room-temperature tensile tests under resolved shear stresses not higher than 140 MPa [93]. Nevertheless, it is

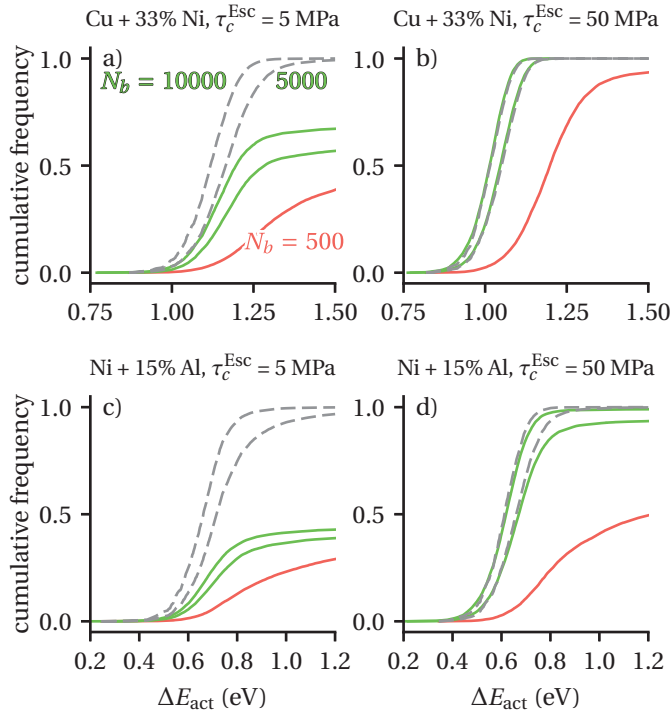


Figure 4.14: Cumulative distributions of ΔE_{act} at 5 or 50 MPa Escaig stress on the cross-slip plane, in different alloys and for different lengths N_b ; red: distribution for $N_b = 500$; green: distributions for $N_b = 5000$ and $N_b = 10000$; red and green data were calculated with the random walk model; dashed lines: predictions using Eq. 4.12 for $N_b = 5000$ and $N_b = 10000$, based on the data for $N_b = 500$

interesting to check the validity of our approach in the limit of very high stress.

In the following, we discuss predictions for Cu+33 at.% Ni, Al+06 at.% Mg and Ni+15 at.% Al. Note that these alloys have increasing ratios of $\sigma [\Delta E_{\text{end}}] / \Delta E_{\text{act,avg}}$, meaning that random fluctuations become more important relative to the deterministic energy. In Fig. 4.15, the predictions for Cu+33 at.% Ni and $N_b = 1000b$ are compared to the results of full random walk calculations and the average-alloy activation energies that one would expect based on E_{det} . The different stress types $\tau_{\text{cross}}^{\text{Esc}}$, $\tau_{\text{cross}}^{\text{Sch}}$ and $\tau_{\text{glide}}^{\text{Esc}}$ are considered separately in subfigures a), b) and c). We see that the predictions (dashed lines) are close to the direct results (solid lines) at all stress levels (colors). In some cases, for example at $\tau_{\text{cross}}^{\text{Esc}} = 200$ MPa, ΔE_{act} is overestimated by roughly 0.1 eV. Furthermore, the predicted distributions tend to be slightly broader at 200 MPa and 600 MPa. However, these errors are small compared to the error one would make by using only the average-alloy activation energy (shown as the cross symbols in the figures). At the median value, for example, the error of the average alloy is typically four to five times larger than the error of the weakest-link prediction. When predicting cross-slip rates, this error would be further amplified by the exponential weighting of ΔE_{act} in Eq. 1.7.

In Al+06 at.% Mg, the predictions are satisfactory as well, see Fig. 4.16. The error is typically less than 0.1 eV. At $\tau_{\text{cross}}^{\text{Esc}} = 50$ MPa and $\tau_{\text{cross}}^{\text{Esc}} = 50$ MPa, the highest 10–15% of energies are

4.4. Cross-Slip of Long Dislocations

underestimated, because some high barriers have not been eliminated by the stress in the direct calculations. However, the other 90–85% of energies are predicted accurately, and it are the these lower energies which are more important, due to the exponential weighting in Eq. 1.7.

The mismatch between prediction and direct calculations at 50 MPa Escaig stress is even stronger in Ni+15 at.% Al, see Fig. 4.17. ΔE_{act} is underestimated above the median value. However, this error is not surprising, since 50 MPa is just above the limit stresses of $\tau_{\text{glide}}^{\text{Esc}} = 48 \text{ MPa}$ and $\tau_{\text{cross}}^{\text{Esc}} = 46 \text{ MPa}$ according to Eq. 4.11. The prediction is nevertheless useful, since it indicates that a significant number of paths have an activation energy of around 0.7 eV, hence thermally activated cross-slip is plausible. Based on the average-alloy value of 1.89 eV, one would perhaps rule it out. At the other stress levels, the prediction is much more accurate.

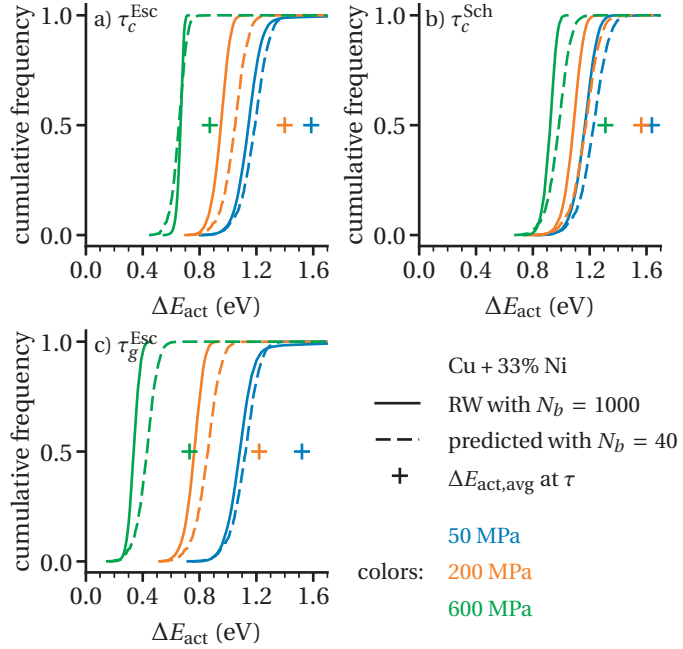


Figure 4.15: Cumulative distributions of cross-slip activation energies in Cu+33 at.% Ni under stress; dashed lines are predictions made with Eq. 4.12, based on shifted zero-stress distributions for $N_b = 40$

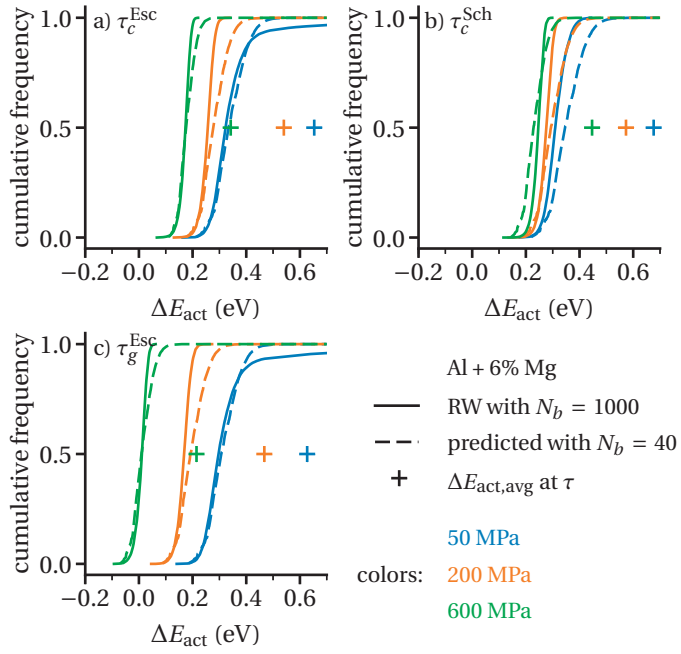


Figure 4.16: Cumulative distributions of ΔE_{act} in Al+06 at.% Mg under stress; dashed lines are predictions made with Eq. 4.12, based on shifted zero-stress distributions for $N_b = 40$

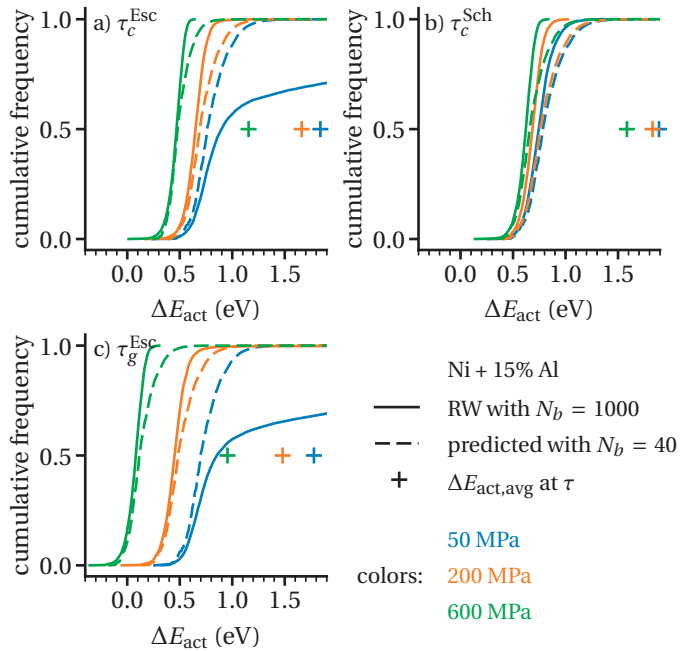


Figure 4.17: Cumulative distributions of ΔE_{act} in Ni+15 at.% Al under stress; dashed lines are predictions made with Eq. 4.12, based on shifted zero-stress distributions for $N_b = 40$. The simulated data (solid lines) shows that a 50 MPa Escaig stress is not sufficient to eliminate all high energy barriers. The prediction according to Eq. 4.12 cannot predict high barriers, hence there is a discrepancy.

4.5 Discussion

We have demonstrated that (i) the standard deviation $\sigma [\Delta E_{\text{end}}]$ of random energy fluctuations caused by cross-slip in random alloys can be predicted accurately based on solute/dislocation and solute/solute interaction energies; (ii) the random walk model captures the accumulation of energy fluctuations during cross-slip over long lengths, such that (iii) the distribution of the cross-slip activation energies ΔE_{act} can be computed for any dislocation length, including the range of practical interest ($\sim 10^3 b$), where direct atomistic calculations are infeasible. We find that such long dislocations frequently have very high ΔE_{act} , on the order of several electron volts, but that moderate stresses (10^0 – 10^1 MPa), especially Schmid stresses, eliminate these barriers and lead to activation barriers that are much lower than the average value. We have then shown that cross-slip becomes a weakest-link problem, enabling computation of barriers for long lengths in terms of barriers computed at shorter lengths. We now discuss implications of these results and some further aspects of our model.

First of all, complete cross-slip of long dislocations ($10^3 b$) is unlikely at zero stress, because of the increasing frequency of high activation energies. Due to the exponential weighting of ΔE_{act} in Eq. 1.7, these barriers are exceedingly unlikely to be overcome by thermal activation alone. Shorter subsegments could perhaps cross-slip, but equilibrium lengths of such segments are expected to be on the order of 10^2 – $10^3 b$, see App. A.5, and are therefore unlikely to be reached. However, when these high barriers are eliminated by an external Escaig or Schmid stress, then ΔE_{act} is typically much lower than the value $\Delta E_{\text{act,avg}}(\tau)$ that one would expect based on an average-alloy model. Thus, cross-slip is much faster than expected. For example, in Cu+33 at.% Ni with a 50 MPa Escaig stress on the glide plane, the median activation energy for a $1000b$ long dislocation is 1.14 eV, whereas the average-alloy estimate is 1.59 eV. Assuming constant prefactors in Eq. 1.7, the rate of cross-slip in the random alloy is roughly 7 orders of magnitude faster than expected based on an average-alloy model. In Al+02 at.% Mg and Ni+15 at.% Al, the rate is increased by ca. 4 and 16 orders of magnitude, respectively.

Under stress, cross-slip becomes a weakest-link problem because the cross-slipped segment expands spontaneously after nucleation. The distribution of ΔE_{act} depends on (i) the distribution of ΔE_{act} for cross-slip nucleation, which takes place over a length much shorter than the total length, and (ii) how many times this distribution is sampled over the total length. We observed that even small Schmid stresses on the cross-slip plane, on the order of a few MPa, eliminate high barriers and make cross-slip a weakest-link problem. Thus, cross-slip of moving dislocations is likely always a weakest-link problem, since it implies a Schmid stress $\tau_{\text{glide}}^{\text{Sch}}$ on the glide plane. Except in high symmetry cases, the applied stress will likely have nonzero Schmid components on both planes, hence the conditions for weakest-link scaling are likely to be fulfilled. The observed critical Schmid stresses for weakest-link scaling are on the order of a few MPa, and therefore comparable to the Peierls stress in pure metals.

In alloys, one additionally has to consider solute strengthening. Recall that we have neglected energy fluctuations during bowing-out, i.e. we have neglected solute strengthening on the cross-slip plane. However, if we assume that the external stress is sufficiently high to make dislocations move on the glide plane, then it is, as before, likely that critical stresses on the cross-slip plane are sufficient, so that a bow-out can be formed.

Chapter 4. Cross-Slip of Long Dislocations

Internal stresses have to be considered as well. For example, the critical stress for weakest-link scaling can be overcome easily in a pile-up of n dislocations against an obstacle, where the external stress is amplified by a factor equal n [18]. Pile-ups were proposed early on as likely sites for cross-slip [125]. Dislocations that do not reside in pile-ups nevertheless experience stresses from other dislocations, e.g. forest dislocations. A particularly interesting scenario is cross-slip of a dislocation in a screw dipole, which can lead to annihilation (see Refs. [108, 111, 145] for atomistic simulations of this process). Here, one would expect large attractive stresses.

The easier/faster cross-slip implied by our results here would have several consequences for plastic deformation behavior. Screw dipole annihilation plays a role in fatigue and may determine the saturation stress [11], hence our observations may help to interpret fatigue of alloys. Due to the faster annihilation by cross-slip one should expect larger minimum stable dipole heights as in pure metals, and hence lower saturation stresses. Discrete [54, 77] and continuum dislocation dynamics calculations [157–159] have demonstrated the importance of cross-slip for dislocation microstructure formation. A cellular microstructure is only observed if cross-slip is activated in such calculations. Thus, one would expect to see a well-developed cellular microstructure in deformed random alloys. Moreover, this microstructure should form more rapidly with strain than in pure metals. Considering the results of Xia and coworkers [158], one would also expect higher yield points and an increased hardening rate. However, it might be difficult to distinguish these effects from other solute strengthening effects.

The case of Ni+15 at.% shows that low values of ΔE_{act} can be realized even in alloys with high $\Delta E_{\text{act,avg}}$ if σ [ΔE_{end}] is high and moderate stresses are applied. In High Entropy Alloys [162], where σ [ΔE_{end}] can be expected to be high due to compositional disorder, cross-slip should therefore be relatively easy. Indeed, Rao et al. [105] recently observed spontaneous cross-slip in atomistic simulations of regular dislocation slip in a Co₄₀Fe_{16.67}Ni_{36.67}Ti_{16.67} random alloy at 300 K, even though $\Delta E_{\text{act,avg}}$ is 4.6–4.9 eV. The effective value of ΔE_{act} was estimated to be 0.3 eV. Liu et al. [73] observed that twins in Al_{0.1}CoCrFeNi were formed by a mechanism which involves cross-slip of dislocations that were piled up against a stacking fault. These studies show the potential importance of cross-slip in HEAs. Somewhat conflicting in this sense is the study of Cao et al. [15], who performed creep tests with a Al_xCoCrFeNi ($x=0.15, 0.60$) HEA and determined activation volumes of 32–52 b^3 , which are consistent with a cross-slip mechanism [102], but also high activation energies (3.5–4 eV). Furthermore, Otto and coworkers [94] observed planar slip in CoCrFeMnNi, which seems to be in conflict with our suggestion of easy cross-slip. The authors attributed planar slip to short-range order (SRO). Gerold and Karnthaler [44] argued that SRO causes planar slip because leading dislocations in a group destroy this order, resulting in glide plane softening and a preference for further slip on this plane. Thus, it seems, that SRO would not increase the energy barrier for cross-slip *per se*. The exact effect of SRO on ΔE_{act} is unclear, but one may speculate that correlations in the solute distributions would reduce σ [ΔE_{act}]. Recall that we assumed a completely random solute distribution. Our model also contradicts a model of planar slip by Hong and Laird [53]. They argued that solutes create a friction stress on the partial dislocations, which impedes constriction and hence cross-slip. The friction stress increases with atomic size misfit and solute content, hence it would seem that solute addition should generally impede cross-slip. However, we have shown that one needs to consider solute binding energy fluctuations, which can be positive or negative and thus impede or facilitate cross-slip.

A few other aspects of our model merit discussion. Some approximations were made when modeling the deterministic energy $E_{\text{det}}(i)$ ($i = 1 \dots N_b$). The current model is appealing because of its simplicity. The energy profile is reduced to two variables, the energy of a single constriction and the cross-slipped length at which the constrictions on the cross-slip plane are approximately fully formed. Both can be determined using atomistic or elastic models. We obtained a satisfactory agreement between E_{det} and the atomistic data by choosing a formation length of $10b$. Indeed, the relative energy has almost reached its final value of $\Delta E_{\text{act,avg}}$ at this point, see Fig. 4.5. Strictly, one would have to choose a value of $20b$, i.e. half of the total cell length of $40b$, which we identified in our previous publication [88] as the periodic length in Ni at which $\Delta E_{\text{act,avg}}$ becomes independent of length. However, it is easy to see that the quadratic energy profile would then underestimate the relative energy more strongly in the region of constriction formation. Better approximations of the energy-length profile could be constructed using a different functional form. For example, in Püschl and Schöck's anisotropic-elastic model, the energy of the two half-constrictions on the cross-slip plane varies with cross-slipped length L and dissociation width d approximately as $2/\pi \arctan(pL/d)2E_c$, where $2E_c$ is the energy of two well-separated half-constrictions, and p is a numerical factor in the range 0.8–1.4. The model of E_{det} under stress could be improved by including the effect of $\tau_{\text{cross}}^{\text{Esc}}$ on the constriction on the cross-slip plane. This could be done by simultaneously scaling the length and the energy of this constriction.

We have also assumed that the ideal Friedel-Escaig mechanism is the operative cross-slip mechanism. This means that the segments on the glide and cross-slip plane are joined by point constrictions. Oren et al. [92] have recently observed a variation of this mechanism in molecular dynamics calculations, where fully constricted segments are formed in the process. Analysis of our atomistic configurations (at zero stress) with the Dislocation Analysis (DXA) algorithm implemented in Ovito [135, 136], shows that such segments occur frequently. In random alloys, lengths of roughly $3b$ are frequently seen before the transition state. At the transition state, however, the fully constricted length is typically only around $1b$. Since the length at the transition state is typically short, it is a fair assumption to use the activation energy of ideal Friedel-Escaig cross-slip for $\Delta E_{\text{act,avg}}$.

Three more subtle assumptions were made when modeling the random energy. First, by assigning a random energy change to $1b$ segments, we associate solute-dislocation binding energies with such short segments. In reality, however, the binding energy quantifies the interaction between the solute and an infinitely long dislocation. The energy has contributions from atoms whose distance to the solute atom along the dislocation line is greater than $1b$. However, the interaction energy drops off rather quickly, due to the $1/r^2$ scaling of the solute stress field. Moreover, a sufficiently long line is realized after cross-slip of a few $1b$ segments. These are the likely reasons why our approximation does not have a significant effect on the results. Another approximation was made in the derivation of $\sigma [\Delta E_{\text{end}}]$. The contributions to ΔE_{end} from solute-dislocation and solute-solute binding are sums of energies times occupation variables, which are Bernoulli random variables. Hence, these contributions are discrete random variables. Here, we assume that they are normally distributed, even for $1b$ segments. In the case of the contribution from solute-solute binding, this approximation is expected to deteriorate when the number of contributing pairs is low, in a similar way as the approximation of a binomial distribution $B(n, p)$ with a normal distribution deteriorates at low n and p . The slight overestimation of $\sigma [\Delta E_{\text{act}}]$ of Ni+02 at.% Al is perhaps an indication of

Chapter 4. Cross-Slip of Long Dislocations

this problem. Furthermore, we have calculated solute-dislocation binding energies using the dislocation core structure at zero stress. Thus, our model of σ [$\Delta E_{\text{end,s-d}}$] does not account for a change of dissociation width d under stress. Since the highest contributions to $\Delta E_{\text{end,s-d}}$ come from the immediate core region of the partial dislocations, the error of approximation should be small, but one must be careful in alloys where there is significant interaction between solutes and the stacking fault, and at high Escaig stresses. Similarly, σ [$\Delta E_{\text{end,s-s}}$] was calculated using the zero-stress value of d . However, here one could simply use a stress-dependent value.

5 Summary

In this thesis, dislocation cross-slip in Face-Centered Cubic solid solutions has been studied using a combination of atomistic simulations and statistical modeling. Atomistic calculations of cross-slip transition paths in various Ni-Al, Al-Mg and Cu-Ni solutions have shown that cross-slip is controlled by solute fluctuations, i.e. the activation energy ΔE_{act} for cross-slip is a stochastic variable with a large variance. The change of the mean value with concentration is small compared to the variance. Therefore, it is not sufficient to consider only average alloying effects, e.g. a change of the mean stacking fault energy, when estimating the propensity for cross-slip in alloys. At moderate stresses, typical values of ΔE_{act} are much lower than the average value $\Delta E_{\text{act,avg}}$, hence cross-slip is much faster than expected.

Two statistical models of the activation energy distribution have been presented. For short ($40b$) dislocations, a linear correlation $\Delta E_{\text{act}} \approx \Delta E_{\text{act,avg}} + 1/2\Delta E_{\text{end}}$ holds, where $\Delta E_{\text{act,avg}}$ is the activation energy in the average alloy, and ΔE_{end} is the energy difference between the fully dissociated dislocation on the glide and cross-slip plane, respectively. Using this correlation, it is possible to estimate the distribution of ΔE_{act} based on the distribution of ΔE_{end} , which is approximately normal with mean zero and standard deviation $\sigma [\Delta E_{\text{end}}]$. The origin of ΔE_{end} are changes in solute-dislocation and solute-solute binding energies. The latter comes from cutting or formation of solute pairs, which occurs when the stacking fault of the dislocation is destroyed on the glide plane and re-generated on the cross-slip plane. In the first part of the thesis, we presented a parameter-free, analytical model of $\sigma [\Delta E_{\text{end}}]$, which, however, is limited to first nearest neighbor pairs of solutes. Nevertheless, the atomistic and analytical calculations indicate that ΔE_{act} for cross-slip nucleation can be much lower than expected based on average-alloy models.

The activation energy for cross-slip of dislocations with a length of hundreds or thousands of Burgers vectors was discussed in the second part of the thesis. At such lengths, transition path calculations become cumbersome or infeasible. Therefore, a random walk model was developed, which allows to predict the activation energy distribution based on knowledge of solute binding energies, the activation energy ΔE_{act} and constriction size N_c in the corresponding average alloy, and basic material properties like the elastic constants and the stacking fault energy. Furthermore, the model accounts for stress effects. The dislocation is partitioned into $1b$ long segments, and cross-slip is the discrete process of moving them one by one from the glide plane to the cross-slip plane. Each step causes a (i) deterministic energy

Chapter 5. Summary

change, due to constriction formation and the work of an external stress; and (ii) a random change of ΔE_{end} . The deterministic energy depends on $\Delta E_{\text{act,avg}}$ and the typical length of the double-constriction that is formed in the process. The work of the external stress can be calculated based on zero-stress material parameters. An extended model for the random fluctuations in ΔE_{end} was presented, which accounts for first to eighth nearest neighbor pairs of solutes and correlations between loss and formation of pairs of different order. The random walk model accurately predicts the distributions of ΔE_{act} for $40b$ long dislocations and the correlation between ΔE_{act} and ΔE_{end} that was seen in this case. Cross-slip of long dislocations (10^2 – 10^3 b) is unlikely at zero stress. High values of ΔE_{act} , on the order of several electron volt, become more frequent with increasing length, whereas the lowest observed activation energies change only little. High values of ΔE_{act} are associated with cross-slip paths where the maximum occurs late, and these barrier can be eliminated by an applied stress. Thus, cross-slip becomes a weakest link problem at sufficiently high stresses. The governing energy barriers are those for nucleation of a short cross-slipped segment, hence the distribution of ΔE_{act} for a long dislocation can be obtained by scaling the distribution for a shorter one. At sufficiently high stresses, the distribution may even be inferred from the distribution for a $40b$ long segment at zero stress.

6 Outlook

The current study has shed light on important aspects of dislocation cross-slip in FCC solid solution alloys and enabled prediction of the corresponding activation energies ΔE_{act} at different levels of approximation. Our results may help other researchers to interpret simulations and experiments where unexpected cross-slip is observed. For example, Rao et al. [105] recently observed cross-slip in a molecular dynamics simulation of regular slip in a High Entropy Alloy (HEA). According to average-alloy models, cross-slip is exceedingly unlikely because $\Delta E_{\text{act,avg}}$ is 4.6 eV–4.9 eV. Rao et al. explained the low effective barriers with solute concentration fluctuations, in agreement with the results of this thesis.

Considering the observation of Rao et al., it would be interesting to estimate the range of ΔE_{act} for HEAs that are discussed in the literature. In general, $\sigma [\Delta E_{\text{end}}]$ should be large in such highly concentrated multi-component alloys. Accordingly, $\sigma [\Delta E_{\text{act}}]$ should be large as well. A challenge is that interatomic potentials for these alloys are typically not available. However, $\Delta E_{\text{act,avg}}$ can be estimated using anisotropic-elastic models, and the solute binding energies that enter in our model of $\sigma [\Delta E_{\text{end}}]$ can be calculated with density functional theory, see for example Refs. [71, 72, 161]. Thus, it is in principle possible to calculate the range of ΔE_{act} with the random walk model. The results would help to understand trends in dislocation network formation in this class of alloys.

Moreover, we expect that the insights from this thesis will help to improve models of plastic deformation of FCC alloys. For example, our results may help to improve the description of cross-slip in Discrete Dislocation Dynamics (DDD). In the following, we outline how the existing approach for pure metals could be modified in order to enable simulation of solid solution alloys and HEAs. In the approach of Kubin et al. [67], screw dislocation segments can cross-slip on each timestep with a probability

$$P_{\text{step}} = A \frac{l}{l_0} \delta t \exp \left(\frac{(\tau_\mu - \tau_{III}) V_{\text{act}}}{k_B T} \right), \quad (6.1)$$

where A is a numerical coefficient, l the segment length, l_0 a reference length, δt the timestep, τ_μ the stress acting on the dislocation, τ_{III} the critical resolved shear stress at the onset of stage III, and V the activation volume of cross-slip. Note that without the δt this equation corresponds to the rate of cross-slip. In the approach of Hussein et al. [54], the rate is

Chapter 6. Outlook

calculated as

$$r = \omega_A \frac{l}{l_0} \exp\left(\frac{-\left(E_c - V_{act}\left(\tau_{\text{glide}}^{\text{Esc}} - \tau_{\text{cross}}^{\text{Esc}}\right)\right)}{k_B T}\right), \quad (6.2)$$

where ω_A is an attempt frequency. A segment cross-slips if $r \geq 1$. Eq. 6.1 and Eq. 6.2 are appropriate for pure metals, where the activation energy for cross-slip is deterministic. Furthermore, it is reasonable to assume that the total cross-slip rate depends on segment length, since cross-slip can nucleate anywhere along the line with the same ΔE_{act} , and nucleation events are presumably uncorrelated if they occur far away from each other. Analytical considerations [145] also indicate such a dependence. In random solid solutions the situation is different and the equations need to be modified. ΔE_{act} should be used in the numerator in the exponential. However, ΔE_{act} is now a random variable. A new value of ΔE_{act} should be drawn for each screw segment whenever it moves, since the random solute environment changes. The distribution of ΔE_{act} , which depends on stress and dislocation length, could be obtained by scaling a zero-stress reference distribution according to Eq. 4.12. This reference distribution, in turn, needs to be calculated only once, using the random walk model. A technical hurdle is to implement efficient scaling and sampling of the distributions. The program must also check whether Eq. 4.11 is fulfilled¹, so that weakest-link scaling can be used. Note that the probability now depends on length through ΔE_{act} and Eq. 4.11. The pre-exponential factor, on the other hand, should be independent of length. Due to the rules for path selection in our model, there is a unique cross-slip path for each segment in its current solute environment. Thus, the term (l/l_0) should be removed in Eq. 6.1 and Eq. 6.2. The issue of the pre-exponential factor will be discussed further below.

In addition to DDD, our results may improve work hardening laws that account for the evolution of the dislocation density during loading. Some models incorporate dislocation annihilation by cross-slip of opposite dislocation [35, 62, 75, 87]. The rate of annihilation thus depends on the rate of cross-slip. In a pure metal with a single ΔE_{act} , both rates could be written like in Eq. 1.7. In solid solutions, calculating the total cross-slip rate is more complicated. Since ΔE_{act} follows a distribution which depends on dislocation length, one would have to do a double integral over length and energy to get the total rate of cross-slip. For this purpose, it may be necessary to parameterize the reference distribution.

An important task for future work is to test our model experimentally. This is a challenging task, since cross-slip occurs alongside other dislocation processes during deformation of real materials. An indirect test would be to predict the stress-strain curves of alloys at different compositions and temperatures using appropriately revised work hardening models, and to compare the results to experimental measurements. This test is somewhat ambiguous, since one would also test additional assumptions in the work hardening model. Nevertheless, failure of these predictions would cast doubt on our model for the distribution of ΔE_{act} . A more direct test would be to observe individual dislocations and dislocation networks in deformed solid solution alloys, using an electron microscope. The alloy should have a high value of σ [ΔE_{end}], but also a high value of $\Delta E_{act,avg}$. The latter should be so high that thermally activated cross-slip is unlikely if it is not assisted by binding energy fluctuations. If it can

1. “=” should then be replaced by \leq in Eq. 4.11.

be ruled out that nucleation took place at a heterogeneity — which might be difficult or impossible, especially for jog-assisted cross-slip — then observation of cross-slip in the bulk would corroborate our suggestion that fluctuations in the binding energy may lower ΔE_{act} . Furthermore, observation of cross-slip traces on the surface and well-formed cell structures in the interior would indicate that cross-slip is active [157, 158]. The alloy should not exhibit short range order (SRO), which must be ruled out as a cause for slip planarity and absence of a cell structure. Similarly, our model could be used to make a prediction about the transition between cellular and planar dislocation structures as a function of alloy composition, which could then be tested experimentally. For example, Hong and Laird [53] tried to explain the transition in CuZn and CuAl with their cross-slip model. Finally, it might be useful to determine the apparent activation energy and activation volume of cross-slip in solid solutions using the technique of Bonneville and Escaig [9, 10].

Having discussed possible applications of the model and experimental validation, we now turn to further aspects of cross-slip that should be addressed in future work. First of all, the pre-exponential factor of the cross-slip rate (A in Eq. 1.7) should be studied. This factor can be interpreted as an attempt frequency for cross-slip. It would be desirable to have an analytical solution for this frequency in solid solution alloys. Vegge et al. [145] derived an expression for pure metals (Eq. 1.9). However, their solution is invalid here, since it is based on the assumption that a displacement of the critical nucleus along the line direction costs zero energy. In a solid solution, there would be a random change of binding energies, hence this assumption is violated. Thus, an analytical solution for the pre-exponential factor in solid solutions is an open problem. Furthermore, the validity of harmonic transition state theory (HTST) for describing the rate of cross-slip should be examined. There could be anharmonic effects, for example from thermal expansion and softening. They have been shown to increase the rate of dislocation nucleation [116] and glide through a solute field [118], respectively. One could perhaps improve the rate estimate by accounting for the temperature dependence of the material properties that appear in our model, for example the elastic constants and the stacking fault energy. Furthermore, it should be checked whether A and ΔE_{act} are correlated according to the Meyer-Neldel [80] compensation rule. Low values of ΔE_{act} would then be compensated by low values of A . One may speculate that there is a small compensation effect due to the correlation between nucleus size and activation energy. We have seen that cross-slip paths with low ΔE_{act} tend to be those where the maximum occurs early on, at a short cross-slipped length. The vibrational modes at the transition state should depend on the size of the critical nucleus, which would then establish a link between the attempt frequency and ΔE_{act} . However, this effect is likely small, because the size of the critical nucleus does not vary by orders of magnitude at moderate stresses. To address the question, the cross-slip rate should be calculated directly using atomistic simulations, for example with the method of Vegge et al. [145] and Oren et al. [92]. They subjected a screw dipole to stress and measured the waiting time for annihilation by cross-slip at different temperatures. A and ΔE_{act} can then be obtained from an Arrhenius plot, i.e. a plot of $\ln r = A - \Delta E_{\text{act}}/k_B T$ as a function of $1/T$. Alternatively, the rate could be estimated using the Finite Temperature String Method [28, 139] or transition path sampling techniques like the Transition Interface Sampling Method [138].

Moreover, the effects of short range order (SRO) on the distribution of ΔE_{act} need to be studied. As speculated in Sec. 4.5, SRO could cause a reduction of $\sigma [\Delta E_{\text{end}}]$, thus ΔE_{act} would be more narrowly distributed around $\Delta E_{\text{act},\text{avg}}$, and cross-slip would become less frequent. This

Chapter 6. Outlook

supposition could be tested by calculating minimum energy paths for cross-slip in solute environments with SRO. The simulations would be very similar to those described in Sec. 2.3, except that correlations would have to be introduced in the solute distributions. However, deriving an analytical model would be more difficult. Occupation variables for different sites around the dislocation are now correlated, hence products of these variables cannot simply be replaced by powers of solute concentrations when taking averages.

In addition to SRO, it would be useful to study the effect of solute segregation. It is likely that ΔE_{act} increases, since the cross-slipping dislocation leaves a favorable solute environment. Such an effect is seen in the study of Andrews et al. [2], who calculated the energy for constriction formation in a segregated solute field using a line tension model. The constriction energy increases with solute content. It would be interesting to supplement this study with atomistic minimum energy path calculations of cross-slip in a segregated alloy. Moreover, it would be interesting to study the effect of segregation on cross-slip at heterogeneities, for example at intersections with forest dislocations. Segregation should be stronger around immobile dislocations, thus cross-slip at intersections could potentially be more affected than cross-slip of mobile dislocations in the bulk.

Another point for further study is the role of other point defects like interstitials and vacancies. In the case of interstitials, one would expect a stronger interaction with the cross-slipping dislocation due to stronger distortion of the lattice by the interstitial. On the other hand, the concentration of interstitials is typically lower. For example, the maximum concentration of C in austenitic Fe is about 2%. Thus, the strength of interstitial effects on cross-slip is not immediately clear. Like in the case of SRO and segregation, the first step towards understanding this effect would be to perform minimum energy path calculations with corresponding alloys. In particular, it would be interesting to perform calculations with hydrogen atoms, which are very mobile and can therefore segregate to the dislocation on the glide plane. For the reasons outlined above, it is likely that they impede cross-slip. The effect of vacancies, on the other hand, can perhaps be studied using a modified version of the solute binding energy model that was used here, where vacancies are effectively treated like solute atoms. Like in the case of solute atoms, segregation would complicate the analysis.

In summary, there are numerous points for future research. The results of this thesis could be used to improve models of FCC strength. Moreover, our model should be tested experimentally and the pre-exponential factor of the cross-slip rate should be studied. Finally, it would be interesting to study the effects of other point defects, SRO, segregation, as well as solute effects on heterogeneous cross-slip.

A Appendix

A.1 Calculation of Basic Properties

Basic properties of average and true random alloys of Ni-Al, Cu-Ni and Al-Mg are listed in Tab. A.1, Tab. A.2 and Tab. A.3. Fig. A.1 shows the relative differences between average alloy and random alloy values, except for the difference in lattice parameter, which is smaller than 0.1% in all cases. The methods for calculating the properties are explained in Sec. A.1.1 and Sec. A.1.2.

Table A.1: Basic properties of average and true random alloys of Ni-Al; solute concentration c in at.%; screw dislocation dissociation width d in Å; intrinsic stacking fault energy γ_{SF} in mJ m^{-2} ; cubic elastic constants C_{11} , C_{12} and C_{44} in GPa; A/R: average/true random alloy value

c(Al)	a		d		γ_{SF}		C_{11}		C_{12}		C_{44}	
	A	R	A	R	A	R	A	R	A	R	A	R
0	–	3.520	–	10	–	134.4	–	241.3	–	150.8	–	127.3
2	3.521	3.521	10	10	127.0	126.6	237.0	236.9	150.8	151.1	127.1	127.1
4	3.522	3.522	10	10	119.4	120.0	233.2	232.3	150.9	151.3	126.7	126.7
8	3.526	3.525	10	11	103.6	112.6	227.4	223.7	151.0	151.8	125.7	125.7
10	3.529	3.527	10	11	95.6	100.6	225.5	219.6	151.0	152.0	125.1	125.1
12	3.532	3.530	10	11	87.7	93.9	224.5	216.0	151.0	152.1	124.4	124.4
15	3.538	3.535	12	11	75.8	77.7	224.2	211.3	150.8	152.2	123.4	123.2

A.1.1 Average Alloys

The average-alloy lattice parameter was determined by locating the minimum of the cohesive energy curve for a single FCC unit cell with periodic boundary conditions in all directions. For this purpose, the Sequential Least Squares Programming algorithm in PYTHON-SCIPY [58] was used. The potential energy was calculated at each iteration of the minimizer by calling LAMMPS through its Python interface.

The cubic elastic constants C_{11} , C_{12} and C_{44} were calculated using the Elastic script that is shipped with LAMMPS. The configuration was $5 \times 5 \times 5$ FCC unit cells large and periodic boundary were applied in all directions. The script calculates all 21 elastic constants

Appendix A. Appendix

Table A.2: Basic properties of average and true random alloys of Cu-Ni; solute concentration c in at.%; screw dislocation dissociation width d in Å; intrinsic stacking fault energy γ_{SF} in mJ m^{-2} ; cubic elastic constants C_{11} , C_{12} and C_{44} in GPa; A/R: average/true random alloy value

c(Al)	a		d		γ_{SF}		C_{11}		C_{12}		C_{44}	
	A	R	A	R	A	R	A	R	A	R	A	R
0	–	3.615	–	14	–	44.8	–	170.2	–	122.6	–	75.8
10	3.612	3.612	14	13	48.5	49.0	175.2	175.5	123.7	124.1	80.0	80.1
22	3.607	3.606	13	13	54.5	56.1	182.2	182.7	125.7	126.3	85.3	85.3
33	3.599	3.598	13	12	61.5	64.5	189.4	189.9	127.9	128.5	90.4	90.4
68	3.566	3.564	10	11	93.2	97.6	227.6	227.0	148.4	148.3	107.3	107.0
79	3.552	3.551	10	10	105.3	108.7	234.3	234.3	148.9	149.5	112.7	112.5
90	3.537	3.536	10	10	116.9	118.6	240.9	240.8	148.8	149.1	118.9	118.7
100	–	3.520	–	10	–	125.6	–	247.0	–	148.0	–	125.5

Table A.3: Basic properties of average and true random alloys of Al-Mg; solute concentration c in at.%; screw dislocation dissociation width d in Å; intrinsic stacking fault energy γ_{SF} in mJ m^{-2} ; cubic elastic constants C_{11} , C_{12} and C_{44} in GPa; A/R: average/true random alloy value

c(Al)	a		d		γ_{SF}		C_{11}		C_{12}		C_{44}	
	A	R	A	R	A	R	A	R	A	R	A	R
0	–	4.032	–	11	–	101.3	–	118.0	–	62.2	–	36.7
2	4.042	4.041	10	10	95.4	97.6	114.5	114.2	60.4	61.2	34.4	34.2
6	4.062	4.060	10	9	86.7	89.2	106.3	105.6	57.0	58.1	29.8	29.5
10	4.083	4.080	10	9	81.1	85.8	99.4	98.3	54.1	55.2	25.5	25.4
14	4.105	4.101	9	9	78.9	85.8	94.1	93.1	51.8	53.0	21.6	22.1
18	4.127	4.123	9	9	78.9	88.4	91.0	89.7	50.4	51.8	18.4	19.9
22	4.149	4.145	9	9	81.4	89.9	92.7	87.5	51.3	51.1	17.2	18.6

for a general anisotropic material by applying appropriate strains and measuring the resulting stresses. C_{11} , C_{12} and C_{44} were calculated as the mean values of the corresponding symmetry-equivalent components.

The average screw dislocation splitting width d was determined using the Dislocation Extraction Algorithm (DXA) [136] as implemented in Ovito [135], by taking the average distance between the extracted partial core coordinates in the average-alloy configurations from Ch. 3.

The intrinsic stacking fault energy γ_{SF} was calculated as follows. The basic configuration was a rectangular cuboid which was elongated in z direction. The x , y and z -directions of the laboratory coordinate system were parallel to the $[\bar{1}10]$, $[\bar{1}\bar{1}2]$ and $[111]$ directions of the crystal. The length of the configuration in x and y was more than eight times the cutoff radius of the interatomic potential. The length along z was $24\sqrt{3}a$. Periodic boundary conditions were applied along x and y , and free boundary conditions along z . In a first step, the normal stresses along x and y were reduced below 0.5 bar using the LAMMPS command `fix boxrelax` in conjunction with the CG minimizer. The box relaxation was reset every 1000 steps of the minimizer, but at most 50 times. After pressure relaxation, the energy of the system was

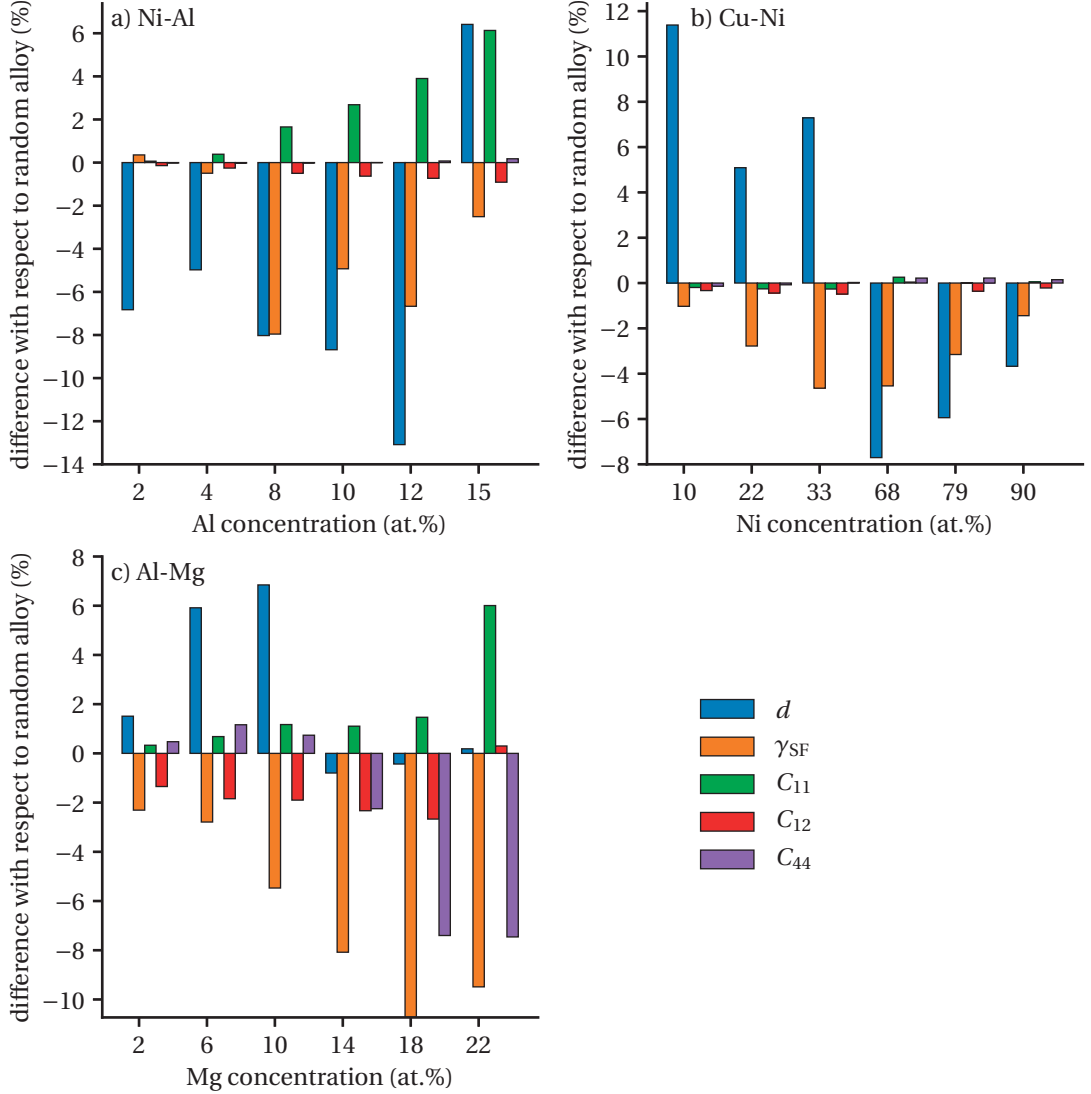


Figure A.1: Difference between the properties of average alloy and the corresponding true random alloys, relative to the value of the true random alloy; a) Ni-Al alloys; b) Cu-Ni alloys; c) Al-Mg alloys

minimized at fixed box size using FIRE. Iterations were stopped when the two-norm of the $3N$ -dimensional vector of atomic forces \mathbf{F} fell below $1 \times 10^{-6} \text{ eV}\text{\AA}^{-1}$ or $1 \times 10^{-8} \text{ eV}\text{\AA}^{-1}$, or after 20000 iterations. A stacking fault was generated by displacing the upper half (along z) of the configuration by $a/6[\bar{2}11]$. Typically, the displacements were applied incrementally to allow simultaneous estimation of the unstable stacking fault energy. Thereafter, the energy of the system was minimized using FIRE. The atoms were constrained to move along the z direction only by setting the x - and y -components of their force vectors to zero.

Appendix A. Appendix

A.1.2 Random Alloys

The configuration for calculating the random alloy lattice parameter was a $30 \times 30 \times 30$ FCC unit cells large cube, which was prepared using the lattice parameter of the corresponding average alloy. The atom types were replaced randomly by the corresponding true atom types according to the desired concentrations. Three realizations were prepared for each concentration. To determine the mean lattice lattice parameter of the random alloy, the pressure was relaxed independently along x , y and z using the LAMMPS command fix boxrelax in conjunction with CG minimization. The mean lattice parameter is then the mean edge length of the cube divided by 30. The pressure tolerance was 0.5 bar. However, this threshold could not always be reached. In the case of Al-Mg alloys, the largest residual pressure was 10.4 bar, in one calculation with Al+18 at.% Mg. At all other concentration levels, the mean absolute residual pressure of the three corresponding calculations was less than 1.6 bar. In the case of Ni-Al and Cu-Ni, the mean absolute pressure was less than 3.3 bar and 0.5 bar, respectively.

The configurations from the lattice parameter calculations were also used for determining C_{11} , C_{12} and C_{44} . This was done by imposing a strain and measuring the resulting stress, following the description in [89]. For C_{11} and C_{12} , a uniaxial strain was applied along y . Switching from Voigt to tensor notation, the response is

$$\begin{aligned}\sigma_{22} &= C_{2222}\varepsilon_{22}, \\ \sigma_{11} &= C_{1122}\varepsilon_{22}, \\ \sigma_{33} &= C_{2233}\varepsilon_{22}.\end{aligned}\tag{A.1}$$

Simulations were performed for six strain levels, compressive as well as tensile. The absolute values of strain were $|\varepsilon_{22}| = 1 \times 10^{-5}, 5 \times 10^{-5}, 1 \times 10^{-4}$. After deforming the configuration, the energy of the system was minimized using FIRE. The elastic constants in Eq. A.1 were determined by linearly fitting the stress-strain data. C_{12} was taken as the mean value of C_{1122} and C_{2233} . To determine C_{44} , a simple shear γ_{12} was applied, which causes a stress

$$\sigma_{12} = C_{1212}\varepsilon_{12}.\tag{A.2}$$

Positive and negative shears were applied, with $|\gamma_{12}| = 1 \times 10^{-5}, 5 \times 10^{-5}, 1 \times 10^{-4}$. The minimization that was performed in both types of calculations after each strain increment was stopped when the two-norm of the force vector fell below $1 \times 10^{-6} \text{ eV } \text{\AA}^{-1}$. However, in the case of Al-Mg a rather high tolerance of $2 \times 10^{-3} \text{ eV } \text{\AA}^{-1}$ was used, hence the corresponding results are more uncertain. Note that random alloy elastic constants where not used in any of the calculations in Ch. 3 and Ch. 4. They are calculated here in order to be able to estimate the error of the average-alloy approximation.

The splitting width d was determined using (DXA), like in the average alloys. The values listed in the tables above are the mean values of the different true random alloy realizations with the corresponding concentration.

Finally, γ_{SF} was calculated like in the case of the average alloys. The configuration was constructed using the corresponding A-atom lattice parameter. Before relaxation of the pressure in x and y , the configuration was converted into a true random alloy by assigning a

random distribution of real atom types according to the desired composition. In the case of Al-Mg, the force tolerance was increased to 1×10^{-4} eV Å⁻¹, due to the convergence problems discussed in Sec. 2.3.1.

A.2 Nudged Elastic Band Method

In the Nudged Elastic Band (NEB) [59, 81] method, the $3N$ -dimensional force vector \mathbf{F}_i acting on image i is calculated as the sum of components \mathbf{F}_i^{\parallel} and \mathbf{F}_i^{\perp} parallel and perpendicular to the transition path, respectively. \mathbf{F}_i^{\parallel} enforces that the images maintain a particular spacing. \mathbf{F}_i^{\perp} is the force derived from the potential energy minus the component parallel to the path. The formulas for the three forces are

$$\begin{aligned}\mathbf{F}_i &= \mathbf{F}_i^{\perp} + \mathbf{F}_i^{\parallel}, \\ \mathbf{F}_i^{\parallel} &= (|\mathbf{R}_{i+1} - \mathbf{R}_i|k_i - |\mathbf{R}_i - \mathbf{R}_{i-1}|k_{i-1})\hat{\tau}_i, \\ \mathbf{F}_i^{\perp} &= -\nabla V(\mathbf{R}_i) + [\nabla V(\mathbf{R}_i) \cdot \hat{\tau}_i]\hat{\tau}_i,\end{aligned}\tag{A.3}$$

where $|\dots|$ indicates the vector norm, \mathbf{R}_i is the $3N$ -dimensional vector of atomic positions, k_i is a constant, $\nabla V(\mathbf{R}_i)$ is the gradient of the potential energy, and τ_i is the tangent to the path in $3N$ -dimension space. The hat indicates that it is normalized i.e. $\hat{\tau}_i = \tau_i / |\tau_i|$. Note that \mathbf{F}_i^{\perp} goes to zero if the images lie on the path. \mathbf{F}_i^{\parallel} goes to zero if the images achieve a specific spacing, which depends on the constants k_i . If a single constant k is used, i.e. $k_i = k \forall i$, then equidistant spacing of the images is enforced.

LAMMPS implements the so-called improved tangent estimate [47], where τ_i is either the forward difference $\hat{\tau}_i^+ = \mathbf{R}_{i+1} - \mathbf{R}_i$, the backward difference $\hat{\tau}_i^- = \mathbf{R}_i - \mathbf{R}_{i-1}$, or a mixture thereof, depending on the energies V_i ,

$$\tau_i = \begin{cases} \hat{\tau}_i^+ & V_{i+1} > V_i > V_{i-1} \\ \hat{\tau}_i^- & V_{i-1} > V_i > V_{i+1} \\ \hat{\tau}_i^+ \Delta V_i^{\max} + \hat{\tau}_i^- \Delta V_i^{\min} & V_i > V_{i+1} > V_{i-1} \vee V_{i+1} > V_{i-1} > V_i \\ \hat{\tau}_i^+ \Delta V_i^{\min} + \hat{\tau}_i^- \Delta V_i^{\max} & V_i > V_{i-1} > V_{i+1} \vee V_{i-1} > V_{i+1} > V_i \end{cases},\tag{A.4}$$

where

$$\begin{aligned}V_i^{\max} &= \max(|V_{i+1} - V_i|, |V_{i-1} - V_i|), \\ V_i^{\min} &= \min(|V_{i+1} - V_i|, |V_{i-1} - V_i|).\end{aligned}\tag{A.5}$$

A.3 Convergence in String Method Calculations

In the String method the minimum energy path between initial and final state is determined iteratively. Ideally, the calculation converges to a unique path with vanishing perpendicular forces. That is, for each image i , the $3N$ -dimensional vector \mathbf{F}_i of atomic forces is parallel to the path. In practice, the calculation may end before this state is reached. Recall that the calculations in Ch. 3 and Ch. 4 were stopped when the Euclidean norm of the maximum displacement of any image fell below 10^{-3} Å, or after 300 or 600 String iterations. In the following, we check whether the calculations are converged by examining the change of

Appendix A. Appendix

energy during String iterations and the residual perpendicular forces. Finally, we check how much the results depend on the calculation method.

Fig. A.2 shows the relative change of activation energy ΔE_{act} per outer iteration¹ in calculations with Al+22 at.% Mg from Ch. 4. Towards the end of each calculation, ΔE_{act} changes only by fractions of a percent. In one case, a change of 0.5% occurs in the last iteration. In all other String method calculations reported in Ch. 4, the change in the last iteration is smaller than this value. Hence, it seems unlikely that continuing the String calculation for many more iterations would yield a substantially different result.

Next, we examine the residual perpendicular forces. The perpendicular force of image i is

$$\mathbf{F}_i^\perp = \mathbf{F}_i - [\mathbf{F}_i \cdot \hat{\tau}_i] \hat{\tau}_i, \quad (\text{A.6})$$

where $\hat{\tau}_i$ is the tangent to the path at the position of image i in $3N$ -dimensional space. We use the following tangent definition, which is similar to the “improved” tangent definition [47] that is frequently used in NEB calculations, see Sec. A.2,

$$\tau_i = \begin{cases} \hat{\tau}_i^+ & V_{i+1} > V_i > V_{i-1} \\ \hat{\tau}_i^- & V_{i-1} > V_i > V_{i+1} \\ \hat{\tau}_i^+ + \hat{\tau}_i^- & V_i > V_{i+1} > V_{i-1} \vee V_{i+1} > V_{i-1} > V_i \\ \hat{\tau}_i^+ + \hat{\tau}_i^- & V_i > V_{i-1} > V_{i+1} \vee V_{i-1} > V_{i+1} > V_i \end{cases}. \quad (\text{A.7})$$

Fig. A.3 shows the distributions of the Euclidean norm of \mathbf{F}_i^\perp from the calculations reported in Ch. 4. Note that the forces of the first and the last image were excluded because they correspond to local minima with close to zero total force. The median norm is lower than 10^{-2} eV/Å, both in calculations with average and random alloys. The norm tends to be lower in average alloy calculations compared to random alloy calculations, which is perhaps not surprising, considering the smoother potential energy landscape of the homogeneous average alloy systems. The maximum values are on the order of 10^{-1} eV/Å. These values are magnitudes higher than the norm of the residual force that one would commonly tolerate in regular energy minimizations (10^{-6} – 10^{-6} eV/Å). However, such large values mainly occur in the region of constriction formation and annihilation, see Fig. A.4, where the norm is drawn as a function of reaction coordinate for two average alloys. The residual forces are much lower at the transition state, where the activation energy is measured.

Additionally, NEB calculations were carried out to check how much the results depend on the algorithm for finding minimum energy paths. The Ni+15 at.% Al random alloy configurations from Ch. 3 were used as test cases. Two sets of NEB calculations were performed. In the first case, the default initial guess for the path, i.e. a linear interpolation between initial and final state, was used in the calculations. In the second case, the output paths from the corresponding String calculations were used as input. Fig. A.5 shows the differences between the activation energies calculated with NEB and String method. They are typically less than 1×10^{-2} eV Å⁻¹. In a few cases, the difference is on the order of 0.1 eV. It tends to be smaller when the output of the String calculation is used as initial guess. The maximum difference is 0.17 eV, in a calculation with Ni+12 at.% Al. Here, cross-slip nucleates at a different position

1. i.e. iterations on which the String was reparameterized

A.3. Convergence in String Method Calculations

along the line. Nevertheless, the transition paths are similar, see Fig. A.6a). Significantly different transition paths are obtained in one calculation for Ni+15 at.% Al, see Fig. A.6b). Here, the NEB calculation predicts a path with more local minima. However, closer inspection reveals that the initial part of the path corresponds to a failed cross-slip attempt, where a nucleus is formed and disappears again. The second part of the path is qualitatively similar to the paths obtained with the String method or the NEB method with String input. In particular, the transition state in this section of the path is very similar to the transition states in the other calculations. These observations demonstrate that our calculations are robust against a change of method. Furthermore, they indicate that continuing the String calculations until all $|F_i^\perp|$ ($i = 1 \dots N_S$) are below 10^{-2} eV/Å would have little effect.

We conclude that the calculated paths are not fully converged minimum energy paths. However, they are sufficiently well converged for our purposes. Continuing the calculations is unlikely to lead to significantly different values of ΔE_{act} . The expected changes are very small compared to the overall level of ΔE_{act} and random fluctuations of ΔE_{act} in random alloys. Furthermore, we have demonstrated that our results are robust against a change of calculation method.

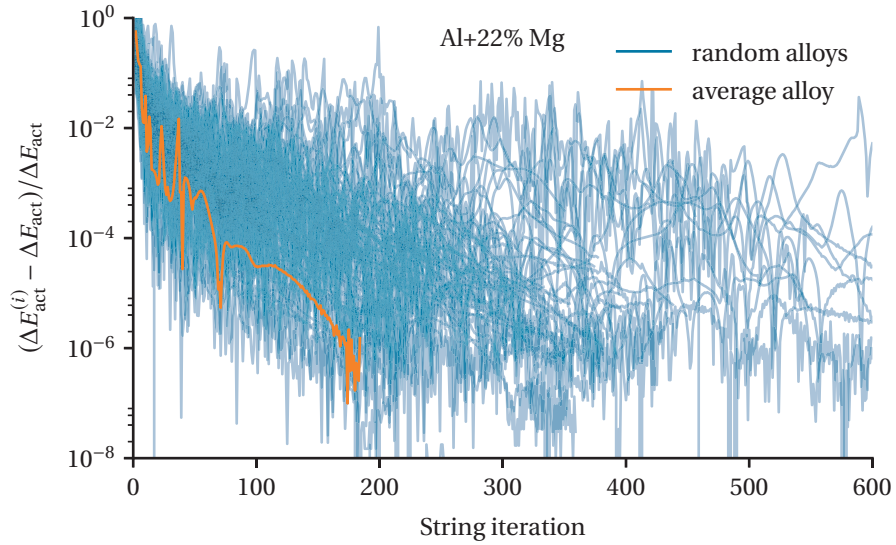


Figure A.2: Change of activation energy $\Delta E_{\text{act}}^{(i)}$ as a function of String iteration i , relative to the final value ΔE_{act} ; data from calculations with Al+22 at.% Mg reported in Ch. 4; note that some calculations terminated due to reaching the maximum number of 600 String iterations; in random Al+22 at.% Mg, a change of 0.5% in the last iteration is seen in one case; this is the maximum final value across all alloy datasets

Appendix A. Appendix

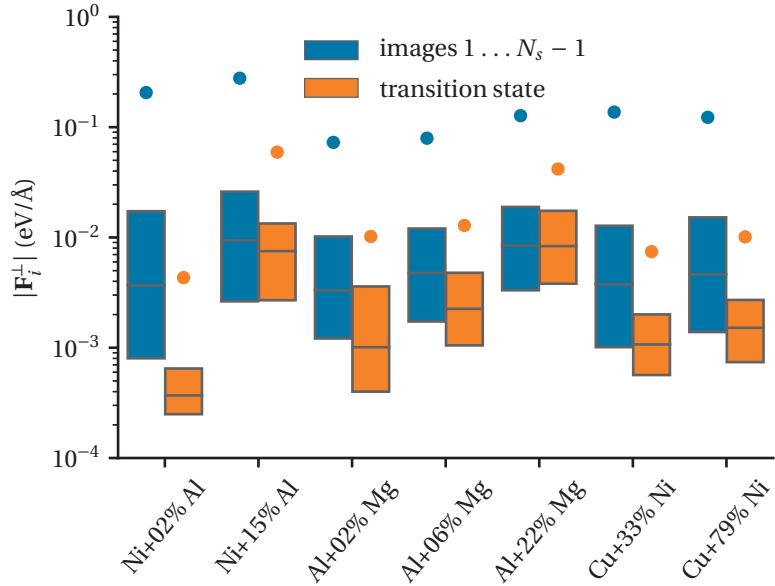


Figure A.3: Distributions of the magnitudes of the force vectors \mathbf{F}_i^\perp ; the magnitude is a measure of convergence, since \mathbf{F}_i^\perp is zero for images lying on the MEP; data for random alloys from calculations reported in Ch. 4; blue: distribution for all images except the initial and final one, which correspond to local minima ($3000 = 100 \times 30$ data points per alloy); orange: magnitude of $\mathbf{F}_{i_{\max}}^\perp$ at the transition state ($i = i_{\max}$); 100 values per alloy; the upper and lower edge of each box represent the third and second quartile of the data, i.e. 50% of all values lie in this range; the horizontal line indicates the median; points indicate maximum values;

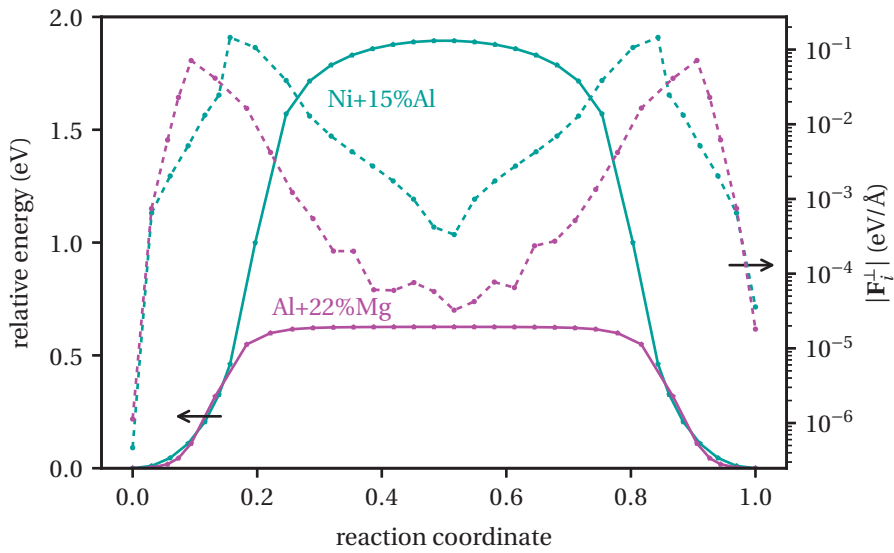


Figure A.4: Relative energy (solid lines, left y-axis) and magnitude of \mathbf{F}^\perp (dashed lines, right y-axis) as a function of reaction coordinate; data from calculations with average alloys of Ni+15 at.% Al (teal) and Al+22 at.% Mg (magenta); high perpendicular forces are seen in the region of constriction formation; data from calculations reported in Ch. 4

A.3. Convergence in String Method Calculations

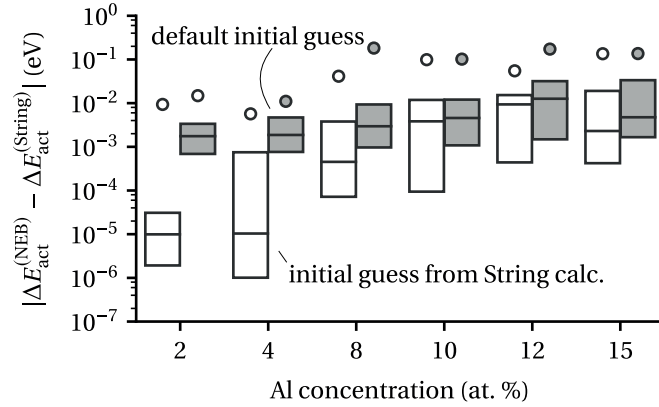


Figure A.5: Magnitude of difference between Nudged Elastic Band (NEB) and String method estimates of ΔE_{act} ; gray and white indicate the initial guess used in the NEB calculation; white: using the same initial guess as in the String method calculation; gray: *output* of String method calculation used as initial guess; the upper and lower edge of each box represent the third and second quartile of the data, i.e. 50% of all values lie in this range; the horizontal line indicates the median; points indicate maximum values; String method data from calculations with Ni-Al alloys reported in Ch. 3; 20 String method calculations were performed for each concentration; however, some NEB calculations with Ni+12 at.% Al and Ni+15 at.% Al diverged; thus the sample size of gray and white datasets is 16 and 19 at 12% Al, and 16 and 17 at 15% Al

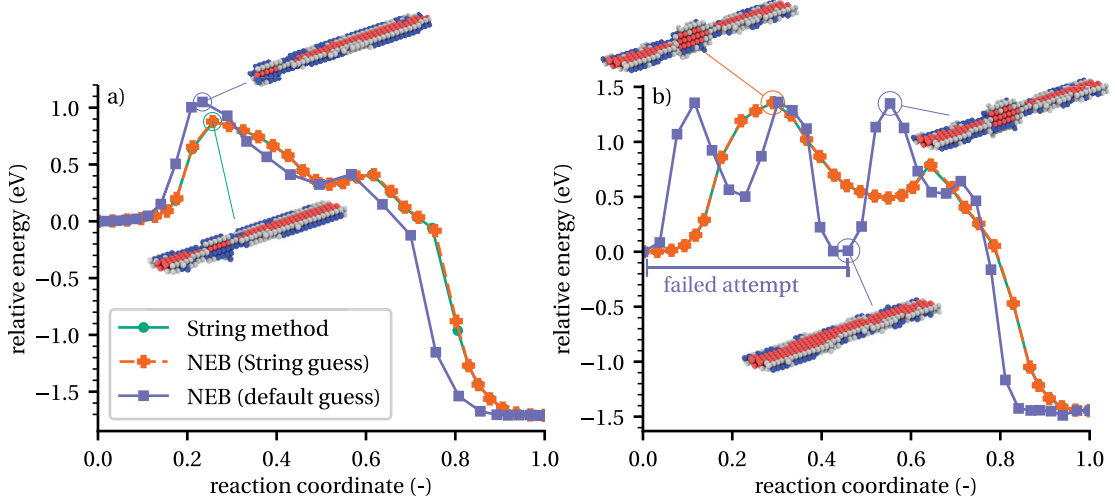


Figure A.6: Transition paths from String and NEB calculations; orange: output of String calculation used as initial guess for NEB calculation; violet: default initial guess; note that the NEB/String paths overlap with the String paths; two extreme cases are shown: a) paths from calculations with a particular Ni+12 at.% Al random alloy realization; here, the difference in ΔE_{act} between NEB/default and String calculations is larger than in other calculations with Ni-Al random alloys; cross-slip nucleates at a different position in the NEB calculation; nevertheless, the paths are qualitatively similar; b) significant qualitative difference between NEB/default and String paths in a calculation with Ni+15 at.% Al; the initial part of the NEB path represents a failed cross-slip attempt, where a nucleus is formed and disappears; the subsequent portion of the path is qualitatively similar to String and NEB/String paths.

A.4 System Size Dependence of ΔE_{act} in Atomistic Calculations

The atomic configurations used in cross-slip transition path calculations must be large enough to minimize boundary effects. Two dimensions have to be taken into account, the inner radius of the cylinder and its length along the periodic direction. If the radius is too small, the width of the dislocation may be far from the value in an infinite medium, due to interactions with the fixed shell. If the cylinder is too short, self-interaction of the two constrictions across the periodic boundary may influence ΔE_{act} .

To determine the required system size, transition path calculations were performed for different radii and periodic lengths. The simulations were carried out with pure Ni, using the potential of Ref. [98]. Preliminary calculations showed that ΔE_{act} of this material is comparable to ΔE_{act} of Cu and Ni as given by the potential of Ref. [91], and higher than ΔE_{act} of Al as given by the potential of Ref. [74]. Thus, it was assumed that the dimensions found here would also be sufficient for the other materials.

The radius was varied between 8 and $22b$. 16 images were used in the calculation. Fig. A.7a) and b) show the transition paths and the corresponding activation energies, respectively. ΔE_{act} decreases with increasing radius. However, at $12b$ and larger, the difference with respect to the value at $22b$ is less than 0.1 eV. In practice, a radius of $10\sqrt{3}a$ was used, which is slightly larger than the largest radius tested here. ΔE_{act} at $10\sqrt{3}a$ is 1.724 eV, and thus only 0.005 eV smaller than the value at $22b$.

To study the effect of length, transition path calculations were carried out with $5b$ to $160b$ long configurations. Two sets of calculations were carried out. In the case, the length was varied between $5b$ and $60b$, but the number of images was kept constant at 16. In a second set, 30– $160b$ long dislocations were simulated and the number of images was increased with increasing length, in order to avoid loss of resolution of the path. The resulting transition paths and activation energies are shown in Fig. A.8a) and b), respectively. ΔE_{act} increases with length until it reaches a value of roughly 1.7 eV. At the largest length of $160b$, cross-slip nucleates at two positions along the dislocation line when using the standard initial guess for the path. Thus, the transition path is a combination of two regular cross-slip transition paths and the activation energy is approximately twice the value for a single nucleus. However, if the calculation is started with an improved initial guess for the path, see Sec. 2.3.3, then a regular cross-slip transition path is obtained. For lengths shorter than $15b$, the dislocation does not cross-slip by the Friedel-Escaig mechanism. Instead of forming point constrictions, it constricts over the full length before changing slip plane. The length at which ΔE_{act} becomes independent of length is approximately $40b$. Between $40b$ and $160b$, ΔE_{act} increases by less than 0.03 eV. Thus, a length of $40b$ was used in the calculations reported in Ch. 3 and Ch. 4.

In calculations at nonzero Escaig stress on the cross-slip plane, a larger configuration may be required to compensate for widening of the dislocation. A more limited parameter test was carried out to determine the required inner radius of the configuration. Transition path calculations were performed with average Ni+15 at.% Al at 300 MPa stress. The radius was varied in the range $10\sqrt{3}a$ – $17.5\sqrt{3}a$. ΔE_{act} increases slightly with radius, see Fig. A.9. Between $12.5\sqrt{a}$ and $17.5\sqrt{a}$, the increase is only 0.01 eV, hence a radius of $13\sqrt{3}a$ was used in practice.

A.4. System Size Dependence of ΔE_{act} in Atomistic Calculations

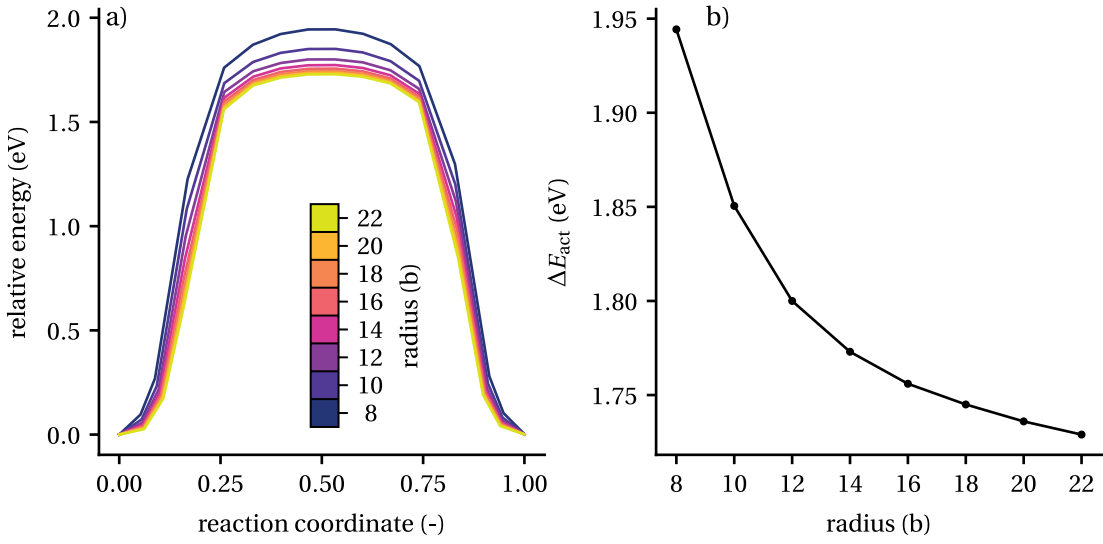


Figure A.7: Cross-slip transition path data for pure Ni as a function of the inner radius of the cylindrical atomistic configuration; a) transition paths for different radii; b) activation energy as a function of radius; 16 images were used in the calculations

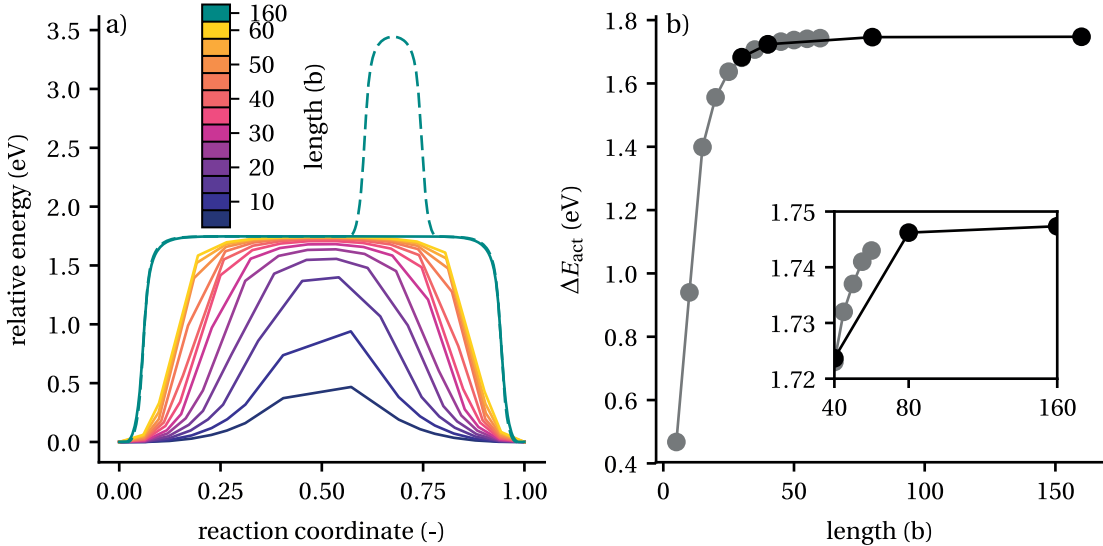


Figure A.8: Cross-slip transition path data for pure Ni as a function of the periodic length of the atomistic configuration; a) transition paths for different lengths; green lines: transition paths for a 160 b long configuration; dashed line: result from a calculation using the default initial guess for the path (interpolation between initial and final state); two cross-slip nuclei are formed here; solid line: result from a calculation with an improved initial guess; the number of images was 16 in calculations with 5–60 b length and 256 in calculations with 160 b length; b) activation energy as a function of length; the data point from the calculation with 160 b length and two nuclei is not shown; gray line: calculations with length 5–60 b and 16 images; black line: calculations for 30 b , 40 b , 80 b and 160 b length; the number of images was 48, 64, 128 and 256; inset: zoom on the range 40 b –160 b

Appendix A. Appendix

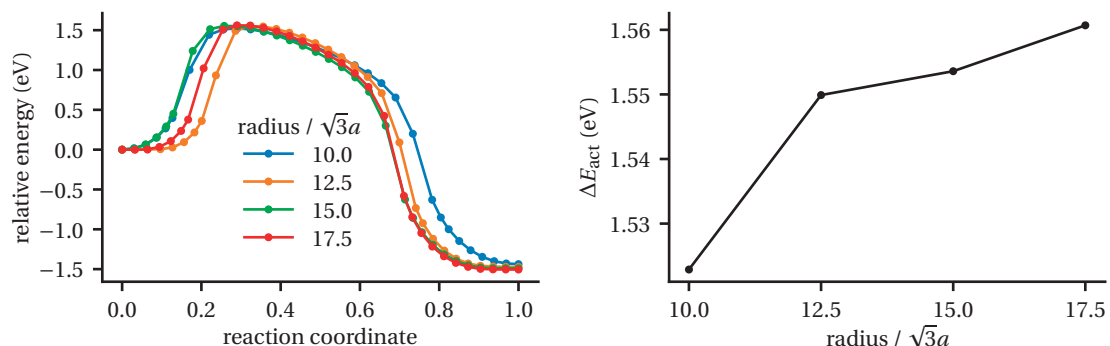


Figure A.9: Influence of the inner radius of the configuration at finite stress; a) transition paths and b) activation energies of Ni+15 at.% Al at 300 MPa Escaig stress

A.5 Partially Cross-Slipped Dislocations

The large fluctuations in solute binding energies raise an interesting possibility. Should we expect to observe partially cross-slipped dislocations in equilibrium? Consider the dislocation

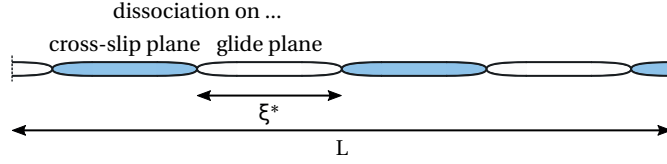


Figure A.10: Partially cross-slipped dislocation

of total length L shown in Fig. A.10. Some segments are dissociated on the cross-slip plane, others on the glide plane. Random fluctuations in solute-dislocation and solute-solute binding energies are unbiased and may promote dissociation on either plane. Thus, we should expect that about half of the segments are dissociated on the cross-slip plane. To find the equilibrium segment length ζ^* , we minimize the relative energy of the partially cross-slipped configuration (relative to that of a dislocation lying fully on the glide plane). For each segment on the cross-slip plane, the energy increases by the energy of two isolated constrictions, which is approximately equal to $\Delta E_{\text{act,avg}}$. On the other hand, a segment will only cross-slip if there are favorable solute fluctuations that promote dissociation on the cross-slip plane. The energy gained by cross-slip is typically one standard deviation of ΔE_{end} , which grows with the square root of the segment length ζ , hence

$$\begin{aligned}\Delta E &= -\frac{L}{2\zeta} \sigma [\Delta E_{\text{end}}] |_{\zeta=1b} \sqrt{\frac{\zeta}{b}} + \frac{L}{2\zeta} \Delta E_{\text{act,avg}}, \\ \frac{\Delta E}{L} &= -\frac{1}{2\sqrt{b\zeta}} \sigma [\Delta E_{\text{end}}] |_{\zeta=1b} + \frac{1}{2\zeta} \Delta E_{\text{act,avg}},\end{aligned}\tag{A.8}$$

where $\sigma [\Delta E_{\text{end}}] |_{\zeta=1b}$ is the standard deviation of ΔE_{end} for a $1b$ long segment. The length ζ^* for which ΔE is minimum can easily be found by requiring $\partial(E/L)/\partial\zeta = 0$. The result is

$$\zeta^* = 4b \left(\Delta E_{\text{act,avg}} / \sigma [\Delta E_{\text{end}}] |_{\zeta=1b} \right)^2.\tag{A.9}$$

Using the extended model for $\sigma [\Delta E_{\text{end}}]$ that was presented in Sec. 4.1, we find that ζ^* is in the range $202b$ to $11264b$ for the alloys considered here, see Tab. A.4. At dislocation densities of 10^{12} to 10^{13} m^{-2} , typical values for L are on the order of $10^3 b$. Thus, it seems that partially cross-slipped states could be observed in extreme cases with low values of $\Delta E_{\text{act,avg}} / \sigma [\Delta E_{\text{end}}] |_{\zeta=1b}$.

Appendix A. Appendix

Table A.4: Equilibrium segment length ζ^* of partially cross-slipped dislocations according to Eq. A.9.

alloy	ζ^*/b
Ni+02%Al	11264
Ni+15%Al	402
Al+02%Mg	2112
Al+06%Mg	659
Al+22%Mg	202
Cu+22%Ni	4847
Cu+33%Ni	2843
Cu+79%Ni	3102

A.6 Extended Solute Pair Model

Our goal is to calculate the standard deviation of the change in solute-solute binding energies due to formation and destruction of solute pairs in the stacking fault ribbon during cross-slip. The corresponding model from Sec. 3.4.3 can be improved by taking into account higher order neighbor pairs and correlation between pair changes. For this purpose, we write the change $\Delta E_{\text{end,s-s,sf},XY}$ in solute-solute binding energy during stacking fault formation in a very general form. Recall that a stacking fault consists of two $\{111\}$ planes with hexagonal-closed packed coordination. In our derivation, we take atoms below the fault, including those in the lower plane of the fault, as fixed. The stacking fault is generated by displacing the atoms above, including those in the upper plane of the fault, by the Burgers vector of a Shockley partial dislocation. Consider a unit cell in the lower region, as shown in Fig. A.11. The upper plane of the cell (green atoms) corresponds to the lower plane of the fault. The fault can be created by displacing the atoms above by $a/6[\bar{1}12]^2$. For a stacking fault of length ζ and width d , there are $N_\zeta \times N_d$ such cells, where $N_\zeta = \zeta/b$ and $N_d = d/b/\sqrt{3}$. To get the total change in solute-solute binding energy, we need to sum contributions from all atomic sites in these cells. Even lower planes do not need to be considered if we restrict ourselves to eight nearest neighbor pairs. The corresponding neighbor distances are listed in Tab. 4.1.

Label the unit cells with indices ij , where $i = 1 \dots N_\zeta$ and $j = 1 \dots N_d$. Let $\Omega_{lo,ij}$ be the set of sites in the unit cell ij . There are three or five sites in each $\{111\}$ plane of the unit cell. Some however, lie on a face or in a corner of the cell and are therefore shared with neighboring unit cells. There are only two full sites per plane and eight per unit cell. To generate $\Omega_{lo,ij}$, one could either associate eight sites with each cell in a consistent way, or take all sites and introduce extra occupation variables or weighting factors to account for the fact that some sites are associated with multiple unit cells. We choose the latter method, because it allows to take into account more correlations between pair changes within each unit cell. Furthermore, let Ω_{hi} be the set of sites above the fault, including the upper plane of the fault. Assign occupation variables $s_{X,ijk}$, where $s_{X,ijk} = 1$ if there is a X -solute at site ijk , and $s_{X,ijk} = 0$ otherwise. The

2. Slightly different results would be obtained with a displacement $a/6[\bar{1}2\bar{1}]$, i.e. parallel to x . The directions $[\bar{1}\bar{1}2]$ and $[\bar{1}2\bar{1}]$ are not equivalent in our model. As we shall see, we consider only neighbor changes for sites in a single unit cell as shown in Fig. A.11. With this particular choice of sites, the threefold rotation symmetry in the $\{111\}$ plane (the plane of the paper) is lost, hence $[\bar{1}\bar{1}2]$ and $[\bar{1}2\bar{1}]$ are not equivalent. However, $a/6[\bar{1}12]$ is the correct displacement corresponding to a Shockley partial of a $1/2a[10\bar{1}]$ screw dislocation.

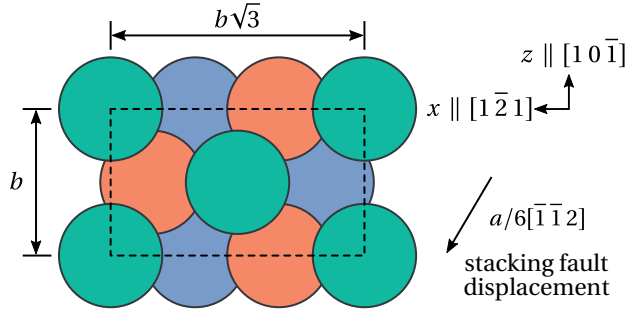


Figure A.11: Unit cell used in the derivation of the change in the number of solute pairs during formation of an intrinsic stacking fault; the cell is below the fault and seen from above. Green atoms represent the lower plane of the fault. Atoms in the upper plane of the fault would be on top of the blue atoms before formation of the fault. To form the fault, all atoms above the green atoms are displaced by $a/6[\bar{1}\bar{1}2]$.

$s_{X,ijk}$ are Bernoulli random variables with probability and expectation value equal to the concentration c_X of type X .

The total change in solute-solute binding energies for pairs formed by X -atoms in $\Omega_{lo,ij}$ and Y -atoms in Ω_{hi} is the sum of contributions from all unit cells, i.e.

$$\Delta E_{\text{end,s-s,sf},XY} = \sum_i^{N_\zeta} \sum_j^{N_d} \Delta E_{\text{end,s-s,sf},XY,ij}. \quad (\text{A.10})$$

To calculate $\Delta E_{\text{end,s-s,XY},ij}$, one sums the changes in solute-solute binding energies for each site in $\Omega_{lo,ij}$. Accounting for pairs up to order N_{\max} ,

$$\Delta E_{\text{end,s-s,sf},XY,ij} = \sum_{k \in \Omega_{lo,ij}} s_{X,ijk} w_k \sum_l^{N_{\max}} U_{s-s,XY,l} \sum_{m \in \Omega_{hi}} s_{Y,ijm} \Delta(i, j, k, m, l), \quad (\text{A.11})$$

where $U_{s-s,XY,l}$ is the binding energy of an l -th nearest neighbor XY pair. The w_k are extra occupation variables, which account for the fact that face and corner sites are shared by multiple unit cells, hence we would have associated only one face or corner site in each plane and unit cell with this cell. They are Bernoulli random variables with probability 1 for sites completely inside the cell, 1/2 for face sites, and 1/4 for corner sites. $\Delta(i, j, k, m, l)$ indicates if a l -th order neighbor pair is formed, lost, or preserved, i.e.

$$\Delta(i, j, k, m, l) = [a(i, j, k, m, l) - b(i, j, k, m, l)], \quad (\text{A.12})$$

where $b(i, j, k, m, l) = 1$ if the sites are l -th nearest neighbors before formation of the fault, and zero otherwise; and $a(i, j, k, m, l) = 1$ if they are l -th nearest neighbors after formation of the fault, and zero otherwise.

The variance of $\Delta E_{\text{end,s-s,sf},XY}$ is

$$\text{Var} [\Delta E_{\text{end,s-s,sf},XY}] = \langle \Delta E_{\text{end,s-s,sf},XY}^2 \rangle - (\langle \Delta E_{\text{end,s-s,sf},XY} \rangle)^2, \quad (\text{A.13})$$

Appendix A. Appendix

where $\langle \dots \rangle$ indicates the average with respect to $s_{X,ijk}$ and $s_{Y,ijk}$. However, a direct calculation would be intractable due to the large number of terms involved. We simplify the problem by making $\Delta(i, j, k, m, l)$ independent of i and j . Neighbor changes are analyzed only once, for all atoms in the unit cell shown in Fig. A.11, i.e.

$$\Delta(i, j, k, m, l) \equiv \Delta^c(k, m, l) = [a^c(k, m, l) - b^c(k, m, l)], \quad (\text{A.14})$$

where a superscript c is used to refer to the reference cell. Thus, we consider only subsets $\Omega_{lo}^c \subset \Omega_{lo,ij}$ and $\Omega_{hi}^c \subset \Omega_{hi}$. By using $\Delta^c(k, m, l)$ instead of $\Delta(i, j, k, m, l)$ we still capture some correlations. For example, we account for exchange of neighbor sites between the sites in the reference unit cell. However, we ignore exchanges between sites in different unit cells with different i and j . The numbers $\Delta^c(k, m, l)$ were determined by finding the neighbors of sites in a unit cell as shown in Fig. A.11 before and after insertion of the fault. The crystals were generated with LAMMPS and the distance-based selection could be done conveniently using OVITO [135].

We can now write for the second term in Eq. A.13, noting that $s_{X,ijk}$ and $s_{Y,ijm}$ are independent in a random solid solution,

$$\begin{aligned} (\langle \Delta E_{\text{end,s-s,sf},XY} \rangle)^2 &= \left[\sum_i^{N_\zeta} \sum_j^{N_d} \langle \Delta E_{\text{end,s-s,sf},XY,ij} \rangle \right]^2 \\ &= \left[\sum_i^{N_\zeta} \sum_j^{N_d} \sum_{k \in \Omega_{lo}^c} \langle s_{X,ijk} \rangle w_k \sum_l^{N_{\max}} U_{\text{s-s},XY,l} \sum_{l \in \Omega_{hi}^c} \langle s_{Y,ijm} \rangle \Delta^c(k, m, l) \right]^2 \\ &= \left[N_\zeta N_d c_X c_Y \sum_{k \in \Omega_{lo}^c} w_k \sum_l^{N_{\max}} U_{\text{s-s},XY,l} \sum_{l \in \Omega_{hi}^c} \Delta^c(k, m, l) \right]^2 \end{aligned} \quad (\text{A.15})$$

Define

$$\beta(\{w_k\}) \equiv \sum_{k \in \Omega_{lo}^c} w_k \sum_l^{N_{\max}} U_{\text{s-s},XY,l} \sum_{l \in \Omega_{hi}^c} \Delta^c(k, m, l), \quad (\text{A.16})$$

then

$$\left(\langle \Delta N_{\text{s-s,sf}}^{\text{loss}} \rangle \right)^2 = (N_\zeta N_d c_X c_Y \beta(\{w_k\}))^2. \quad (\text{A.17})$$

The first term in Eq. A.13 involves the square of a sum and can be expanded as follows. For the sake of brevity we write $\alpha_{ij} \equiv \Delta E_{\text{end,s-s,sf},XY,ij}$. Thus

$$\begin{aligned} \langle \Delta E_{\text{end,s-s,sf},XY}^2 \rangle &= \left\langle \left[\sum_i^{N_\zeta} \sum_j^{N_d} \alpha_{ij} \right]^2 \right\rangle \\ &= \left\langle \sum_i^{N_\zeta} \sum_j^{N_d} \alpha_{ij}^2 \right\rangle + \left\langle \sum_i^{N_\zeta} \sum_{p \neq i}^{N_\zeta} \sum_j^{N_d} \sum_{q \neq j}^{N_d} \alpha_{ij} \alpha_{pq} \right\rangle \\ &\quad + \left\langle \sum_i^{N_\zeta} \sum_{p \neq i}^{N_\zeta} \sum_j^{N_d} \alpha_{ij} \alpha_{pj} \right\rangle + \left\langle \sum_i^{N_\zeta} \sum_j^{N_d} \sum_{q \neq j}^{N_d} \alpha_{ij} \alpha_{iq} \right\rangle. \end{aligned} \quad (\text{A.18})$$

The variables α_{ij} , α_{pq} , α_{pj} and α_{iq} are independent, hence

$$\begin{aligned} \langle \Delta E_{\text{end,s-s,sf},XY}^2 \rangle &= \sum_i^{N_\zeta} \sum_j^{N_d} \langle \alpha_{ij}^2 \rangle + \sum_i^{N_\zeta} \sum_{p \neq i}^{N_\zeta} \sum_j^{N_d} \sum_{q \neq j}^{N_d} \langle \alpha_{ij} \rangle \langle \alpha_{pq} \rangle \\ &\quad + \sum_i^{N_\zeta} \sum_{p \neq i}^{N_\zeta} \sum_j^{N_d} \langle \alpha_{ij} \rangle \langle \alpha_{pj} \rangle + \sum_i^{N_\zeta} \sum_j^{N_d} \sum_{q \neq j}^{N_d} \langle \alpha_{ij} \rangle \langle \alpha_{iq} \rangle. \end{aligned} \quad (\text{A.19})$$

For the last three terms, one obtains

$$\begin{aligned} \sum_i^{N_\zeta} \sum_{p \neq i}^{N_\zeta} \sum_j^{N_d} \sum_{q \neq j}^{N_d} \langle \alpha_{ij} \rangle \langle \alpha_{pq} \rangle &= N_\zeta (N_\zeta - 1) N_d (N_d - 1) (c_X c_Y \beta(\{w_k\}))^2, \\ \sum_i^{N_\zeta} \sum_{p \neq i}^{N_\zeta} \sum_j^{N_d} \langle \alpha_{ij} \rangle \langle \alpha_{pj} \rangle &= N_\zeta N_d (N_\zeta - 1) (c_X c_Y \beta(\{w_k\}))^2, \\ \sum_i^{N_\zeta} \sum_j^{N_d} \sum_{q \neq j}^{N_d} \langle \alpha_{ij} \rangle \langle \alpha_{iq} \rangle &= N_\zeta N_d (N_d - 1) (c_X c_Y \beta(\{w_k\}))^2. \end{aligned} \quad (\text{A.20})$$

The first term in Eq. A.19 is more cumbersome to resolve, because α_{ij}^2 is a sum of terms that may contain squares of occupation variables, e.g. $s_{X,ijk}^2 s_{Y,ijm} s_{Y,igs}$. Since the occupation variables are Bernoulli random variables, the averages of their squares are the same as the averages of the variables themselves, i.e. c_X and c_Y . Each such product contains at least two independent variables, thus the averaged products have the form $c_X^\nu c_Y^w$ with $\nu + w \in [2, 3, 4]$. The correct products of concentrations can be substituted for the products of occupation variables using a computer algebra program, e.g. MATHEMATICA [155]. Corresponding MATHEMATICA code is presented in App. A.6.1.

The variance of $\Delta E_{\text{end,s-s,XY}}$, the change in solute-solute binding energies during cross-slip, is approximately two times the variance of $\Delta E_{\text{end,s-s,sf},XY}$. Combining Eq. A.13, Eq. A.20, Eq. A.19 and Eq. A.17, one obtains the preliminary result

$$\text{Var} [\Delta E_{\text{end,s-s,XY}}] = 2 \left[N_\zeta N_d (c_X c_Y \beta(\{w_k\}))^2 + \sum_i^{N_\zeta} \sum_j^{N_d} \langle \alpha_{ij}^2 \rangle \right]. \quad (\text{A.21})$$

Both terms on the right hand side still contain the extra occupation variables w_k . They must be averaged over. Recall that the w_k are Bernoulli random variables, with probabilities 1 for center sites, 1/4 for corner sites, and 1/2 for sites on the face of the unit cell. Since they are Bernoulli variables, powers of w_k are replaced by the corresponding probabilities. Again, a computer algebra program can be used to make these substitutions in Eq. A.21, see App. A.6.1. The final result for $\text{Var} [\Delta E_{\text{end,s-s,XY}}]$ is quite long. However, all terms are of the form $A U_{\text{s-s},XY,l} U_{\text{s-s},XY,m} c_X^\nu c_Y^w$, where A is an integer, $\nu, w = 1, 2$ and $l, m = 1, \dots, N_{\max}$. Thus, the variance can be written using matrix-vector notation, as in Eq. 4.1,

$$\begin{aligned} \text{Var} [\Delta E_{\text{end,s-s,XY}}] &= \frac{\zeta d}{b^2 \sqrt{3}} c_X c_Y \frac{1}{(1 + \delta_{XY})} \\ &\times \mathbf{U}_{\text{s-s},XY}^\top [\mathbf{C}_1 + \mathbf{C}_2 (c_X + c_Y) - (\mathbf{C}_1 + 2\mathbf{C}_2) c_X c_Y] \mathbf{U}_{\text{s-s},XY}, \end{aligned} \quad (4.1)$$

Appendix A. Appendix

with coefficient matrices

$$\mathbf{C}_1 = 8 \begin{pmatrix} 2 & -4 & 0 & 0 & 0 & 0 & 0 & 0 \\ 0 & 6 & -8 & 0 & 0 & 0 & 0 & 0 \\ 0 & 0 & 14 & 0 & -8 & 0 & 0 & 0 \\ 0 & 0 & 0 & 6 & 0 & 0 & 0 & 0 \\ 0 & 0 & 0 & 0 & 24 & -8 & -8 & 0 \\ 0 & 0 & 0 & 0 & 0 & 9 & 0 & 0 \\ 0 & 0 & 0 & 0 & 0 & 0 & 38 & 0 \\ 0 & 0 & 0 & 0 & 0 & 0 & 0 & 6 \end{pmatrix}, \quad (A.22)$$

$$\mathbf{C}_2 = \frac{1}{2} \begin{pmatrix} -16 & 47 & 5 & 5 & -16 & 3 & -1 & -1 \\ 0 & -62 & 86 & -12 & 37 & -16 & -14 & 2 \\ 0 & 0 & 34 & 349 & 673 & 157 & 1309 & 275 \\ 0 & 0 & 0 & 97 & 602 & 114 & 1280 & 290 \\ 0 & 0 & 0 & 0 & 426 & 231 & 2468 & 652 \\ 0 & 0 & 0 & 0 & 0 & -48 & 603 & 78 \\ 0 & 0 & 0 & 0 & 0 & 0 & 2424 & 1146 \\ 0 & 0 & 0 & 0 & 0 & 0 & 0 & 96 \end{pmatrix}.$$

If only first nearest neighbor pairs of like solutes ($X = Y$, $c = c_X = c_Y$) are considered, one obtains

$$\text{Var} [\Delta N_{\text{s-s}}] = 8c^2(1 - c) \frac{\zeta d}{b^2\sqrt{3}}, \quad (A.23)$$

which is equivalent to our previous solution for this special case, Eq. 3.16.

A.6.1 Implementation

In the following, we present Wolfram Mathematica (Version 11) [155] code for writing Eq. A.11 and substituting powers of occupation variables by concentrations.

Suppose the information about pair changes is stored in a text file `pairs.txt` with four columns and multiple rows. Each row corresponds to one pair that is lost or gained. The first column indicates the order ($l = 1 \dots N_{\max}$) of the pair, the second the sign ($-1 = \text{loss}$, $+1 = \text{gain}$), the third the unique identifier of the site in the unit cell below the fault, and the fourth the unique identifier of the site above the fault. If pairs up to the eighth order are considered, then eleven sites in the unit cell below the fault need to be taken into account. Number those sites from one to eleven and let 1, 6, and 11 be center sites with $\langle w_k \rangle = 1$ in Eq. A.21. Furthermore, let 2–5 be face sites ($\langle w_k \rangle = 1/2$), and 7–10 corner sites ($\langle w_k \rangle = 1/4$). We consider the more general case where the atoms above the fault have a different type than those in the unit cell below.

First, load the data and write the sum Eq. A.11. The pair energies are indicated by symbols E_i ($i = 1 \dots 8$). The occupation variables for sites in the unit cell are written as p_i , where i is the site number. Similarly, the occupation variables for sites above the fault are written as s_i . Symbols w_i indicate the extra occupation variables w_k in Eq. A.21.

```

1 (*Load the information and write the sum*)
2 Numbers = ReadList["pairs.txt", Table[Number, 4]];
3 Formatter[x_]:=ToExpression[
4   ToString[
5     StringForm[
6       "E``*``*p``*s``*w``", x[[1]], x[[2]], x[[3]], x[[4]], x[[3]]
7     ]
8   ]
9 ]
10 (*We could ignore pairs of higher order*)
11 (*Restrictions=*
12 E2\[Rule]0,E3\[Rule]0,E4\[Rule]0,E5\[Rule]0,
13 E6\[Rule]0,E7\[Rule]0,E8\[Rule]0
14 };*)
15 Restrictions={};
16 EnergyChange=Total[Map[Formatter,Numbers]]/.Restrictions;

```

In the following, we define a module which substitutes powers of the occupation variables p_i and s_i by the corresponding concentrations c_p and c_s , i.e. c_X and c_Y in Eq. 4.1. Furthermore, powers of w_k are replaced by the appropriate site weight. Finally, $\text{Var}[\Delta E_{\text{end},s-s,XY}]$ is derived.

```

1 (*Expression for matching powers of the symbol s *)
2 (*see https://mathematica.stackexchange.com/a/75295*)
3 MatchPowersOf=s_Symbol/;StringMatchQ[SymbolName[Unevaluated@s],#]&;
4 CalcVarianceUnlike[EnergyChange_]:=Module[
5 {
6   AverageOfSquare, SquareOfAverage,
7   AllTermsA,AllTermsB,
8   ListOfAllTermsA,ListOfAllTermsB,
9   ResultA,ResultB,
10  Uniquep,Uniques,
11  TmpList,TmpList2,TmpList3,
12  EnergyProduct,
13  Uniquews,
14  SiteWeights,
15 },
16 (*Average values of the extra occupation variables for *)
17 (*center, face and corner sites. Here: 1,6,11=center sites, *)
18 (*2-5=face sites, 7-10=corner sites*)
19 SiteWeights={1,1/2,1/2,1/2,1/2,1,1/4,1/4,1/4,1/4,1};
20 (*Calculate the average of the square of the pair change*)
21 AllTermsA=Expand[EnergyChange^2];
22 ListOfAllTermsA=List@@AllTermsA;
23 ResultA={};
24 (*Consider individual terms of the sum, which are products of*)
25 (*pair energies and mixed powers of occupation variables. *)

```

Appendix A. Appendix

```
26 (*Substitute the corresponding concentration for any power of*)
27 (*an occupation variable, since it is a Bernoulli random variable.*)
28 For[i=1,i<= Length[ListOfAllTermsA],i++,
29   TmpList=List@@ListOfAllTermsA[[i]];
30   (*Number of unique s-occupation variables*)
31   Uniques=Length[Cases[TmpList,MatchPowersOf["s*"]^_.]];
32   (*Number of unique p-occupation variables in the product*)
33   Uniquep=Length[Cases[TmpList,MatchPowersOf["p*"]^_.]];
34   (*Number of unique w-occupation variables*)
35   Uniquews={};
36   For[j=1,j<=11,j++,
37     AppendTo[
38       Uniquews,
39       Length[
40         Cases[
41           TmpList,
42           MatchPowersOf[ToString[StringForm["w` ``",j]]]^_.
43         ]
44       ]
45     ];
46   ];
47   (*Get product of pair energies by deleting occupation variables from list*)
48   TmpList2=DeleteCases[TmpList,MatchPowersOf["s*"]^_.];
49   TmpList3=DeleteCases[TmpList2,MatchPowersOf["w*"]^_.];
50   EnergyProduct=Times@@DeleteCases[TmpList3,MatchPowersOf["p*"]^_.];
51   For[j=1,j<=11,j++,
52     EnergyProduct=EnergyProduct*SiteWeights[[j]]^Uniquews[[j]];
53   ];
54   AppendTo[ResultA,
55     EnergyProduct*(
56       Nl*Nd*cp^Uniquep*cs^Uniques +
57       Nl*Nd*(Nd-1)*cp^2*cs^2 +
58       Nl*Nd*(Nl-1)*cp^2*cs^2 +
59       Nl*Nd*(Nd-1)*(Nl-1)*cp^2*cs^2
60     )
61   ];
62 ]; (*end of loop over sum terms*)
63 AverageOfSquare=Collect[FullSimplify[Total[ResultA]],cp];
64 (*Calculate the square of the average of the pair change*)
65 AllTermsB=Expand[EnergyChange];
66 ListOfAllTermsB=List@@AllTermsB;
67 ResultB={};
68 For[i=1,i<= Length[ListOfAllTermsB],i++,
69   TmpList=List@@ListOfAllTermsB[[i]];
70   Uniques=Length[Cases[TmpList,MatchPowersOf["s*"]^_.]];
71   Uniquep=Length[Cases[TmpList,MatchPowersOf["p*"]^_.]]; 
```

```

72     TmpList2=DeleteCases[TmpList,MatchPowersOf["s*"]^_.];
73     EnergyProduct=Times@@DeleteCases[TmpList2,MatchPowersOf["p*"]^_.];
74     AppendTo[ResultB,EnergyProduct*(Nl*Nd*cp^Uniquep*cs^Uniques)];
75 ];
76 (*Replace site weights AFTER taking the square!*)
77 SquareOfAverage=Expand[Total[ResultB]^2];
78 ResultB={};
79 ListOfAllTermsB=List@@SquareOfAverage;
80 For[i=1,i<=Length[ListOfAllTermsB],i++,
81     TmpList=List@@ListOfAllTermsB[[i]];
82     Uniquews={};
83     For[j=1,j<=11,j++,
84         AppendTo[
85             Uniquews,
86             Length[
87                 Cases[
88                     TmpList,
89                     MatchPowersOf[ToString[StringForm["w`^",j]]]^_.
90                 ]
91             ]
92         ];
93     ];
94     EnergyProduct=Times@@DeleteCases[TmpList,MatchPowersOf["w*"]^_.];
95     For[j=1,j<=11,j++,
96         EnergyProduct=EnergyProduct*SiteWeights[[j]]^Uniquews[[j]];
97     ];
98     AppendTo[ResultB,EnergyProduct];
99 ]; (*end of loop over sum terms*)
100 SquareOfAverage=Collect[FullSimplify[Total[ResultB]],cp];
101 FullSimplify[2*(AverageOfSquare-SquareOfAverage)]
102 ] (*end of module*)

```

Finally, the variance for unlike and like pairs can be calculated as follows.

```

1 (*Variance for unlike pairs, where atoms in the unit cell have type p and*)
2 (*atoms above the fault have type s*)
3 VarUnlike=CalcVarianceUnlike[EnergyChange];
4 (*Adding the variance of the opposite pair*)
5 Swap1=VarUnlike/.{cp->tp,cs->ts};
6 Swap2=Swap1/.{ts->cp,tp->cs};
7 VarUnlikeSwapped=FullSimplify[Swap2];
8 VarUnlikeCombined=FullSimplify[VarUnlike+VarUnlikeSwapped]
9 (*Variance of like pairs of solutes with concentration c*)
10 VarLike=(1/2*VarUnlikeCombined)/.{cp->c,cs->c}

```

A.7 E_{det} under Stress

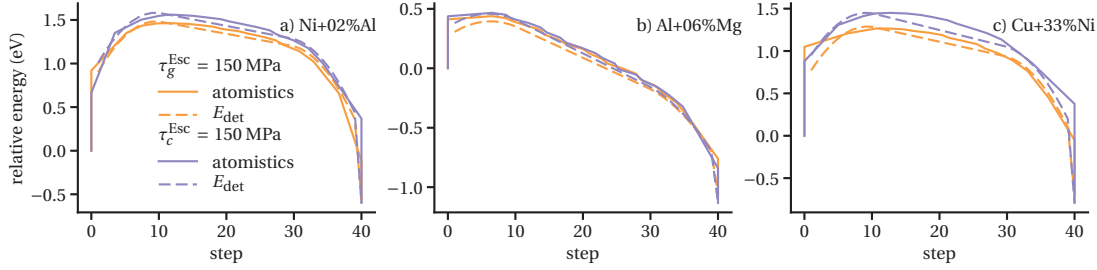


Figure A.12: Relative energy during cross-slip under 150 MPa Escaig stress as a function of step, i.e. length of the cross-slipped segment in Burgers vectors; solid lines: results from atomistic transition path calculations; dashed lines: determinisitic energy E_{det} for random walk calculations (Eq. 4.10).

Fig. A.12 compares E_{det} according to Eq. 4.10 with $N_c = 10$, and $\tau_{\text{glide}}^{\text{Esc}} = 150 \text{ MPa}$ or $\tau_{\text{cross}}^{\text{Esc}} = 150 \text{ MPa}$ to results from atomistic calculations. The cross-slipped length in the atomistic calculations was measured using the dislocation analysis (DXA) algorithm implemented in Ovito [135, 136]. The best match is obtained in the case of Ni-15 at.% Al. In Al-06 at.% Mg and Cu-33 at.% Ni, E_{det} underestimates the relative energy, especially near the center of the curve. In the case of Cu-33 at.% Ni, the error is larger when the Escaig stress is applied on the cross-slip plane, which is a consequence of neglecting the stress effect on the constriction on this plane. However, the difference between activation energies obtained from the E_{det} curve and from atomistic calculations is typically less than 0.1 eV for Escaig stresses up to 300 MPa, see Fig. A.13.

Our model of the effect of a Schmid stress on the cross-slip plane can be verified by comparing activation energies predicted with Eq. 4.10 to results from atomistic transition path calculations reported by Kang et al. [60], see Fig. A.14. We also show their predictions based on the Friedel-Escaig model. Note that the material is pure Ni. When evaluating Eq. 4.10 to find the activation energy, we used the material parameters reported in their publication ($a = 3.52 \text{ \AA}$, $C_{11} = 244 \text{ GPa}$, $C_{12} = 149 \text{ GPa}$, $C_{44} = 119 \text{ GPa}$, $\Delta E_{\text{act,avg}} \approx 2.27 \text{ eV}$). The activation energies predicted using the stress-dependent deterministic energy profile are only about 0.06 eV higher than the atomistic energies. Qualitatively and quantitatively, a better match is obtained than with the Friedel-Escaig model.

A.8. Correlation between ΔE_{act} and ΔE_{end}

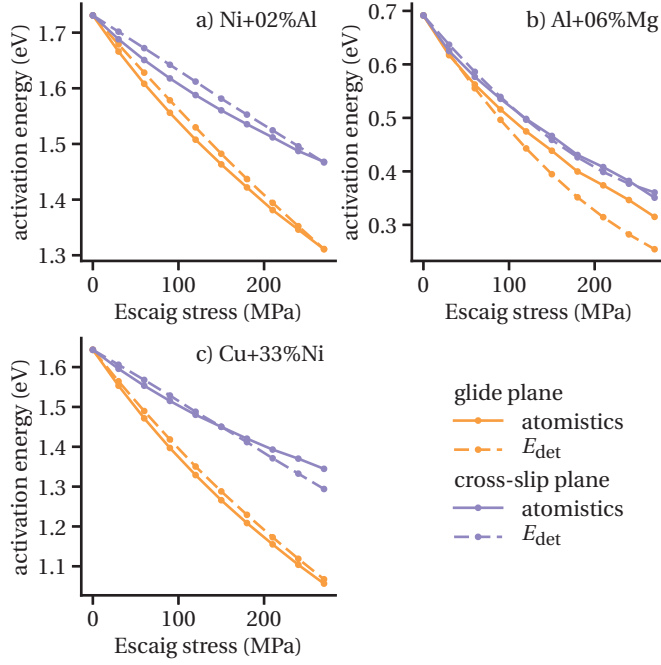


Figure A.13: Cross-slip activation energies as a function of Escaig stress on the glide (Yellow) or cross-slip plane (Violet); solid lines: results from atomistic transition path calculations; dashed lines: maximum of the deterministic energy E_{det} for random walk calculations (Eq. 4.10)

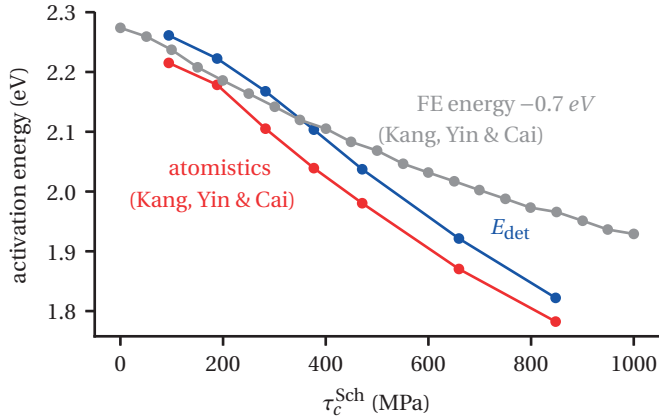


Figure A.14: Cross-slip activation energies in pure Ni as a function of Schmid stress on the cross-slip plane. Red: atomistic data reported by Kang et al. [60]; gray: values calculated by Kang et al. using their implementation of the Friedel-Escaig [32, 43] model, shifted by -0.7 eV ; blue: maximum of the deterministic energy E_{det} for random walk calculations (Eq. 4.10, evaluated with the material properties reported by Kang et al.).

A.8 Correlation between ΔE_{act} and ΔE_{end}

Fig. A.15 shows the correlations between the distributions of ΔE_{act} and ΔE_{end} from the atomistic and random walk calculations reported in Sec. 4.3.1 ($N_b = 40$, zero stress). Linear

Appendix A. Appendix

regression yields a slope of 0.53–0.54 for the random walk data. In case of the atomistic calculations, the slope shows more variation. The mean value across all alloys is 0.5, however.

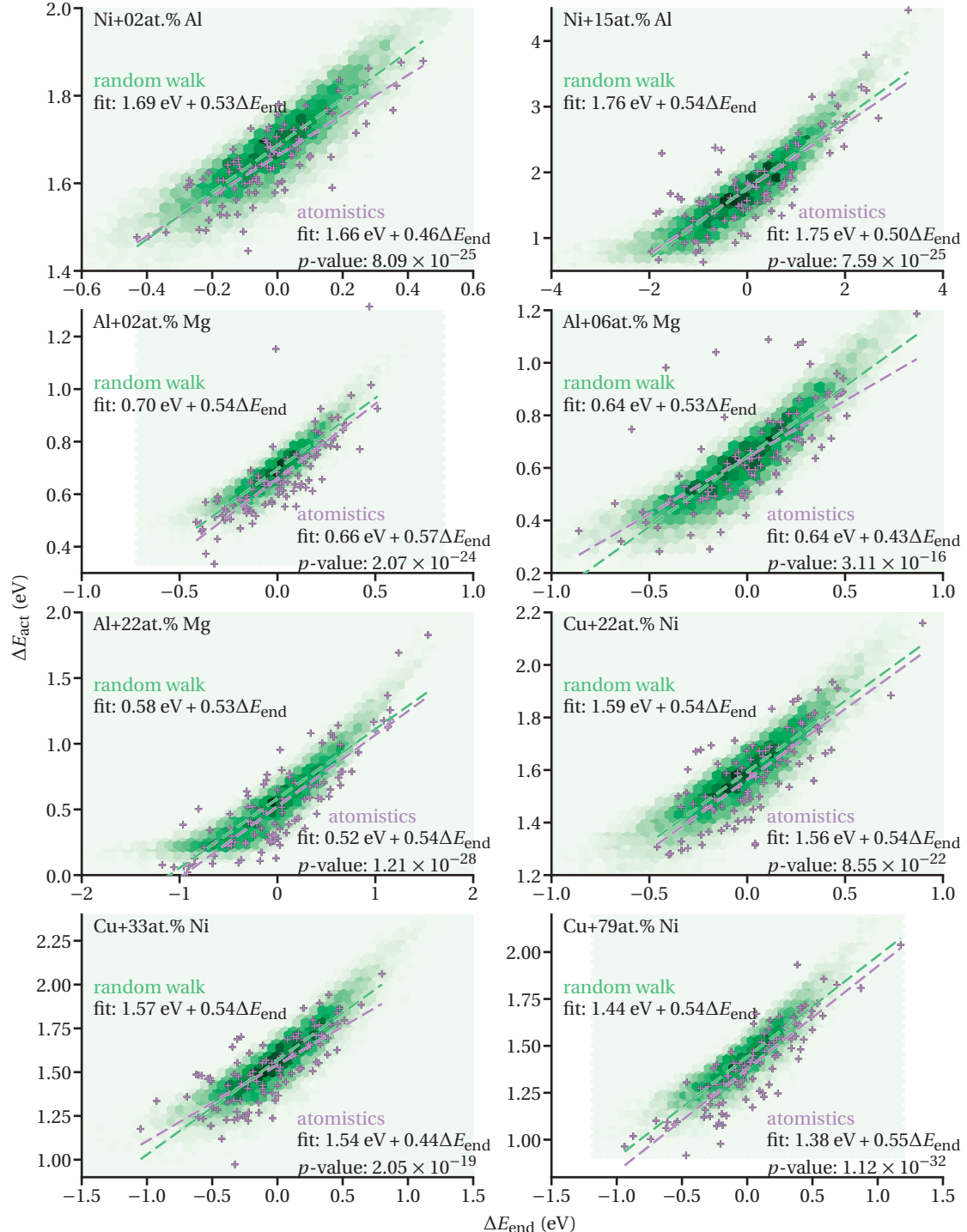


Figure A.15: Correlation between ΔE_{act} and ΔE_{end} , in atomistic (violet, crosses) and random walk (green, hexagonal bins) calculations from Sec. 4.3.1 ($N_b = 40$, zero stress)

Bibliography

- [1] P. M. Anderson, J. P. Hirth, and J. Lothe. *Theory of Dislocations*. 4th ed. New York: Cambridge University Press, 2017. ISBN: 978-0-521-86436-7.
- [2] S. D. Andrews, H. Sehitoglu, and I. Karaman. "Constriction Energy in the Presence of a Solute Field". In: *Journal of Applied Physics* 87.5 (2000), p. 2194. ISSN: 00218979. doi: 10.1063/1.372161.
- [3] A. S. Argon. "A New Model of Dynamic Recovery for Stage III of Pure FCC Metals without Cross Slip". In: *International Journal of Materials Research* 100.4 (2009), pp. 488–493. doi: 10.3139/146.110059.
- [4] S. Arrhenius. "Über die Reaktionsgeschwindigkeit bei der Inversion von Rohrzucker durch Säuren". In: *Zeitschrift für physikalische Chemie* 4.6 (1889), pp. 226–248.
- [5] Z. S. Basinski. "Work Hardening: Surface Effects. Dislocation Distribution in Deformed Copper Single Crystals". In: *Discussions of the Faraday Society* 38 (1964), pp. 93–102. doi: 10.1039/DF9643800093.
- [6] R. P. Bell. "The Theory of Reactions Involving Proton Transfers". In: *Proceedings of the Royal Society of London. A* 154 (1936), pp. 414–429. doi: 10.1098/rspa.1936.0060.
- [7] E. Bitzek et al. "Dislocation Cross-Slip in Nanocrystalline FCC Metals". In: *Physical Review Letters* 100.23 (June 2008). ISSN: 0031-9007, 1079-7114. doi: 10.1103/PhysRevLett.100.235501.
- [8] E. Bitzek et al. "Structural Relaxation Made Simple". In: *Physical Review Letters* 97.17 (Oct. 2006). ISSN: 0031-9007, 1079-7114. doi: 10.1103/PhysRevLett.97.170201.
- [9] J. Bonneville and B. Escaig. "Cross-Slipping Process and the Stress-Orientation Dependence in Pure Copper". In: *Acta Metallurgica* 27 (1979), pp. 1477–1486. doi: 10.1016/0001-6160(79)90170-6.
- [10] J. Bonneville, B. Escaig, and J. Martin. "A Study of Cross-Slip Activation Parameters in Pure Copper". In: *Acta Metallurgica* 36.8 (1988), pp. 1989–2002. doi: 10.1016/0001-6160(88)90301-X.
- [11] L. M. Brown. "Toward a Sound Understanding of Dislocation Plasticity". In: *Metallurgical Transactions A* 22.8 (1991), pp. 1693–1708. doi: 10.1007/BF02646493.
- [12] W. Cai and W. D. Nix. *Imperfections in Crystalline Solids*. 1st ed. Cambridge, UK: Cambridge University Press, 2016. ISBN: 978-1-107-12313-7.

Bibliography

- [13] W. Cai et al. "A Non-Singular Continuum Theory of Dislocations". In: *Journal of the Mechanics and Physics of Solids* 54.3 (Mar. 2006), pp. 561–587. ISSN: 00225096. doi: 10.1016/j.jmps.2005.09.005.
- [14] D. Caillard and J. Martin. *Thermally Activated Mechanisms in Crystal Plasticity*. Ed. by R. Cahn. 1st. Vol. 8. Pergamon Materials Series. Amsterdam: Pergamon, 2003.
- [15] T. Cao et al. "The Influence of Al Elements on the Structure and the Creep Behavior of AlxCrFeNi High Entropy Alloys". In: *Materials Letters* 164 (Feb. 2016), pp. 344–347. ISSN: 0167577X. doi: 10.1016/j.matlet.2015.11.016.
- [16] C. Carter and S. Holmes. "The Stacking Fault Energy of Nickel". In: *Philosophical Magazine* 35.5 (1977), pp. 1161–1172. doi: 10.1080/14786437708232942.
- [17] D. Cockayne, M. Jenkins, and I. Ray. "The Measurement of Stacking-Fault Energies of Pure Face-Centred Cubic Metals". In: *Philosophical Magazine* 24.192 (1971), pp. 1383–1392. doi: 10.1080/14786437108217419.
- [18] A. H. Cottrell. "Theory of Dislocations". In: *Progress in Metal Physics* 1 (1949).
- [19] P. Coulomb. "Comment on Graphs Relating Some Property to Stacking Fault Energy". In: *Scripta Metallurgica* 15.7 (1981), pp. 769–770. doi: 10.1016/0036-9748(81)90017-X.
- [20] M. S. Daw and M. Baskes. "Embedded-Atom Method: Derivation and Application to Impurities, Surfaces, and Other Defects in Metals". In: *Physical Review B* 29.12 (1984), pp. 6443–6453. doi: 10.1103/PhysRevB.29.6443.
- [21] K. A. Dill and S. Bromberg. *Molecular Driving Forces*. 2nd. London, New York: Garland Science, 2011. ISBN: 978-0-8153-4430-8.
- [22] I. L. Dillamore and W. Roberts. "Rolling Textures in F.C.C. and B.C.C. Metals". In: *Acta Metallurgica* 12.3 (1964), pp. 281–293. doi: 10.1016/0001-6160(64)90204-4.
- [23] D. E. Dominici. "The Inverse of the Cumulative Standard Normal Probability Function". In: *Integral Transforms and Special Functions* 14.4 (Aug. 2003), pp. 281–292. ISSN: 1065-2469, 1476-8291. doi: 10.1080/1065246031000081698.
- [24] J. Dorn and N. Jaffe. "Effect of Temperature on the Creep of Polycrystalline Aluminum by the Cross-Slip Mechanism". In: *Transactions of the Metallurgical Society of AIME* 221 (1961), pp. 229–233.
- [25] J.-P. Du, C.-Y. Wang, and T. Yu. "Cross-Slip Process in Model Ni(Al) Solid Solution: An Embedded-Atom Method Study". In: *Computational Materials Science* 91 (Aug. 2014), pp. 192–199. ISSN: 09270256. doi: 10.1016/j.commatsci.2014.04.063.
- [26] M. S. Duesbery. "Dislocation Motion, Constriction and Cross-Slip in FCC Metals". In: *Modelling and Simulation in Materials Science and Engineering* 6.1 (1998), p. 35. doi: 10.1088/0965-0393/6/1/005.
- [27] M. S. Duesbery, N. P. Louat, and K. Sadananda. "The Mechanics and Energetics of Cross-Slip". In: *Acta metallurgica et materialia* 40.1 (1992), pp. 149–158. doi: 10.1016/0956-7151(92)90208-V.
- [28] W. E, W. Ren, and E. Vandendijnen. "Finite Temperature String Method for the Study of Rare Events". In: *The Journal of Physical Chemistry B* 109.14 (2005), pp. 6688–6693. ISSN: 1520-6106, 1520-5207. doi: 10.1021/jp0455430.

Bibliography

- [29] W. E, W. Ren, and E. Vanden-Eijnden. "Simplified and Improved String Method for Computing the Minimum Energy Paths in Barrier-Crossing Events". In: *The Journal of Chemical Physics* 126.16 (2007), p. 164103. ISSN: 00219606. doi: 10.1063/1.2720838.
- [30] W. E, W. Ren, and E. Vanden-Eijnden. "String Method for the Study of Rare Events". In: *Physical Review B* 66.5 (Aug. 2002). ISSN: 0163-1829, 1095-3795. doi: 10.1103/PhysRevB.66.052301.
- [31] B. Escaig. "Contribution à l'étude des déviations dans la structure cubique faces centrées, cubic centrée, et hexagonale compacte". PhD. Paris: Université de Paris, 1968.
- [32] B. Escaig. "Sur le glissement dévié des dislocations dans la structure cubique à faces centrées". In: *Journal de Physique* 29.2-3 (1968), pp. 225–239. ISSN: 0302-0738. doi: 10.1051/jphys:01968002902-3022500.
- [33] U. Essmann. "Elektronenmikroskopische Untersuchung der Versetzungsanordnung in plastisch verformten Kupfereinkristallen". In: *Acta Metallurgica* 12.12 (1964), pp. 1468–1470. doi: 10.1016/0001-6160(64)90142-7.
- [34] U. Essmann and H. Mughrabi. "Annihilation of Dislocations during Tensile and Cyclic Deformation and Limits of Dislocation Densities". In: *Philosophical Magazine A* 40.6 (1979), pp. 731–756. doi: 10.1080/01418617908234871.
- [35] Y. Estrin et al. "A Dislocation-Based Model for All Hardening Stages in Large Strain Deformation". In: *Acta Materialia* 46.15 (1998), pp. 5509–5522. doi: 10.1016/S1359-6454(98)00196-7.
- [36] M. G. Evans and M. Polanyi. "Further Considerations on the Thermodynamics of Chemical Equilibria and Reaction Rates". In: *Transactions of the Faraday Society* 32 (1936), pp. 1333–1360. doi: 10.1039/TF9363201333.
- [37] H. Eyring. "The Activated Complex in Chemical Reactions". In: *The Journal of Chemical Physics* 3.2 (Feb. 1935), pp. 107–115. ISSN: 0021-9606, 1089-7690. doi: 10.1063/1.1749604.
- [38] R. A. Fisher and F. Yates. *Statistical Tables for Biological, Agricultural and Medical Research*. 3rd ed. London: Oliver & Boyd, 1948.
- [39] R. L. Fleischer. "Cross Slip of Extended Dislocations". In: *Acta Metallurgica* 7.2 (1959), pp. 134–135. doi: 10.1016/0001-6160(59)90122-1.
- [40] F. C. Frank and W. T. Read Jr. "Multiplication Processes for Slow Moving Dislocations". In: *Physical Review* 79.4 (1950), p. 722.
- [41] J. A. Frenkel. "Zur Theorie der Elastizitätsgrenze und der Festigkeit kristallinischer Körper". In: *Zeitschrift für Physik* 37.7-8 (1926), pp. 572–609. doi: 10.1007/BF01397292.
- [42] J. Friedel. "Sur le flueage par déviation". In: *Revue de Physique Appliquée* 12.10 (1977), pp. 1649–1654. ISSN: 0035-1687. doi: 10.1051/rphysap:0197700120100164900.
- [43] J. Friedel. "Regarding Seeger's Paper on Work Hardening". In: *Dislocations and Mechanical Properties of Crystals*. Ed. by J. Fisher et al. John Wiley & Sons, Inc., 1957, pp. 330–332.
- [44] V. Gerold and H. P. Karnthaler. "On the Origin of Planar Slip in F.C.C. Alloys". In: *Acta Metallurgica* 37.8 (1989), pp. 2177–2183. doi: 10.1016/0001-6160(89)90143-0.

Bibliography

- [45] G. S. Hammond. "A Correlation of Reaction Rates". In: *Journal of the American Chemical Society* 77.2 (1955), pp. 334–338. doi: 10.1021/ja01607a027.
- [46] R. Heidenreich and W. Shockley. "Study of Slip in Aluminium Crystals by Electron Microscope and Electron Diffraction Methods". In: *Report of a Conference on Strength of Solids*. London: Physical Society, 1948, pp. 57–75.
- [47] G. Henkelman and H. Jónsson. "Improved Tangent Estimate in the Nudged Elastic Band Method for Finding Minimum Energy Paths and Saddle Points". In: *The Journal of Chemical Physics* 113.22 (2000), p. 9978. ISSN: 00219606. doi: 10.1063/1.1323224.
- [48] N. E. Henriksen and F. Y. Hansen. *Theories of Molecular Reaction Dynamics*. 1st ed. Oxford: Oxford University Press, 2008. ISBN: 978-0-19-920386-4.
- [49] M. R. Hestenes and E. Stiefel. "Methods of Conjugate Gradients for Solving Linear Systems". In: *Journal of Research of the National Bureau of Standards* 49.6 (1952), pp. 409–436. doi: 10.6028/jres.049.044.
- [50] P. Hirsch. "Extended Jogs in Dislocations in Face-Centred Cubic Metals". In: *Philosophical Magazine* 7.73 (1962), pp. 67–93. doi: 10.1080/14786436208201859.
- [51] P. Hirsch. "The Interpretation of the Slip Pattern in Terms of Dislocation Movements". In: *Journal of the Institute of Metals* 86 (1957), p. 13.
- [52] J. D. Honeycutt and H. C. Andersen. "Molecular Dynamics Study of Melting and Freezing of Small Lennard-Jones Clusters". In: *Journal of Physical Chemistry* 91 (1987), pp. 4950–4963. doi: 10.1021/j100303a014.
- [53] S. I. Hong and C. Laird. "Mechanisms of Slip Mode Modification in F.C.C. Solid Solutions". In: *Acta metallurgica et materialia* 38.8 (1990), pp. 1581–1594. doi: 10.1016/j.msea.2012.12.044.
- [54] A. M. Hussein et al. "Microstructurally Based Cross-Slip Mechanisms and Their Effects on Dislocation Microstructure Evolution in FCC Crystals". In: *Acta Materialia* 85 (Feb. 2015), pp. 180–190. ISSN: 13596454. doi: 10.1016/j.actamat.2014.10.067.
- [55] P.J. Jackson. "The Role of Cross-Slip in the Plastic Deformation of Crystals". In: *Materials Science and Engineering* 57.1 (1983), pp. 39–47. doi: 10.1016/0025-5416(83)90025-3.
- [56] M. L. Jenkins. "Measurement of the Stacking-Fault Energy of Gold Using the Weak-Beam Technique of Electron Microscopy". In: *Philosophical Magazine* 26.3 (Sept. 1972), pp. 747–751. ISSN: 0031-8086. doi: 10.1080/14786437208230118.
- [57] C. Jin, Y. Xiang, and G. Lu. "Dislocation Cross-Slip Mechanisms in Aluminum". In: *Philosophical Magazine* 91.32 (Nov. 2011), pp. 4109–4125. ISSN: 1478-6435, 1478-6443. doi: 10.1080/14786435.2011.602030.
- [58] E. Jones, T. Oliphant, P. Peterson, et al. *SciPy: Open Source Scientific Tools for Python*. 2001.
- [59] H. Jónsson, G. Mills, and K. W. Jacobsen. "Nudged Elastic Band Method for Finding Minimum Energy Paths of Transitions". In: *Classical and Quantum Dynamics in Condensed Phase Simulations*. Ed. by B. Berne, G. Cicotti, and D. Coker. World Scientific, 1998, pp. 385–404.

- [60] K. Kang, J. Yin, and W. Cai. "Stress Dependence of Cross Slip Energy Barrier for Face-Centered Cubic Nickel". In: *Journal of the Mechanics and Physics of Solids* 62 (Jan. 2014), pp. 181–193. ISSN: 00225096. doi: 10.1016/j.jmps.2013.09.023.
- [61] K. Karhausen and F. Roters. "Development and Application of Constitutive Equations for the Multiple-Stand Hot Rolling of Al-Alloys". In: *Journal of Materials Processing Technology* 123 (2002), pp. 155–166. doi: 10.1016/S0924-0136(02)00081-X.
- [62] U. F. Kocks. "Laws for Work-Hardening and Low-Temperature Creep". In: *Journal of Engineering Materials and Technology* 98.1 (1976), pp. 76–85. doi: 10.1115/1.3443340.
- [63] J. S. Koehler. "The Nature of Work-Hardening". In: *Physical Review* 86.1 (1952), pp. 52–59. doi: 10.1103/PhysRev.86.52.
- [64] A. N. Kolmogorov. "Sulla determinazione empirica di una legge di distribuzione". In: *Giornale dell'Istituto Italiano degli Attuari* 4 (1933), pp. 83–91.
- [65] E. L. Kolsbjerg, M. N. Groves, and B. Hammer. "An Automated Nudged Elastic Band Method". In: *The Journal of Chemical Physics* 145.9 (Sept. 2016), p. 094107. ISSN: 0021-9606, 1089-7690. doi: 10.1063/1.4961868.
- [66] L. Kubin, T. Hoc, and B. Devincre. "Dynamic Recovery and Its Orientation Dependence in Face-Centered Cubic Crystals". In: *Acta Materialia* 57.8 (May 2009), pp. 2567–2575. ISSN: 13596454. doi: 10.1016/j.actamat.2009.02.013.
- [67] L. P. Kubin et al. "Dislocation Microstructures and Plastic Flow: A 3D Simulation". In: *Solid State Phenomena* 23-24 (1992), pp. 455–472. ISSN: 1662-9779. doi: 10.4028/www.scientific.net/SSP.23-24.455.
- [68] T. Leffers and O. B. Pedersen. "The Activation Energy for the FCC Rolling-Texture Transition as Related to the Activation Energy for Cross Slip". In: *Scripta materialia* 46.10 (2002), pp. 741–746. doi: 10.1016/S1359-6462(02)00065-9.
- [69] T. Leffers and R. Ray. "The Brass-Type Texture and Its Deviation from the Copper-Type Texture". In: *Progress in Materials Science* 54.3 (May 2009), pp. 351–396. ISSN: 00796425. doi: 10.1016/j.pmatsci.2008.09.002.
- [70] P. Lévy. "Sur certains processus stochastiques homogènes". In: *Compositio Mathematica* 7 (1940), pp. 283–339.
- [71] G. Leyson, L. Hector, and W. Curtin. "Solute Strengthening from First Principles and Application to Aluminum Alloys". In: *Acta Materialia* 60.9 (May 2012), pp. 3873–3884. ISSN: 13596454. doi: 10.1016/j.actamat.2012.03.037.
- [72] G. P. M. Leyson et al. "Quantitative Prediction of Solute Strengthening in Aluminium Alloys". In: *Nature Materials* 9.9 (Sept. 2010), pp. 750–755. ISSN: 1476-1122, 1476-4660. doi: 10.1038/nmat2813.
- [73] J. Liu et al. "Deformation Twinning Behaviors of the Low Stacking Fault Energy High-Entropy Alloy: An in-Situ TEM Study". In: *Scripta Materialia* 137 (Aug. 2017), pp. 9–12. ISSN: 13596462. doi: 10.1016/j.scriptamat.2017.05.001.
- [74] X.-Y. Liu et al. "EAM Potential for Magnesium from Quantum Mechanical Forces". In: *Modelling and Simulation in Materials Science and Engineering* 4 (1996), pp. 293–303. doi: 10.1088/0965-0393/4/3/004.

Bibliography

- [75] Z. S. Liu and V. Mohles. "Solution Strengthening of Various Elements in Aluminium Alloys". In: *Materials Science Forum* 794-796 (June 2014), pp. 473–478. ISSN: 1662-9752. doi: 10.4028/www.scientific.net/MSE794-796.473.
- [76] J. Lytton, L. Shepard, and J. Dorn. "The Activation Energies for Creep of Single Aluminum Crystals Favorably Oriented for (III)[T0I] Slip". In: *Transactions of the American Institute of Mining, Metallurgical and Petroleum Engineers* 212 (1958), p. 220.
- [77] R. Madec, B. Devincre, and L. P. Kubin. "Simulation of Dislocation Patterns in Multislip". In: *Scripta materialia* 47.10 (2002), pp. 689–695. doi: 10.1016/S1359-6462(02)00185-9.
- [78] M. Marcinkowski, K. Sadananda, and N. J. Olson. "Cross Slip of Extended Dislocations in Disordered Face-Centred-Cubic Alloys". In: *Crystal Lattice Defects* 5 (1974), pp. 187–198.
- [79] J. Marian, J. Knap, and M. Ortiz. "Nanovoid Deformation in Aluminum under Simple Shear". In: *Acta Materialia* 53.10 (June 2005), pp. 2893–2900. ISSN: 13596454. doi: 10.1016/j.actamat.2005.02.046.
- [80] W. Meyer and H. Neldel. "Über die Beziehungen zwischen der Energiekonstanten E und der Mengenkonstanten a in der Leitwerts-Temperaturformel bei oxydischen Halbleitern". In: *Zeitschrift für technische Physik* 18 (1937), pp. 588–593.
- [81] G. Mills and H. Jónsson. "Quantum and Thermal Effects in H₂ Dissociative Adsorption: Evaluation of Free Energy Barriers in Multidimensional Quantum Systems". In: *Physical review letters* 72.7 (1994), p. 1124. doi: 10.1103/PhysRevLett.72.1124.
- [82] M. J. Mills and P. Stadelmann. "A Study of the Structure of Lomer and 60° Dislocations in Aluminium Using High-Resolution Transmission Electron Microscopy". In: *Philosophical Magazine A* 60.3 (Sept. 1989), pp. 355–384. ISSN: 0141-8610. doi: 10.1080/01418618908213867.
- [83] D. Mordehai, I. Kelson, and G. Makov. "Cross-Slip and Annihilation of Screw Dislocations in Cu: A Molecular Dynamics Study". In: *Materials Science and Engineering: A* 400-401 (July 2005), pp. 37–39. ISSN: 09215093. doi: 10.1016/j.msea.2005.03.077.
- [84] N. F. Mott. "A Theory of the Origin of Fatigue Cracks". In: *Acta Metallurgica* 6.3 (1958), pp. 195–197. doi: 10.1016/0001-6160(58)90007-5.
- [85] N. F. Mott. "Mechanical Properties of Metals". In: *Physica* 15.1-2 (1949), pp. 119–134. doi: 10.1016/0031-8914(49)90034-8.
- [86] F. R. N. Nabarro. "Dislocations in a Simple Cubic Lattice". In: *Proceedings of the Physical Society* 59.2 (1947), p. 256. doi: 10.1088/0959-5309/59/2/309.
- [87] W. D. Nix, J. C. Gibeling, and D. A. Hughes. "Time-Dependent Deformation of Metals". In: *Metallurgical Transactions A* 16.12 (1985), pp. 2215–2226. doi: 10.1007/BF02670420.
- [88] W. G. Nöhring and W. A. Curtin. "Dislocation Cross-Slip in FCC Solid Solution Alloys". In: *Acta Materialia* 128 (Apr. 2017), pp. 135–148. ISSN: 13596454. doi: 10.1016/j.actamat.2017.02.027.
- [89] W. G. Nöhring and W. A. Curtin. "Thermodynamic Properties of Average-Atom Interatomic Potentials for Alloys". In: *Modelling and Simulation in Materials Science and Engineering* 24.4 (May 2016), p. 045017. ISSN: 0965-0393, 1361-651X. doi: 10.1088/0965-0393/24/4/045017.

- [90] W. G. Nöhring et al. "Wedge-Shaped Twins and Pseudoelasticity in FCC Metallic Nanowires under Bending". In: *Extreme Mechanics Letters* 8 (Sept. 2016), pp. 140–150. ISSN: 23524316. doi: 10.1016/j.eml.2016.03.001.
- [91] B. Onat and S. Durukanolu. "An Optimized Interatomic Potential for CuNi Alloys with the Embedded-Atom Method". In: *Journal of Physics: Condensed Matter* 26.3 (Jan. 2014), p. 035404. ISSN: 0953-8984, 1361-648X. doi: 10.1088/0953-8984/26/3/035404.
- [92] E. Oren, E. Yahel, and G. Makov. "Kinetics of Dislocation Cross-Slip: A Molecular Dynamics Study". In: *Computational Materials Science* 138 (Oct. 2017), pp. 246–254. ISSN: 09270256. doi: 10.1016/j.commatsci.2017.06.039.
- [93] E. Osswald. "Zugversuche an Kupfer-Nickelkristallen". In: *Zeitschrift für Physik* 83.1 (1933), pp. 55–78. ISSN: 0044-3328. doi: 10.1007/BF01331092.
- [94] F. Otto et al. "The Influences of Temperature and Microstructure on the Tensile Properties of a CoCrFeMnNi High-Entropy Alloy". In: *Acta Materialia* 61.15 (Sept. 2013), pp. 5743–5755. ISSN: 13596454. doi: 10.1016/j.actamat.2013.06.018.
- [95] R. Peierls. "The Size of a Dislocation". In: *Proceedings of the Physical Society* 52.1 (1940), p. 34.
- [96] S. Plimpton. "Fast Parallel Algorithms for Short-Range Molecular Dynamics". In: *Journal of Computational Physics* 117 (1995), pp. 1–19. doi: 10.1006/jcph.1995.1039.
- [97] J. Poirier. "On the Symmetrical Role of Cross-Slip of Screw Dislocations and Climb of Edge Dislocations as Recovery Processes Controlling High-Temperature Creep". In: *Revue de Physique Appliquée* 11.6 (1976), pp. 731–738. ISSN: 0035-1687. doi: 10.1051/rphysap:01976001106073100.
- [98] G. Purja Pun and Y. Mishin. "Development of an Interatomic Potential for the Ni-Al System". In: *Philosophical Magazine* 89.34-36 (Dec. 2009), pp. 3245–3267. ISSN: 1478-6435, 1478-6443. doi: 10.1080/14786430903258184.
- [99] W. Püschl and G. Schoeck. "Calculation of Cross-Slip Parameters in FCC Crystals". In: *Materials Science and Engineering: A* 164.1 (1993), pp. 286–289. doi: 10.1016/0921-5093(93)90679-9.
- [100] W. Püschl. "Models for Dislocation Cross-Slip in Close-Packed Crystal Structures: A Critical Review". In: *Progress in materials science* 47.4 (2002), pp. 415–461. doi: 10.1016/S0079-6425(01)00003-2.
- [101] B. R. Ramírez, N. Ghoniem, and G. Po. "Ab Initio Continuum Model for the Influence of Local Stress on Cross-Slip of Screw Dislocations in FCC Metals". In: *Physical Review B* 86.9 (Sept. 2012). ISSN: 1098-0121, 1550-235X. doi: 10.1103/PhysRevB.86.094115.
- [102] S. I. Rao, T. A. Parthasarathy, and C. Woodward. "Atomistic Simulation of Cross-Slip Processes in Model FCC Structures". In: *Philosophical Magazine A* 79.5 (May 1999), pp. 1167–1192. ISSN: 0141-8610, 1460-6992. doi: 10.1080/01418619908210354.
- [103] S. Rao et al. "Activated States for Cross-Slip at Screw Dislocation Intersections in Face-Centered Cubic Nickel and Copper via Atomistic Simulation". In: *Acta Materialia* 58.17 (2010), pp. 5547–5557. ISSN: 13596454. doi: 10.1016/j.actamat.2010.06.005.
- [104] S. Rao et al. "Atomistic Simulations of Cross-Slip Nucleation at Screw Dislocation Intersections in Face-Centered Cubic Nickel". In: *Philosophical Magazine* 89.34-36 (Dec. 2009), pp. 3351–3369. ISSN: 1478-6435, 1478-6443. doi: 10.1080/14786430903286201.

Bibliography

- [105] S. Rao et al. “Atomistic Simulations of Dislocation Behavior in a Model FCC Multicomponent Concentrated Solid Solution Alloy”. In: *Acta Materialia* 134 (Aug. 2017), pp. 188–194. ISSN: 13596454. doi: 10.1016/j.actamat.2017.05.071.
- [106] S. Rao et al. “Atomistic Simulations of Surface Cross-Slip Nucleation in Face-Centered Cubic Nickel and Copper”. In: *Acta Materialia* 61.7 (Apr. 2013), pp. 2500–2508. ISSN: 13596454. doi: 10.1016/j.actamat.2013.01.026.
- [107] S. Rao et al. “Calculations of Intersection Cross-Slip Activation Energies in FCC Metals Using Nudged Elastic Band Method”. In: *Acta Materialia* 59.19 (Nov. 2011), pp. 7135–7144. ISSN: 13596454. doi: 10.1016/j.actamat.2011.08.029.
- [108] S. Rao et al. “Screw Dislocation Cross Slip at Cross-Slip Plane Jogs and Screw Dipole Annihilation in FCC Cu and Ni Investigated via Atomistic Simulations”. In: *Acta Materialia* 101 (Dec. 2015), pp. 10–15. ISSN: 13596454. doi: 10.1016/j.actamat.2015.08.070.
- [109] S. Rao et al. “Spontaneous Athermal Cross-Slip Nucleation at Screw Dislocation Intersections in FCC Metals and L1₂ Intermetallics Investigated via Atomistic Simulations”. In: *Philosophical Magazine* 93.22 (Aug. 2013), pp. 3012–3028. ISSN: 1478-6435, 1478-6443. doi: 10.1080/14786435.2013.799788.
- [110] T. Rasmussen et al. “Atomic Structure and Energetics of Constricted Screw Dislocations in Copper”. In: *Materials Science and Engineering: A* 234-236 (1997), pp. 544–547. doi: 10.1016/S0921-5093(97)00311-0.
- [111] T. Rasmussen et al. “Simulation of Structure and Annihilation of Screw Dislocation Dipoles”. In: *Philosophical Magazine A* 80.5 (May 2000), pp. 1273–1290. ISSN: 0141-8610, 1460-6992. doi: 10.1080/01418610008212115.
- [112] T. Rasmussen et al. “Atomistic Determination of Cross-Slip Pathway and Energetics”. In: *Physical review letters* 79.19 (1997), p. 3676. doi: 10.1103/PhysRevLett.79.3676.
- [113] T. Rasmussen et al. “Simulations of the Atomic Structure, Energetics, and Cross Slip of Screw Dislocations in Copper”. In: *Physical Review B* 56.6 (1997), p. 2977. doi: 10.1103/PhysRevB.56.2977.
- [114] W. Read. *Dislocations in Crystals*. International Series in Pure and Applied Physics. New York, Toronto, London: McGraw-Hill Book Company, Inc., 1953.
- [115] E. Rodary et al. “Dislocation Glide in Model Ni(Al) Solid Solutions by Molecular Dynamics”. In: *Physical Review B* 70.5 (Aug. 2004). ISSN: 1098-0121, 1550-235X. doi: 10.1103/PhysRevB.70.054111.
- [116] S. Ryu, K. Kang, and W. Cai. “Entropic Effect on the Rate of Dislocation Nucleation”. In: *Proceedings of the National Academy of Sciences* 108.13 (2011), pp. 5174–5178.
- [117] G. Saada. “Cross-Slip and Work Hardening of FCC Crystals”. In: *Materials Science and Engineering: A* 137 (1991), pp. 177–183. doi: 10.1016/0921-5093(91)90333-I.
- [118] S. Saroukhani and D. Warner. “Investigating Dislocation Motion through a Field of Solutes with Atomistic Simulations and Reaction Rate Theory”. In: *Acta Materialia* 128 (2017), pp. 77–86. doi: 10.1016/j.actamat.2017.02.001.
- [119] R. O. Scattergood and D. J. Bacon. “The Orowan Mechanism in Anisotropic Crystals”. In: *Philosophical Magazine* 31.1 (1975), pp. 179–198. doi: 10.1080/14786437508229295.

- [120] G. Schoeck. "Beiträge zur Theorie der Versetzungen: Aufspaltung, Linienenergie und Quergleitung von Versetzungen". PhD thesis. Technische Hochschule Stuttgart, 1954.
- [121] G. Schoeck. "The Cross-Slip Energy Unresolved". In: *Philosophical Magazine Letters* 89.8 (Aug. 2009), pp. 505–515. ISSN: 0950-0839, 1362-3036. doi: 10.1080/09500830903092399.
- [122] G. Schoeck. "Thermodynamics and Thermal Activation of Dislocations". In: *Dislocations in Solids*. Ed. by F. R. N. Nabarro. Vol. 3. Amsterdam, New York, Oxford: North-Holland Publishing Company, 1980, pp. 65–163. ISBN: 0-444-85015-5.
- [123] G. Schoeck and W. Püschl. "Prismatic Slip in HCP Metals". In: *Proceedings of the 8th International Conference on the Strength of Metals and Alloys*. Ed. by P. Kettunen, T. Lepistö, and M. Lehtonen. Elsevier Ltd., 1988, pp. 239–244.
- [124] G. Schoeck and A. Seeger. "Activation Energy Problems Associated with Extended Dislocations". In: *Report of a Conference on Defects in Crystalline Solids*. London: Physical Society, 1955, pp. 340–346.
- [125] A. Seeger. "The Mechanism of Glide and Work Hardening in Face-Centered Cubic and Hexagonal Close-Packed Metals". In: *Dislocations and Mechanical Properties of Crystals*. Ed. by J. Fisher et al. John Wiley & Sons, Inc., 1957, pp. 243–329.
- [126] A. Seeger, R. Berner, and H. Wolf. "Die experimentelle Bestimmung von Stapelfehlerenergien kubisch-flächenzentrierter Metalle". In: *Zeitschrift für Physik* 155.2 (1959), pp. 247–262.
- [127] D. Sheppard, R. Terrell, and G. Henkelman. "Optimization Methods for Finding Minimum Energy Paths". In: *The Journal of Chemical Physics* 128.13 (2008), p. 134106. ISSN: 00219606. doi: 10.1063/1.2841941.
- [128] C. Singh, A. Mateos, and D. Warner. "Atomistic Simulations of Dislocation-Precipitate Interactions Emphasize Importance of Cross-Slip". In: *Scripta Materialia* 64.5 (Mar. 2011), pp. 398–401. ISSN: 13596462. doi: 10.1016/j.scriptamat.2010.10.041.
- [129] R. E. Smallman and D. Green. "The Dependence of Rolling Texture on Stacking Fault Energy". In: *Acta Metallurgica* 12.2 (1964), pp. 145–154. doi: 10.1016/0001-6160(64)90182-8.
- [130] N. V. Smirnov. "On the Estimation of the Discrepancy Between Empirical Curves of Distribution for Two Independent Samples". In: *Bulletin mathématiques de l'Université de Moscou* 2 (1939), pp. 3–14.
- [131] R. W. Smith and G. S. Was. "Application of Molecular Dynamics to the Study of Hydrogen Embrittlement in Ni-Cr-Fe Alloys". In: *Physical Review B* 40.15 (1989), pp. 10332–10336. doi: 10.1103/PhysRevB.40.10322.
- [132] J. W. Steeds and P. Hazzledine. "Dislocation Configurations in Deformed Copper and Copper 10%(Atomic) Aluminium Alloy". In: *Discussions of the Faraday Society* 38 (1964), pp. 103–110. doi: 10.1039/DF9643800103.
- [133] A. N. Stroh. "Constrictions and Jogs in Extended Dislocations". In: *Proceedings of the Physical Society. Section B* 67.5 (1954), p. 427. doi: 10.1088/0370-1301/67/5/307.
- [134] A. Stroh. "Dislocations and Cracks in Anisotropic Elasticity". In: *Philosophical Magazine* 3.30 (1958), pp. 625–646. doi: 10.1080/14786435808565804.

Bibliography

- [135] A. Stukowski. "Visualization and Analysis of Atomistic Simulation Data with OVITO—the Open Visualization Tool". In: *Modelling and Simulation in Materials Science and Engineering* 18.1 (Jan. 2010), p. 015012. ISSN: 0965-0393, 1361-651X. doi: 10.1088/0965-0393/18/1/015012.
- [136] A. Stukowski, V. V. Bulatov, and A. Arsenlis. "Automated Identification and Indexing of Dislocations in Crystal Interfaces". In: *Modelling and Simulation in Materials Science and Engineering* 20.8 (Dec. 2012), p. 085007. ISSN: 0965-0393, 1361-651X. doi: 10.1088/0965-0393/20/8/085007.
- [137] B. A. Szajewski, A. Hunter, and I. J. Beyerlein. "The Core Structure and Recombination Energy of a Copper Screw Dislocation: A Peierls Study". In: *Philosophical Magazine* 97.25 (Sept. 2017), pp. 2143–2163. ISSN: 1478-6435, 1478-6443. doi: 10.1080/14786435.2017.1328138.
- [138] T. S. van Erp, D. Moroni, and P. G. Bolhuis. "A Novel Path Sampling Method for the Calculation of Rate Constants". In: *The Journal of Chemical Physics* 118.17 (May 2003), pp. 7762–7774. ISSN: 0021-9606, 1089-7690. doi: 10.1063/1.1562614.
- [139] E. Vanden-Eijnden and M. Venturoli. "Revisiting the Finite Temperature String Method for the Calculation of Reaction Tubes and Free Energies". In: *The Journal of Chemical Physics* 130.19 (2009), p. 194103. ISSN: 0021-9606, 1089-7690. doi: 10.1063/1.3130083.
- [140] C. Varvenne, A. Luque, and W. A. Curtin. "Theory of Strengthening in FCC High Entropy Alloys". In: *Acta Materialia* 118 (Oct. 2016), pp. 164–176. ISSN: 13596454. doi: 10.1016/j.actamat.2016.07.040.
- [141] C. Varvenne et al. "Average-Atom Interatomic Potential for Random Alloys". In: *Physical Review B* 93.10 (2016), p. 104201. doi: 10.1103/PhysRevB.93.104201.
- [142] T. Vegge et al. "Atomistic Simulations of Cross-Slip of Jogged Screw Dislocations in Copper". In: *Philosophical Magazine Letters* 81.3 (Mar. 2001), pp. 137–144. ISSN: 0950-0839, 1362-3036. doi: 10.1080/09500830010019040.
- [143] T. Vegge. "Atomistic Simulations of Screw Dislocation Cross Slip in Copper and Nickel". In: *Materials Science and Engineering: A* 309 (2001), pp. 113–116. doi: 10.1016/S0921-5093(00)01624-5.
- [144] T. Vegge and K. W. Jacobsen. "Atomistic Simulations of Dislocation Processes in Copper". In: *Journal of Physics: Condensed Matter* 14.11 (2002), p. 2929. doi: 10.1088/0953-8984/14/11/309.
- [145] T. Vegge et al. "Determination of the of Rate Cross Slip of Screw Dislocations". In: *Physical review letters* 85.18 (2000), p. 3866. doi: 10.1103/PhysRevLett.85.3866.
- [146] G. H. Vineyard. "Frequency Factors and Isotope Effects in Solid State Rate Processes". In: *Journal of Physics and Chemistry of Solids* 3.1 (1957), pp. 121–127. doi: 10.1016/0022-3697(57)90059-8.
- [147] W. Voigt. *Lehrbuch der Kristallphysik*. Teubner, Leipzig, 1910.
- [148] A. F. Voter and S. P. Chen. "Accurate Interatomic Potentials for Ni, Al and Ni₃Al". In: *MRS Proceedings* 82 (1987), p. 175. doi: 10.1557/PROC-82-175.
- [149] S. van der Walt, S. C. Colbert, and G. Varoquaux. "The NumPy Array: A Structure for Efficient Numerical Computation". In: *Computing in Science & Engineering* 13.2 (2011), pp. 22–30. doi: 10.1109/MCSE.2011.37.

Bibliography

- [150] J. Washburn. "Intersection Cross Slip". In: *Applied Physics Letters* 7.7 (1965), p. 183. ISSN: 00036951. doi: 10.1063/1.1754369.
- [151] M. Wen, S. Fukuyama, and K. Yokogawa. "Cross-Slip Process in FCC Nickel with Hydrogen in a Stacking Fault: An Atomistic Study Using the Embedded-Atom Method". In: *Physical Review B* 75.14 (Apr. 2007). ISSN: 1098-0121, 1550-235X. doi: 10.1103/PhysRevB.75.144110.
- [152] M. Wen, S. Fukuyama, and K. Yokogawa. "Hydrogen-Affected Cross-Slip Process in FCC Nickel". In: *Physical Review B* 69.17 (May 2004). ISSN: 1098-0121, 1550-235X. doi: 10.1103/PhysRevB.69.174108.
- [153] H. Wolf. "Die Aktivierungsenergie für die Quergleitung aufgespalter Schraubenversetzungen". In: *Zeitschrift für Naturforschung* 15A (1960), pp. 180–193. doi: 10.1515/zna-1960-0302.
- [154] H. Wolf. "Die Aktivierungsenergie für die Quergleitung aufgespalter Schraubenversetzungen". PhD thesis. Technische Hochschule Stuttgart, 1959.
- [155] Wolfram Research, Inc. *Mathematica*. Champaign, Illinois, 2016.
- [156] Z. Wu and W. A. Curtin. "Mechanism and Energetics of $\langle c+a \rangle$ Dislocation Cross-Slip in HCP Metals". In: *Proceedings of the National Academy of Sciences* 113.40 (Oct. 2016), pp. 11137–11142. ISSN: 0027-8424, 1091-6490. doi: 10.1073/pnas.1603966113.
- [157] S. X. Xia and A. El-Azab. "A Preliminary Investigation of Dislocation Cell Structure Formation in Metals Using Continuum Dislocation Dynamics". In: *IOP Conference Series: Materials Science and Engineering* 89 (Aug. 2015), p. 012053. ISSN: 1757-8981, 1757-899X. doi: 10.1088/1757-899X/89/1/012053.
- [158] S. Xia and A. El-Azab. "Computational Modelling of Mesoscale Dislocation Patterning and Plastic Deformation of Single Crystals". In: *Modelling and Simulation in Materials Science and Engineering* 23.5 (July 2015), p. 055009. ISSN: 0965-0393, 1361-651X. doi: 10.1088/0965-0393/23/5/055009.
- [159] S. Xia, J. Belak, and A. El-Azab. "The Discrete-Continuum Connection in Dislocation Dynamics: I. Time Coarse Graining of Cross Slip". In: *Modelling and Simulation in Materials Science and Engineering* 24.7 (Oct. 2016), p. 075007. ISSN: 0965-0393, 1361-651X. doi: 10.1088/0965-0393/24/7/075007.
- [160] S. Xu et al. "Shear Stress- and Line Length-Dependent Screw Dislocation Cross-Slip in FCC Ni". In: *Acta Materialia* 122 (Jan. 2017), pp. 412–419. ISSN: 13596454. doi: 10.1016/j.actamat.2016.10.005.
- [161] J. A. Yasi, L. G. Hector, and D. R. Trinkle. "Prediction of Thermal Cross-Slip Stress in Magnesium Alloys from Direct First-Principles Data". In: *Acta Materialia* 59.14 (Aug. 2011), pp. 5652–5660. ISSN: 13596454. doi: 10.1016/j.actamat.2011.05.040.
- [162] J.-W. Yeh et al. "Nanostructured High-Entropy Alloys with Multiple Principal Elements: Novel Alloy Design Concepts and Outcomes". In: *Advanced Engineering Materials* 6.5 (May 2004), pp. 299–303. ISSN: 1438-1656, 1527-2648. doi: 10.1002/adem.200300567.

Acronyms

F-E Friedel-Escaig. 3, 5, 8–12, 24, 28–30, 51

BEP Bell-Evans-Polanyi. 45

CNA Common Neighbor Analysis. 22

EAM Embedded Atom Method. 17–19

FCC Face-Centered Cubic. iii, 1–6, 8, 11, 13, 17–19, 22, 26, 29, 30, 42, 49, 52, 71, 73, 77, 80

HCP Hexagonal Close-Packed. 3, 6

HEA High Entropy Alloy. 19, 73

MEP Minimum Energy Path. 14, 22–24, 84

NEB Nudged Elastic Band. 20, 22–24, 81–83, 85

PES Potential Energy Surface. 14, 15, 23, 24

WOLFRAM GEORG NÖHRING
CURRICULUM VITAE

e-mail: wolfram.nohring@epfl.ch

EDUCATION

2014–2018	PhD EPFL
2010–2013	M.Sc. (hons.), Advanced Materials and Processes, Friedrich-Alexander-Universität Erlangen-Nürnberg, Erlangen, Germany Master thesis: Towards a Finite Element Multiscale Model of the Accumulative Roll Bonding Process
2007–2010	B.Sc. (with distinction), Materials Science, Friedrich-Alexander-Universität Erlangen-Nürnberg, Erlangen, Germany Bachelor thesis: Atomistic Simulations of Single Crystal Nanostructures Subjected to Bending Loads
1997–2006	Allgemeine Hochschulreife (general qualification for university entrance) Friedrich-Alexander-Gymnasium, Neustadt a. d. Aisch, Germany

PUBLICATIONS IN PEER-REVIEWED JOURNALS

1. W. G. Nöhring and W. A. Curtin (Apr. 2017). “Dislocation Cross-Slip in Fcc Solid Solution Alloys”. In: *Acta Materialia* 128, pp. 135–148
2. W. G. Nöhring and W. A. Curtin (May 2016c). “Thermodynamic Properties of Average-Atom Interatomic Potentials for Alloys”. In: *Modelling and Simulation in Materials Science and Engineering* 24.4, p. 045017
3. W. G. Nöhring, J. J. Möller, Z. Xie, and E. Bitzek (Sept. 2016). “Wedge-Shaped Twins and Pseudoelasticity in FCC Metallic Nanowires under Bending”. In: *Extreme Mechanics Letters* 8, pp. 140–150
4. C. Varvenne, A. Luque, W. G. Nöhring, and W. A. Curtin (2016). “Average-Atom Interatomic Potential for Random Alloys”. In: *Physical Review B* 93.10, p. 104201
5. A. Prakash, W. G. Nöhring, R. A. Lebensohn, H. W. Höppel, and E. Bitzek (Apr. 2015). “A Multiscale Simulation Framework of the Accumulative Roll Bonding Process Accounting for Texture Evolution”. In: *Materials Science and Engineering: A* 631, pp. 104–119

PRESENTATIONS AT CONFERENCES

1. W. G. Nöhring and W. A. Curtin (2016b). *Cross-Slip in FCC Solid Solutions*. Presentation. MMM, Dijon
2. W. G. Nöhring and W. A. Curtin (2016a). *Cross-Slip in FCC Solid Solutions*. Presentation. EMMC15, Brussels
3. W. G. Nöhring, E. Bitzek, and Y. Umeno (2013). *Atomic Scale Analysis of Structural Instability in Nanostructures*. Poster. ICMM3, Warsaw

4. W. G. Nöhring, A. Prakash, and E. Bitzek (2013). *A Coupled Finite Element Polycrystal Texture Model of the Accumulative Roll Bonding Process*. Presentation. ICMM3, Warsaw
5. W. G. Nöhring, E. Bitzek, A. Kelling, and C. A. Volkert (2012). *Deformation Mechanisms of Twinned Au-Nanoparticles under Uniaxial Compression*. Presentation. IUMRS-IUMRS 2012, Yokohama
6. W. G. Nöhring, E. Bitzek, and Y. Umeno (2012). *Atomic Scale Analysis of Structural Instability in Nanostructures*. Poster. IUMRS-IUMRS 2012, Yokohama
7. A. Kelling, C. A. Volkert, W. G. Nöhring, and E. Bitzek (Mar. 2012). *Deformation Mechanisms of Twinned Au-Nanoparticles under Compression: Experiments and Simulation*. Presentation. DPG Spring Meeting, Berlin

ARTICLES IN CONFERENCE PROCEEDINGS

1. Y. Umeno, W. G. Nöhring, A. Iskandarov, and E. Bitzek (Nov. 2013). “Atomistic Model Analysis of Local and Global Instabilities in Crystals at Finite Temperature”. In: *Key Engineering Materials*. Vol. 592-593, pp. 39–42

REFEREE SERVICES

1. JOM – The Journal of The Minerals, Metals & Materials Society (TMS)

AWARDS

2017	Poster prize of the Gordon Research Conference on Physical Metallurgy
2012	Best student award of the master program Advanced Materials and Processes

TEACHING

2017	Supervision of a Bachelor student project
2015 & 2016	Tutor for “Introduction à la mécanique des structures” (lecturer:Matteo Galli)

